Luiz Delagnelo Barbetta

SOLIDIFICATION FLAW AND POROSITY FORMATION IN HYBRID LASER – GMA WELDING OF THICK API 5L X70 STEEL PLATES

Dissertação submetida ao Programa de Pós-Graduação em Engenharia Mecânica da Universidade Federal de Santa Catarina para a obtenção do Grau de Mestre em Engenharia Mecânica.
Orientador: Prof. Dr.-Ing Walter Lindolfo Weingaertner
Coorientador: Dr.-Ing. Stefan Kaierle

Florianópolis
2014

Ficha de identificação da obra elaborada pelo autor,
através do Programa de Geração Automática da Biblioteca Universitária da UFSC.

Barbetta, Luiz Delagnelo
Solidification flaw and porosity formation in hybrid laser - GMA welding of thick API 5L X70 steel plates / Luiz Delagnelo Barbetta ; orientador, Walter Lindolfo Weingaertner ; coorientador, Stefan Kaierle. - Florianópolis, SC, 2014.
112 p.

Dissertação (mestrado) - Universidade Federal de Santa Catarina, Centro Tecnológico. Programa de Pós-Graduação em Engenharia Mecânica.

Inclui referências

1. Engenharia Mecânica. 2. Hybrid laser - arc welding. 3. Solidification flaw and porosity. 4. Laser. 5. GMAW. I. Weingaertner, Walter Lindolfo. II. Kaierle, Stefan. III. Universidade Federal de Santa Catarina. Programa de Pós-Graduação em Engenharia Mecânica. IV. Título.

Luiz Delagnelo Barbetta

SOLIDIFICATION FLAW AND POROSITY FORMATION IN HYBRID LASER – GMA WELDING OF THICK API 5L X70 STEEL PLATES

Esta Dissertação foi julgada adequada para obtenção do Título de Mestre, e aprovada em sua forma final pelo Programa Pós-Graduação em Engenharia Mecânica (POSMEC).

Florianópolis, 22 de outubro de 2014.

____
Prof. Armando Albertazzi, Dr. Eng.
Coordenador do POSMEC

Banca Examinadora:

____
Prof. Dr.-Ing. Walter Lindolfo Weingaertner
Orientador
Universidade Federal de Santa Catarina

____
Dr.-Ing. Stefan Kaierle
Coorientador
Laser Zentrum Hannover e.V.

____
Prof. Rolf Bertrand Schroeter, Dr. Eng
Universidade Federal de Santa Catarina

____
Prof. Régis Henrique Gonçalves e Silva, Dr. Eng.
Universidade Federal de Santa Catarina

____
Dr. Edson Costa Santos, Ph.D.
Instituto SENAI de Inovação em Laser

Dedico este trabalho à minha família, que sempre me apoiou e me amou não importando a distância.

ACKNOWLEDGEMENTS

This work was developed in the scope of the public-funded HYBRILAS project thanks to the financial and technical support of the *Bundesministerium für Bildung und Forschung* and project partners.

I would like to thank the *Laser Zentrum Hannover* for the opportunity of doing my research in an excellent institute with great infrastructure, work environment and colleagues. Special thanks to Dipl.-Ing. Oliver Seffer and Dr.-Ing. Stefan Kaierle for all the advising and supervising during my work in Germany.

I would like to express my appreciation to all my professors at *Universidade Federal de Santa Catarina* for the prime formation I had during my graduation and my master. I am especially thankful to Prof. Dr.-Ing Walter Lindolfo Weingaertner, my advisor for many years.

None of this would be possible if it was not for my family, who always supported and stimulated me to study and improve myself. Their love also help making life enjoyable and worth living.

Other factor that makes life enjoyable is friendship and I have to thank for having amazing friends both in Brazil and in Germany.

Last but not least, I would like to thank my wonderful girlfriend, Paola, for the great moments we spent together and for the patience while we were apart.

RESUMO

Para melhor compreender a formação de falhas de solidificação e de porosidade na soldagem híbrida laser – GMAW de chapas de aço com grande espessura, foram feitos ensaios com variação de diâmetro do feixe laser, de potência do feixe laser, de metal de adição, de velocidade de soldagem e com oscilação transversal do feixe laser. Esses ensaios foram realizados utilizando-se uma fonte de laser de disco com 16 kW de potência máxima e duas tochas GMAW em chapas de aço alta resistência e baixa liga que atende ao grau de qualidade X70 da API 5L e depois foram avaliados através de imagens metalográficas e de raios-X. Acredita-se que a geometria do cordão de solda tem grande influência na formação de falhas de solidificação e esse trabalho investigou a relação que há entre uma protuberância no cordão de solda e a falha de solidificação, sugerindo ainda uma forma de medir a severidade dessa protuberância: o ângulo de alargamento da protuberância. Foi verificado também como os parâmetros supracitados influenciam o ângulo de alargamento da protuberância e a formação das falhas de solidificação. Duas novas explicações para a discrepância de resultados encontrados na literatura quanto à formação da falha de solidificação foram propostas. Por fim, analisou-se a porosidade encontrada nos cordões de solda através das imagens metalográficas e de raios-X para determinar as suas principais causas na soldagem híbrida laser – GMA de chapas grossas de aço API 5L X70.

Palavras-chave: Soldagem híbrida, laser, MIG/MAG, trinca, descontinuidade.

ABSTRACT

To achieve a better understanding of the solidification flaw and porosity formation in hybrid laser – GMA welding of thick steel plates, tests were carried with varying laser beam width, laser beam power, filler metal, welding speed and with transverse beam oscillation. Those tests were carried using a 16 kW maximal power disk laser source and two GMAW torches on high strength low alloy steel plates that complies with the grade X70 from API 5L that were later analyzed through metallographic and X-ray imaging. It is believed that the weld seam geometry has a high influence on the solidification flaw formation and it was investigated in this work the relation between a bulge in the weld seam and the solidification flaw, introducing a new way to measure the severity of the bulge: the bulge widening angle. It was also verified how the aforementioned parameters influence the bulge widening angle and the solidification flaw formation. Two new explanations for the discrepancy found in the literature regarding the formation of the solidification flaws were proposed. Lastly, the porosity found in the weld seams was analyzed through the metallographic and X-ray images to determine its main causes in the hybrid laser – GMA welding of thick API 5L X70 steel plates.

Keywords: Hybrid welding, laser, MIG/MAG, crack, discontinuity.

RESUMO EXPANDIDO

FORMAÇÃO DE FALHAS DE SOLIDIFICAÇÃO E DE POROSIDADE NA SOLDAGEM HÍBRIDA LASER – GMAW DE CHAPAS GROSSAS DE AÇO API 5L X70

Introdução

A soldagem de chapas grossas é praticamente inevitável na fabricação de gasodutos e oleodutos. Devido à grande espessura dessas chapas, os processos mais usuais para essa união, como GMAW e arco submerso [1-3], não conseguem efetuar a soldagem num único passe e uma grande quantidade de material precisa ser depositada. Para aumentar a velocidade de processo e reduzir a quantidade de metal de adição, é de interesse da indústria que os processos capazes de efetuar essa soldagem num único passe, como soldagem a laser, soldagem por feixe de elétrons e soldagem híbrida laser – arco elétrico, sejam desenvolvidas. O projeto com financiamento público HYBRILAS, desenvolvido pelo Laser Zentrum Hannover e.V. e parceiros, tem como objetivo desenvolver a soldagem híbrida para a soldagem de aços API 5L X70, usados na fabricação de gasodutos e oleodutos, e para a soldagem da liga de alumínio EN AW-6082-T6.

A soldagem híbrida laser – arco elétrico é definida quando se utilizam duas fontes térmicas distintas, o feixe laser e o arco elétrico, em uma mesma poça fundida [4]. Em comparação com a soldagem a laser, a soldagem híbrida apresenta maior velocidade de solda para a mesma potência do laser e maior tolerância ao desalinhamento das faces e à abertura de raiz [5].

Uma das maiores dificuldades na soldagem híbrida laser – arco elétrico é evitar a formação de falhas de solidificação e de porosidade. Falhas de solidificação são curtas descontinuidades que ocorrem com certa regularidade embebidas ao longo da linha central do cordão de solda [6]. Ainda não se sabe exatamente o que causa as falhas de solidificação, mas acredita-se que a geometria da poça fundida, em especial a razão profundidade/largura e a presença de protuberância, seja um dos principais fatores na formação dessas descontinuidades [7].

Objetivos

O principal objetivo deste trabalho é analisar os efeitos dos parâmetros de soldagem na formação de falhas de solidificação e de porosidade na soldagem híbrida laser – GMAW de chapas com 23 mm de espessura de aço API 5L X70 e quais os fenômenos causando essas descontinuidades.

Os objetivos específicos são:

- Verificar a influência do metal de adição, do diâmetro do feixe, da velocidade de soldagem, da potência do laser e da oscilação transversal do feixe laser na formação de falhas de solidificação e de porosidade.
- Estudar a relação entre a geometria da poça fundida, em especial protuberâncias, e o desenvolvimento de falhas de solidificação.
- Melhor compreender os mecanismos que causam as falhas de solidificação.
- Enumerar as principais causas de porosidade nas soldas do projeto HYBRILAS.

Metodologia

As soldagens foram feitas em chapas de aço API 5L X70 com 350 mm de comprimento e 23 mm de espessura, com chanfros de 5 mm no canto superior e de 3 mm no canto inferior das faces a serem soldadas. Esse metal foi escolhido por ser um aço de alta resistência e baixa liga muito utilizado na fabricação de gasodutos e oleodutos.

Foi utilizada uma fonte laser de disco com 16 kW de potência máxima e duas tochas GMAW trabalhando com a transferência de metal no regime de *spray*. A primeira tocha precede o feixe laser e ambos atuam em uma mesma poça fundida. A segunda tocha sucede o feixe laser e atua em uma poça fundida separada da primeira. A figura 1 mostra a geometria do processo. Sob a raiz é colocado um suporte para o cordão de solda preenchido com fluxo para proteger a solda do ar e dar sustentação ao metal fundido.

A tabela 1 mostra todos os parâmetros utilizados neste trabalho. Foram feitas de uma a quatro soldagens com cada uma das sete combinações de parâmetros indicadas na tabela.

Figura 1: Disposição das fontes térmicas.

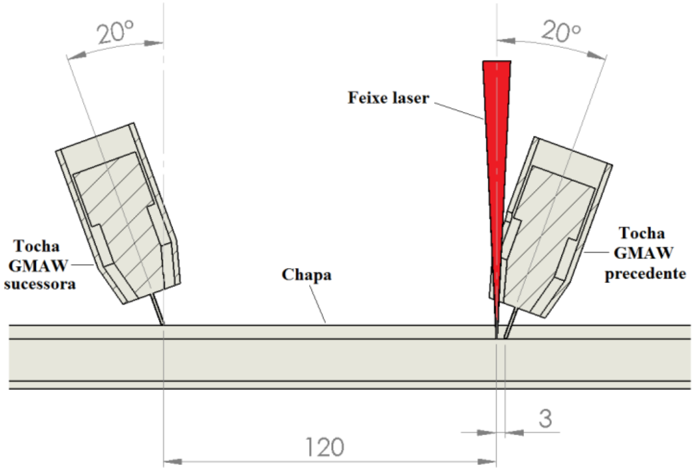

Fonte: Autor

Tabela 1: Combinações de parâmetros para as soldagens.

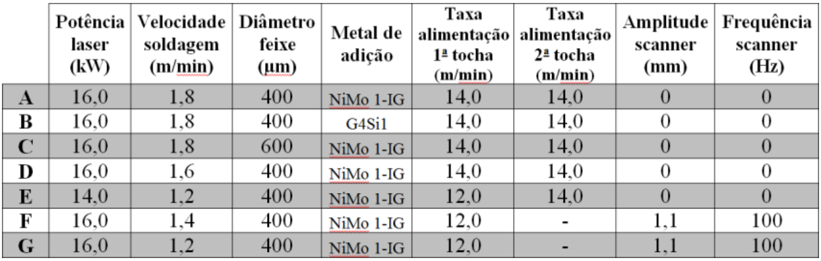

	Potência laser (kW)	Velocidade soldagem (m/min)	Diâmetro feixe (µm)	Metal de adição	Taxa alimentação 1ª tocha (m/min)	Taxa alimentação 2ª tocha (m/min)	Amplitude scanner (mm)	Frequência scanner (Hz)
A	16,0	1,8	400	NiMo 1-IG	14,0	14,0	0	0
B	16,0	1,8	400	G4Si1	14,0	14,0	0	0
C	16,0	1,8	600	NiMo 1-IG	14,0	14,0	0	0
D	16,0	1,6	400	NiMo 1-IG	14,0	14,0	0	0
E	14,0	1,2	400	NiMo 1-IG	12,0	14,0	0	0
F	16,0	1,4	400	NiMo 1-IG	12,0	-	1,1	100
G	16,0	1,2	400	NiMo 1-IG	12,0	-	1,1	100

Foram feitas imagens metalográficas e de raios-X das combinações de parâmetros A, B e C enquanto das combinações de parâmetros D, E, F e G foram feitas apenas imagens metalográficas. As imagens de raios-X podiam mostrar a quantidade e o tamanho das falhas de solidificação e dos poros, enquanto as imagens metalográficas foram feitas de seções transversais do cordão de solda, mostrando, nessa seção, a presença de falhas de solidificação e de porosidade e a geometria da poça fundida.

Para mensurar a severidade de uma protuberância na poça fundida foi definido o ângulo de alargamento da protuberância (β). Ele é medido como o ângulo entre o lado e a altura de um trapézio isósceles cujas bases maior e menor são respectivamente a largura máxima de uma protuberância na poça fundida (B) e a largura mínima da constrição logo acima dessa protuberância (b) e cuja altura é a distância vertical entre as duas, assim como mostra a figura 2.

Figura 2: Definição do ângulo de alargamento da protuberância (β).

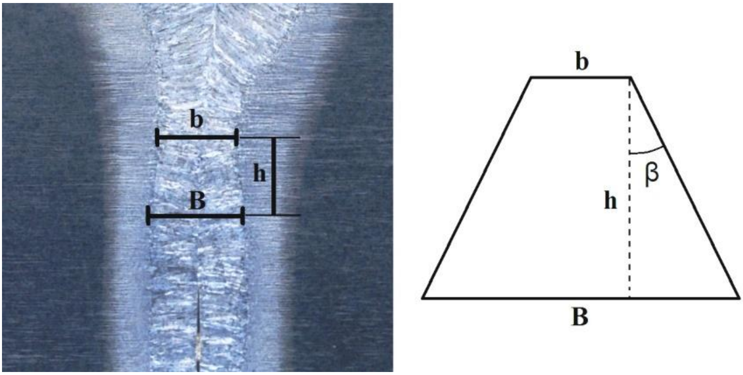

Fonte: Autor

A porosidade foi avaliada quanto à sua posição, ao seu formato e ao seu tamanho. Quanto à sua posição, a seção transversal do cordão de solda foi dividida em quatro regiões às quais um poro poderia pertencer: zona da tocha precedente, zona da tocha sucessora, zona do laser e zona do reforço de raiz. O formato dos poros foi avaliado em regular, sendo mais próximo de esferas e elipsóides, e amorfos.

Resultados e Discussões

Os resultados das imagens de raios-X para a detecção de falhas de solidificação estão demonstrados na tabela 2. C/W indica o comprimento das detecções de falhas de solidificação pelo comprimento do cordão de solda. Foi observado que a segunda metade (2/2) apresenta uma quantidade muito maior de falhas de solidificação do que a primeira (1/2), devido à abertura de raiz, que aumentou de 0 até 0,5 mm ao longo do comprimento da solda devido às cargas térmicas. Para reduzir esse efeito, apenas a primeira metade foi utilizada para as análises a seguir.

Os melhores resultados foram obtidos com a combinação de parâmetros A. B difere de A na composição do metal de adição e apresentou uma quantidade maior de falhas de solidificação, mostrando que o metal de adição tem influência sobre a formação de falhas de solidificação. As soldagens C foram feitas com diâmetro do feixe laser maior e apresentaram uma quantidade muito maior de falhas de solidificação, provavelmente devido a mudanças na geometria e na dinâmica da poça fundida. O que pode ser confirmado observando-se a tabela 3, onde a média do ângulo de abertura da protuberância das soldas C aparece sendo maior que o dobro das soldas A.

Tabela 2: Resultados das imagens de raios-X.

Parâmetros	**A**				**B**	**C**	
Teste	**1**	**2**	**3**	**4**	**1**	**1**	**2**
C/W 1/2	0,047	0,027	0,013	0,000	0,120	0,627	0,400
C/W 2/2	0,433	0,173	0,313	0,207	0,353	0,720	0,613
Maior trinca (mm)	6	8	10	3	6	19	19

Tabela 3: Resultados das medições dos ângulos de alargamento da protuberância (β).

	A	**B**	**C**	**D**	**E**	**F**	**G**
β (°)	1,5	1,4	3,5	2,0	3,7	2,8	1,6

Pôde ser observado também nas imagens metalográficas que a falha de solidificação está sempre associada a uma protuberância, sendo a profundidade média delas **11,5 mm** e **11,0 mm** respectivamente, indicando uma forte relação entre elas. Essa relação foi observada também comparando-se os resultados das detecções de falhas de solidificação pelas imagens de raios-X com os ângulos de alargamento da protuberância, através do gráfico da figura 3. Nele pode ser visto que a quantidade de falhas de solidificação tem uma boa relação com o ângulo β, tanto entre parâmetros diferentes como dentro da mesma combinação de parâmetros.

Dos ensaios analisados apenas por imagens metalográficas, é interessante observar que o cordão de solda realizado com a combinação de parâmetros E apresentou um grande ângulo β e uma falha de solidificação observável. Em comparação com A, a velocidade de soldagem foi menor e o aporte de energia do laser maior, de **533 kJ/m** passou para **700 kJ/m**, e isso causou uma solda mais propensa à formação de falhas de solidificação, como observado por alguns autores [8, 9]. Os ensaios F e G, feitos com oscilação transversal do feixe laser, apresentaram comportamento contrário, sendo a geometria da poça fundida mais suscetível a falhas de solidificação e com falhas de solidificação visíveis em ambas as imagens metalográficas para o ensaio feito com maior velocidade e menor aporte de energia do laser, F, com **686 kJ/m**, do que para o feito com menor velocidade e maior aporte, G, com **800 kJ/m**, estando de acordo com o observado por outros autores [10, 11].

Figura 3: Gráfico do comprimento das falhas de solidificação pelo comprimento do cordão de solda (C/W) em função do ângulo de alargamento da protuberância.

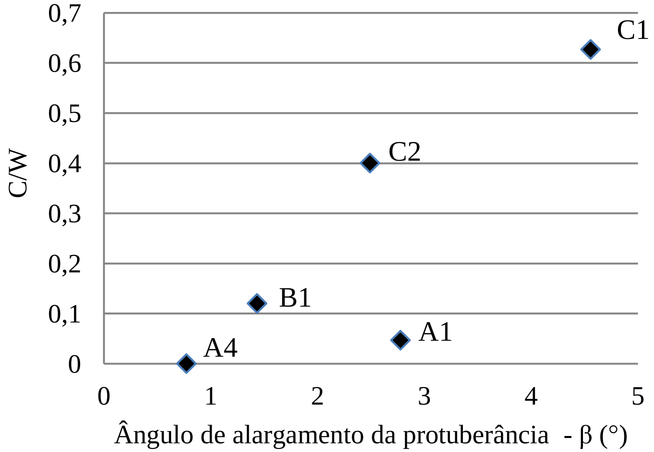

Alguns autores [12] observam características de trincas de solidificação nas falhas de solidificação, enquanto outros [13-15] encontram indícios de formação por rechupe. Se propõe aqui duas possíveis explicações para essa discrepância. A primeira, é a de que são duas descontinuidades diferentes, mas que se confundem, sendo uma a trinca de solidificação e a outra o rechupe, que ocorrem separadamente dependendo das condições da soldagem. Já a segunda explicação sugere que a falha de solidificação nucleie como um rechupe. Se houver tração suficiente, esse rechupe age como um concentrador de tensões e pode levar à formação de uma trinca, deixando uma descontinuidade com características de trinca. Se a tração for pouca, o rechupe crescerá sem formar trincas, apresentando então características apenas de rechupe.

A tabela 4 apresenta como está distribuída a porosidade nas quatro zonas pré-definidas como percentual do total observado nas imagens metalográficas e também o percentual de poros amorfos em cada uma dessas regiões.

Tabela 4: Distribuição da porosidade e proporção de poros amorfos.

Zona	Fração da porosidade total (%)	Poros amorfos (%)
1ª tocha GMAW	45	95
2ª tocha GMAW	13	33
Laser	22	10
Reforço de raiz	20	56

A principal causa da porosidade na zona da tocha GMAW precedente (1ª tocha) acredita-se ser a contaminação pelo ar atmosférico devido às perturbações do fluxo de gás de proteção devido ao *cross-jet*, ao vapor e plasma saindo em alta velocidade do *keyhole* e ao corte no bocal da tocha. A tocha sucessora (2ª tocha), mais distante dessas perturbações apresentou muito menos porosidade, apesar de ocupar uma área maior da seção transversal.

Na zona do laser, acredita-se que a principal causa de porosidade sejam as instabilidades do *keyhole*. As instabilidades do *keyhole* também podem causar parte dos poros encontrados na zona do reforço de raiz. Além disso, proteção insuficiente da raiz por parte do fluxo do suporte para o cordão de solda pode levar à contaminação por ar e causar porosidade.

Os resultados das detecções de poros por imagens de raios-X se encontram na tabela 5. O resultado é mostrado na forma da média de quantidade de poros por comprimento do cordão de solda (P/W) e também indica o maior poro observado. Novamente a abertura de raiz interferiu nos resultados.

Tabela 5: Resultados da detecção de poros pelas imagens de raios-X.

Parâmetros	**A**				**B**	**C**	
Teste	**1**	**2**	**3**	**4**	**1**	**1**	**2**
P/W 1/2 (m^{-1})	30	100	90	40	140	40	10
P/W 2/2 (m^{-1})	7	40	7	13	33	33	17
Maior poro (mm)	0,6	1,0	1,0	1,4	1,0	0,6	0,4

O metal de adição parece ter uma influência na porosidade encontrada na soldagem híbrida laser – GMAW, pois B apresentou mais poros do que A. Os melhores resultados aconteceram para os ensaios feitos com a combinação de parâmetros C, que apresenta um feixe mais largo. O feixe mais largo produz uma abertura maior do *keyhole*, o que deve reduzir a velocidade de saída dos vapores e plasmas do *keyhole*, reduzindo assim uma das fontes de perturbação do fluxo de gás de proteção.

Conclusões

Foi observado que metal de adição, o diâmetro do feixe, a velocidade de soldagem, a potência do laser e a oscilação transversal do feixe influenciam na formação de falhas de solidificação e de porosidade na soldagem híbrida laser – GMAW.

Uma boa relação entre as protuberâncias na poça fundida e as falhas de solidificação foi encontrada, sendo que o ângulo de alargamento da protuberância proposto neste trabalho se mostrou eficaz na mensuração da severidade de uma protuberância.

Resultados divergentes quanto ao efeito da velocidade de soldagem e do aporte térmico do laser foram encontrados, assim como foi observado na literatura.

Duas explicações para a divergência das características das falhas de solidificação encontradas na literatura foram propostas.

As principais causas de porosidade nas diferentes zonas do cordão de solda foram levantadas, sendo que a região mais severamente afetada por porosidade foi a da tocha GMAW precedente.

Referências

[1] BUCKLAND, B. **An Introduction into the Production and Specification of Steel Pipe**. 2005. Disponível em: <http://www.piledrivers.org/>. Data de acesso: 10/05/2014.

[2] TSURU, E.; HARA, T.; ASAHI, H.; MIYAZAKI, H.; YOSHIDA, T. **High-strength steel pipe excellent in formability and burst resistance**. United States Patent 6782921, 2004.

[3] YAPP, D.; BLACKMAN, S. A. **Recent Development in High Productivity Pipeline Welding**, Fronius, 2004.

[4] DVS. **Laserstrahl-Lichtbogen-Hybridschweißverfahren**. Düsseldorf, 2002.

[5] OLSEN, F. O. (Ed.); REUTZEL, E. W.; KATAYAMA, S.; MAHRLE, A.; BEYER, E.; GAO, M.; ZENG, Z. Y.; KUJANPÄÄ, V.; KRISTENSEN, J. K.; LIU, L.; STAUFER, H.; THOMY, C. **Hybrid laser-arc welding**. Cambridge: Woodhead Publishing Limited, 2009. 323 pp.

[6] WEBSTER, S.E., TKACH, Y., LANGENBERG, P., NONN, A., KUCHARCYZK, P., KRISTENSEN, J. K., COURTADE, P., DEBIN, L., PETRING, D. **Hyblas**: economical and safe laser hybrid welding of structural steel. Luxembourg: Off. for Official Publ. of the European Communities, 2009.

[7] KRISTENSEN, J. K.; HANSEN, L. E.; NEILSEN, S. E.; BORGGREEN, K. Laser welding of C-Mn steels and duplex stainless steels. In: EUROPEAN SYMPOSIUM ON ASSESSMENT OF POWER BEAM WELDS, Geesthacht, 1999. **Proceedings...** Geesthacht: GKSS-Forschungszentrum, 1999.

[8] SLV HALLE GMBH. **Erstarrungsbedingte Gefügetrennungen beim Hochenergieschweißen**. Halle. 2009.

[9] KRISTENSEN, J. K.; BORGGREEN, K.; KNUDSEN, S. Large scale testing of laser welded structural steels. In: CONFERENCE ON THE JOINING OF MATERIALS, 8., 1997, Elsinore, 8., 1997. **Proceedings...** Helsingor: Institute for the Joining of Materials, 1997. pp. 1-13.

[10] BUNDESANSTALT FÜR MATERIALFORSCHUNG UND -PRÜFUNG. **Qualifizierung des Nd:YAG- und CO2-Laser-Plasma-Pulver-Hybridschweißens**. Berlin. 2006.

[11] WEISE, S. **Heißrißbildung beim Laserstrahlschweißen von Baustählen**. Bremen: BIAS, 1998. 122 pp.

[12] JÜPTNER, W.; SEPOLD, G.; SCHUBERT, E.; WEISE, S.; KURGUSOW-LINK, A. Modellierung der Heißrißeignung unlegierter Stähle beim Laserstrahlschweißen. **Strahltechnik Band**, Bremen, v. 6, pp. 143-150, 1998.

[13] JACOBSKÖTTER, L. **Laserstrahlschweißen thermomechanisch gewalzter Grobbleche in Dicken zwischen 10 mm und 30 mm**: Vergleich und Kombination mit konventionellen Schweissverfahren. Aachen: Shaker, 1996. 168 pp.

[14]MALY, H. **Laserstrahlschweißen mit Zusatzwerkstoff – Untersuchungen zur Beeinflussung der Nahteigenschaften von Grobblechen**. 1998. 202 pp. Thesis (Dr.) - Rheinisch-Westfälische Technische Hochschule, Aachen.

[15]HENDRICKS, M. **Qualitätsuntersuchungen an Laserstrahlschweißverbindungen un-, niedrig- und hoch-legierter Stähle**. Aachen: Shaker, 1991. 117 pp.

LIST OF FIGURES

Figure 1.1: The UOE pipe making process. 38
Figure 1.2: HYBRILAS welding process. 39
Figure 2.1: Laser, arc and hybrid welding qualities. 41
Figure 2.2: Sketch from a hybrid laser – MIG welding. 42
Figure 2.3: Transversal view of the typical weld seam shape for a) arc welding, b) laser keyhole welding and c) hybrid laser – arc welding. 42
Figure 2.4: GMAW metal transfer modes. 48
Figure 2.5: Typical welding torch for TIG (left) and PAW (right). 49
Figure 2.6: Effects of the D_{LA} on the resulting weld depth. 50
Figure 2.7: Penetration depth as a function of the D_{LA} for a) different processes and b) different arc currents in a hybrid laser – TIG welding with the TIG torch leading. 51
Figure 2.8: Ionization grade of different materials as a function of the temperature. 53
Figure 2.9: Arc narrowing observed on an electric arc of a TIG welding. (a) is without laser and (b) is with a laser. 53
Figure 2.10: An electric arc bended by the influence of a 7 W CO_2 laser. 55
Figure 2.11: Ψ as a function of the D_{LA} for different laser and arc parameters in a hybrid CO_2 laser – GMA welding. 56
Figure 2.12: Effect of the arc current on a hybrid CO_2 laser – TIG welding penetration depth. 57
Figure 2.13: Molten pool shape of a fiber laser welding when the laser induced plume is not suppressed (left) and when it is suppressed with a fan (right). 58
Figure 2.14: Longitudinal section of an 11 kW CO_2 laser weld of 11 mm thick C-Si-Mn steel without back shielding. 59
Figure 2.15: Knob formation at the top of the keyhole and its descent to the bottom, causing a gas bubble. 60
Figure 2.16: Bubble formation process in pulsed laser welding: (a) keyhole drilling, (b) expansion and detachment, (c) pulse termination, post-vaporization and vapor relaxation, (d) cooling, recondensation and shielding gas reverse flow, (e) keyhole collapse formation, (f) contraction, (g) final sphere and buoyancy. 61

Figure 2.17: Schematic welding phenomena during laser welding and during hybrid YAG laser – MIG welding at 120 and 240 A, showing melt flows, bubble and porosity formation or no porosity. 62
Figure 2.18: Effect of grain boundary liquid morphology on crack susceptibility: (a) weld; (b) continuous; (c) isolated. 63
Figure 2.19: Effect of Mn–S ratio and carbon content on solidification cracking susceptibility of carbon steel weld metal. 64
Figure 2.20: Calculated stress distribution in the Sigmajig specimen. . 65
Figure 2.21: Conditions in a Sigmajig specimen. TE in the tensile region (a), TE in the compressive region and (c) Stress distribution along the weld bead centerline. 65
Figure 2.22: Sequence of photographs showing various stages in the Sigmajig test. (a) Molten pool without cracks. (b) Crack nucleation. (c) and (d) Crack propagation. 66
Figure 2.23: Effect of depth/width ratio on centerline cracking. 66
Figure 2.24: Examples of solidification flaws. 67
Figure 2.25: Solidification flaw formation as shrinkage porosity. 68
Figure 3.1: HYBRILAS welding head picture. 70
Figure 3.2: Optical path of the HYBRILAS welding head. 71
Figure 3.3: Specimens geometry and edge preparation. 72
Figure 3.4: Nozzle used for the leading GMAW torch with a cut to allow the laser beam pass. 74
Figure 4.1: Geometrical arrangement of the heat sources. 75
Figure 4.2: Plates positioned and ready to be welded. 76
Figure 4.3: Weld bead support. 77
Figure 4.4: Solidification flaw (h_F) and bulge (h_B) depth definition. 79
Figure 4.5: Method for bulge widening angle determination. 80
Figure 4.6: Definition of the four zones in the cross section view of the weld bead. 82
Figure 5.1: Crack length per weld length (C/W) as a function of laser irradiance. 85
Figure 5.2: Cross sectional metallographic images of welds with solidification flaws. 86

Figure 5.3: The average laser intensity absorbed along keyhole depth (X). 86
Figure 5.4: Cross sectional metallographic image showing the molten pool geometry varying along the same weld seam. 87

Figure 5.5: Total crack length per weld length (C/W) as a function of the bulge widening angle. 88

Figure 5.6: Cross sectional view metallographic images from the beginning of weld D1 (a) and from the end of weld D2 (b). 89

Figure 5.7: Cross sectional view metallographic images of the beginning (a) and of the end (b) of the weld done with parameters E. 91

Figure 5.8: Cross sectional image with defect highlighting of the weld with parameters E. 91

Figure 5.9: Cross sectional view metallographic images of the beginning (a) and of the end (b) of the weld done with arameters F. (c) and (d) show with special lighting the olidification flaws found at the beginning and at the end of the weld respectively. 93

Figure 5.10: Cross sectional view metallographic images of the beginning (a) and of the end (b) of the weld done with parameters G. 93

Figure 5.11: Cross sectional view of the weld defect from the weld with parameters G (a) and representation of the solidification process (b). 94

Figure 5.12: Solidification flaw formed as a solidification cracking. 95

Figure 5.13: SEM image of a solidification flaw surface with shrinkage hole characteristics in a laser beam weld. 96

Figure 5.14: Solidification flaw exhibiting solidification crack characteristics. 96

Figure 5.15: Solidification flaw with no clear sign whether it is a solidification crack or a shrinkage hole. 97

Figure 5.16: Cross section view of the upper region of the weld seam,showing the porosity in the leading GMAW torch zone for tests with parameters A (a) and B (b), but not with C (c). 99

Figure 5.17: Cross section view of the leading GMAW torch zone with severe porosity. 100

Figure 5.18: Graphic of the crack length per weld length (C/W) as a function of the porosity per weld length (P/W). 101

Figure 5.19: Transversal cut view of the cross-jet induced air flow in the working zone. 102

Figure 5.20: Keyhole plume jet inducing shielding gas and air flow. 103

LIST OF TABLES

Table 3.1: Laser source characteristics. 69
Table 3.2: API 5L X70 steel composition. 72
Table 3.3: Filler metals composition in mass percentage. 73
Table 4.1: Backing flux composition used in the weld bead support. 77
Table 4.2: Parameter combination for the welds. 78
Table 5.1: X-ray imaging results for cracks detection showing the accumulated crack length, the C/W and the longest crack for the first half (1/2), second half (2/2) and total length (Total) of the weld seams. 83
Table 5.2: X-ray imaging results for cracks detection showing the accumulated crack length, the C/W and the longest crack for the first half (1/2), second half (2/2) and total length (Total) of the weld seams. 98
Table 5.3: Porosity distribution and shape along the four weld zones. 101

LIST OF ABBREVIATIONS

API – American Petroleum Institute
CC – Constant Current
CV – Constant Voltage
Gasbol – Gasoduto Bolívia-Brasil
GB – Grain Boundary
GMAW – Gas Metal Arc Welding
GTAW – Gas Tungsten Arc Welding
HSLA – High Strength Low Alloy
ISO – International Organization for Standardization
L – Liquid
LZH – Laser Zentrum Hannover e.V.
MAG – Metal Active Gas
MIG – Metal Inert Gas
Nd:YAG – Neodymium-doped Yttrium Aluminium Garnet
PAW – Plasma Arc Welding
PSL – Product Specification Level
S – Solid
SAW – Submerged Arc Welding
TIG – Tungsten Inert Gas
UOE – U-Pressing, O-Pressing and Expansion
Yb:YAG – Ytterbium-doped Yttrium Aluminium Garnet

LIST OF SYMBOLS

β – Bulge widening angle
Θ – Half-angle of the far-field divergence
θ_G – Half-angle of the far field divergence of a Gaussian beam
θ_{NG} – Half-angle of the far field divergence of a non-Gaussian beam
λ – Wavelength
Ψ – Melting energy variation
ω_0 – Beam waist radius
$\omega_{0,G}$ – Beam wais radius of a Gaussian beam
$\omega_{0,NG}$ – Beam wais radius of a non-Gaussian beam
A – Area
b – Trapezium smaller base
B – Trapezium bigger base
BPP – Beam parameter product
BPP_G – Beam parameter product of a Gaussian beam
BPP_{NG} – Beam parameter product of a non-Gaussian beam
C/W – Crack length per weld length
D – Initial beam diameter before being focused
D_{LA} – Laser to arc distance
E_H – Hybrid welding melting energy
E_L – Laser welding melting energy
E_{GMA} – GMA welding melting energy
f – Focal length
h – Trapezium height
h_B – Bulge depth
h_F – Solidification flaw depth
I – Irradiance
M^2 – Beam propagation ratio
P – Laser power
P/W – Pores per weld length
S_{GMA} – GMA welding molten area
S_H – Hybrid welding molten area
S_L – Laser welding molten area
$T_{B,S}$ – Beginning of solidification temperature
T_E – Terminal solidification temperature
X – Keyhole depth

SUMMARY

1 INTRODUCTION 37
1.1 OBJECTIVES 39
1.1.1 General Objective 39
1.1.2 Specific Objectives 39
2 STATE OF ART 41
2.1 INTRODUCTION TO HYBRID WELDING 41
2.2 THERMAL SOURCES 43
2.2.1 Laser Sources 43
2.2.1.1 Wavelength 44
2.2.1.2 Power 44
2.2.1.3 Beam Quality 45
2.2.1.4 Disk Laser 46
2.2.2 Electric Arc Sources 46
2.2.2.1 Consumable Electrode Sources 47
2.2.2.2 Non-Consumable Electrode Sources 48
2.3 RELATIVE POSITION OF THERMAL SOURCES 49
2.3.1 Effects of the Laser to Arc Distance 50
2.4 INTERACTIONS BETWEEN THERMAL SOURCES ... 52
2.4.1 Laser Influences on the Electric Arc 52
2.4.2 Electric Arc Influences on the Laser 55
2.5 WELDING DISCONTINUITIES 58
2.5.1 Porosity 58
2.5.2 Solidification Cracking 62
2.5.3 Solidification Flaws 67
3 EQUIPMENT AND MATERIAL 69
3.1 EQUIPMENT 69

3.1.1 Laser Source ... 69
3.1.2 GMAW Source ... 69
3.1.3 Welding Head ... 69
3.1.4 Robotic Arm ... 71
3.1.5 Weld Monitoring System ... 71
3.2 MATERIAL ... 72
3.2.1 Plates ... 72
3.2.2 Filler Metal ... 73
3.2.3 Shielding Gas ... 73
4 EXPERIMENTAL PROCEDURE ... 75
4.1 PROCESS GEOMETRY ... 75
4.2 TESTS PREPARATION ... 76
4.3 PARAMETERS ... 77
4.4 X-RAY ... 78
4.5 METALLOGRAPHIC IMAGES ... 79
4.5.1 Bulge and Solidification Flaw Depth ... 79
4.5.2 Bulge Widening Angle ... 80
4.5.3 Porosity Evaluation ... 81
5 RESULTS AND DISCUSSION ... 83
5.1 SOLIDIFICATION FLAW ... 83
5.1.1 Focal Spot Size and Filler Metal ... 83
5.1.2 Keyhole Bulging and Solidification Flaws ... 85
5.1.2.1 Bulge and Solidification Flaw Position ... 85
5.1.2.2 Bulge Widening Angle and Solidification Flaw ... 87
5.1.3 Metallographic Images from Parameters D, E, F and G88
5.1.3.1 Parameters D ... 89
5.1.3.2 Parameters E ... 90
5.1.3.3 Parameters F and G ... 92

5.1.4 Solidification Flaw Formation Mechanism 94

5.2 POROSITY 98

5.2.1 Focal Spot Size and Filler Metal 98

5.2.2 Porosity Distribution and Causes 101

5.2.2.1 Leading GMAW Torch Zone 101

5.2.2.2 Trailing GMAW Torch Zone 103

5.2.2.3 Laser Zone 104

5.2.2.4 Root Reinforcement Zone 105

6 CONCLUSIONS 107

6.1 SUGESTIONS FOR FUTURE WORK 108

REFERENCES 110

1 INTRODUCTION

The need of fresh water led to the development of pipelines, a very efficient way of transporting fluids. The first known pipelines were made of hollow bamboos in ancient China to transport water. Those bamboo pipes were even used to transport natural gas to light Beijing around 400 BC. The Roman Empire also relied on pipelines to deliver fresh water to their cities with their well known aqueducts [1].

Nowadays pipelines also play an important role in the transport of oil and gas. They are the most cost effective, reliable and safe mean of oil and gas transportation by land [2]. Material development is one of the main reasons for this success, which enabled high pressure ducts with decreased wall thickness.

Pipes used in the petroleum and natural gas industry are usually classified according to the American Petroleum Institute (API) as a function of their application and mechanical resistance. Steels used for the fabrication of transmission pipelines of oil and gas follow the API 5L standards.

The API 5L X70 steel is a very popular material nowadays for the manufacturing of transmission pipelines for oil and gas. It was used, for example, in the Bolivia-Brazil gas pipeline (Gasbol) [3]. It is a high strength low alloy (HSLA) steel with fine ferrite and pearlite grains.

The commercial manufacturing of large diameter steel pipes includes unavoidably welding processes, both for producing the pipe and to join single pipes into a line. One of the most used technique to produce pipes for oil and gas pipelines is the UOE process, where a metal plate is formed first into a U-shape, than formed into an O-shape, welded and then expanded [4], as shown in figure 1.1.

Due to the wall thickness, two passes of submerged arc welding (SAW) are mostly used for the longitudinal welding of the pipe [4, 5] while for the girth welding, multipass gas metal arc welding (GMAW) is the most popular [6].

To increase the productivity, extended research has been made on one pass welding processes. Laser welding, for instance, had a huge development in recent years and is now accepted for the welding of many API 5L pipes, including grade X70, under PSL1 [7].

Figure 1.1: The UOE pipe making process.

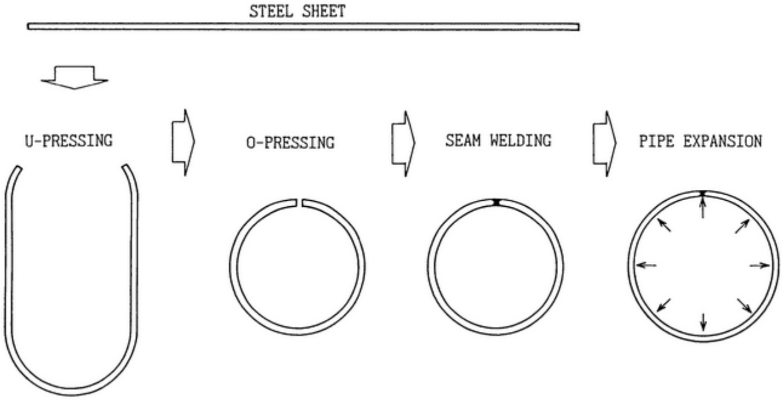

Adapted from: [5]

Laser welding however is very gap sensitive, which demands more careful edge preparation and positioning, increasing the costs. The addition of an electric arc to the laser welding, resulting in a hybrid process, can reduce that gap sensibility. Hybrid laser – arc welding has also some other advantages like higher penetration, faster welding speed and reduced porosity and cracking.

To help developing the hybrid laser – arc welding for the production of pipelines, the *Laser Zentrum Hannover e.V.* (LZH) with other partners and the financial aid from the *Bundesministerium für Bildung und Forschung* created the public-funded HYBRILAS project, in which 23 mm thick API 5L X70 steel plates were welded with a special welding head [8].

The welding head used for that project consists of the optical elements for a 16 kW disk laser and two GMAW torches. The first torch is placed just ahead of the laser beam and acts in the same molten pool, while the second GMAW torch is found behind the laser and forms its own independent molten pool. Figure 1.2 is a sketch of the HYBRILAS welding process.

This work was written under the scope of the HYBRILAS project to try to create a better understanding of some of the main difficulties found when hybrid laser – arc welding thick steel plates: solidification flaws and porosity formation.

Figure 1.2: HYBRILAS welding process.

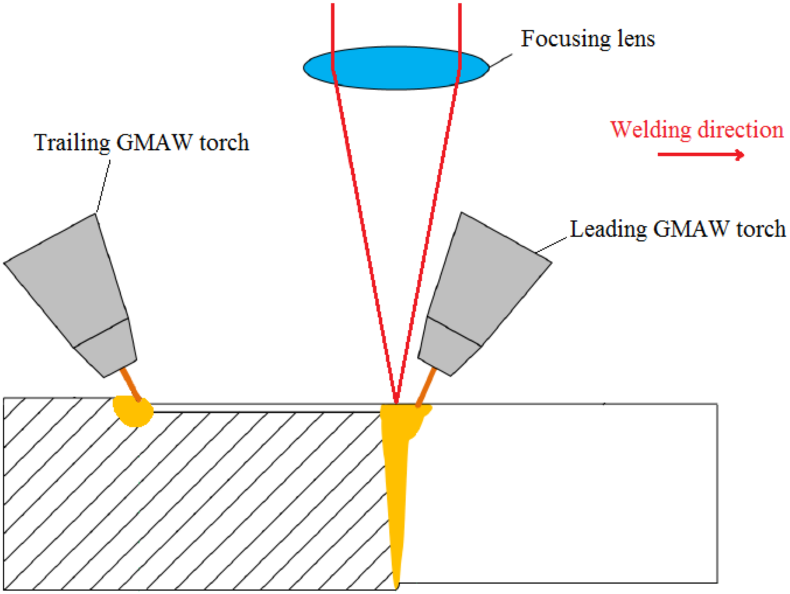
Focusing lens
Trailing GMAW torch
Welding direction
Leading GMAW torch

Adapted from: [8]

1.1 OBJECTIVES

1.1.1 General Objective

The main goal of this work is to analyze the effects of the welding parameters on solidification flaw and porosity formation on hybrid laser – GMA full penetrating welding of 23 mm thick API 5L X70 steel and what are the phenomena causing those discontinuities.

1.1.2 Specific Objectives

- Verify the influence of filler metal, beam width, welding speed, laser power and transverse beam oscillation on solidification flaws and porosity formation.

- Study the relation between molten pool geometry, especially bulges, and solidification flaw development.
- Better understand the mechanisms that lead to solidification flaws.
- Enumerate what are the main causes of porosity in the HYBRILAS hybrid welding.

2 STATE OF ART

2.1 INTRODUCTION TO HYBRID WELDING

Laser welding has become very popular thanks to its high quality, fast welding speed, good precision, high performance, low thermal distortion and ease of automation. But it has some disadvantages, such as low fit-up tolerance, due to its focused energy, predisposition to defects, like porosity, and high initial costs. Arc welding, on the other hand, offers good outcomes with low-cost equipment, possibility of high filler metal deposition rates and good gap bridgeability. It shows however shallow penetration, slow welding speed and high thermal distortions [9-11].

The joining of both processes in one hybrid process, done for the first time in the 70's by Steen *et al* [12], has added the advantages and eased some disadvantages of both processes. The hybrid laser – arc welding has deeper penetration, faster welding speed, higher gap bridgeability and fewer defects [1-15] *apud* Olsen *et al* [9]. Figure 2.1 illustrates the advantages of laser, arc and hybrid welding.

Figure 2.1: Laser, arc and hybrid welding qualities.

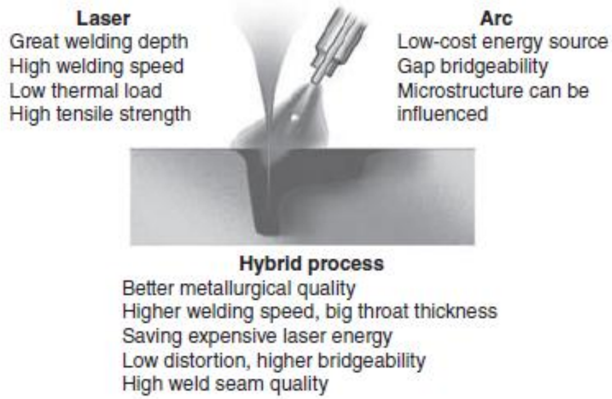
Laser
Great welding depth
High welding speed
Low thermal load
High tensile strength
Arc
Low-cost energy source
Gap bridgeability
Microstructure can be influenced
Hybrid process
Better metallurgical quality
Higher welding speed, big throat thickness
Saving expensive laser energy
Low distortion, higher bridgeability
High weld seam quality

Source: [9]

Hybrid welding is defined when both heat sources act in the same molten pool, with strong interactions between them. If they act in separated molten pools, it is said to be a process combination rather than a hybrid process [13]. When in process combination regime, there are only indirect interactions between the thermal sources, like preheating and annealing [14]. A hybrid laser – MIG welding sketch is presented in figure 2.2

Figure 2.2: Sketch from a hybrid laser – MIG welding.

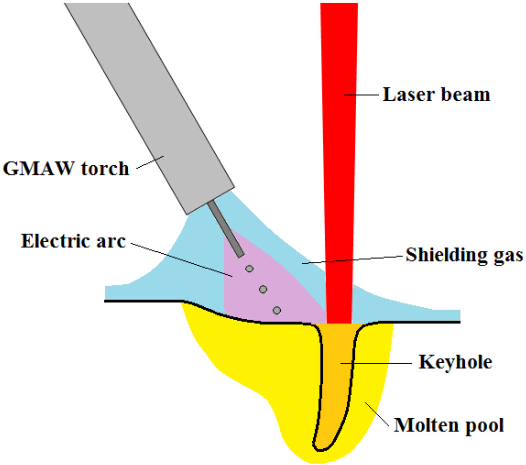
Laser beam
GMAW torch
Electric arc
Shielding gas
Keyhole
Molten pool

Source: The author

The resulting weld seam resembles the combination of the typical cup shape of arc welding and the deep profile of laser keyhole welding in a transversal view, as can be seen in figure 2.3. The characteristics of the upper region are mainly defined by the arc parameters, while the deeper portion is more influenced by the laser, therefore they can be respectively called the arc zone and the laser zone [15, 16].

Figure 2.3: Transversal view of the typical weld seam shape for a) arc welding, b) laser keyhole welding and c) hybrid laser – arc welding.

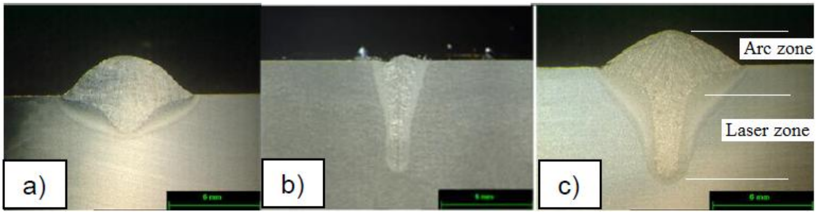
a)
b)
c)
Arc zone
Laser zone

Adapted from: [10]

There are some divergences in the hybrid welding nomenclature. In this work, the term “hybrid laser – arc welding” will be used independently from the order of the thermal sources, although some authors, like Olsen [9], do use “hybrid laser – arc welding” and “hybrid arc – laser welding” as an indicator of the position of the arc, if it trails or leads the laser respectively. “Hybrid laser – arc welding” in this work means only that the laser is the main responsible for the welding penetration depth.

2.2 THERMAL SOURCES

2.2.1 Laser Sources

There are five kinds of laser sources typically used for welding purposes: CO_2, Nd:YAG, diode, fiber and disk lasers. Laser sources with CO_2 or Nd:YAG as active mediums were the first used for welding, but are becoming less popular in favor of the other three newer sources. All of the five mentioned types of laser sources can be used for hybrid laser – arc welding [9, 17].

Different laser sources have different characteristics that make each one unique for welding. The main difference between them being: wavelength, available power and beam quality. Table 2.1 shows the most usual wavelength, the maximal power for industrial use and the beam quality for the most usual laser sources used in metal welding.

Table 2.1: Wavelength, maximal power and beam quality of the most common laser sources for welding.

Laser Source	**Wavelength (µm)**	**Max. Power (kW)**	**Beam quality**
Nd:YAG	1.06	5	Low at high power
CO_2	10.6	45	Low
Diode	0.81~0.94	5	Average
Fiber	1.07	20	Good
Disk	1.03	20	Good

2.2.1.1 Wavelength

The wavelength of the laser light defines how it will interact with matter, setting its reflectivity and absorptivity for different materials. CO_2 laser sources produce light with 10.6 µm wavelength, in the far-infrared zone of the spectrum, while the solid-state lasers have typically around 1 µm wavelength.

One big drawback from CO_2 lasers is that light with that wavelength is readily absorbed by the silica glass from glass fibers, so the beam can only be delivered to the workpiece through hard optics, i.e. mirrors and lenses. On the other hand, the shorter wavelengths of the solid-state lasers make the delivery of the beam through glass fibers as well as through hard optics possible [9, 10].

Another disadvantage of the longer wavelength of CO_2 lasers is that metals tend to have higher reflectivity to it than to the 1 µm light, which reduces the amount of energy effectively absorbed by the processed metal [18, 19]. This problem is reduced when working in keyhole regime, as it will act similar to a black body [19, 20].

Other forms of interaction between light and matter reliant on the wavelength include Rayleigh scattering and inverse Bremsstrahlung absorption [10]. Rayleigh scattering is the scattering of light caused by particles smaller than the light wavelength and is dependent on the wavelength and on the particle size. The inverse Bremsstrahlung effect is the heating of matter by the absorption of photons by electrons, which then collide with atoms and ions, increasing the kinetic energy of them. The inverse Brehmsstrahlung effect is strongly dependent on wavelength, what makes it much more important when working with a CO_2 laser than with solid-state lasers [9, 10, 21]. For this reason Helium is used as shielding gas when welding with a CO_2 laser, as it exhibits a much higher ionization potential than Argon, avoiding the plasma shielding effect, which is the excessive attenuation of the incoming laser light due to the absorption by the plasma [9, 10].

2.2.1.2 Power

Laser power is probably the most important factor defining the welding speed and welding penetration.

Irradiance (I), or power density, is the power per unit area, which is transmitted through an imagined surface perpendicular to the propagation direction and can be measured in W/m^2. It is dependent on the total laser power (P) and how it is distributed, the intensity profile.

For a flat-top distribution, the irradiance is constant along the imagined surface and can be easily calculated as the total power divided by the beam area, as in equation (1). For a Gaussian beam, the irradiance varies along the surface with a maximum in the beam axis, which can be calculated using the equation (2) [22].

$$I = \frac{P}{A} = \frac{P}{\pi\omega^2} \qquad (1)$$

$$I_P = \frac{2P}{\pi\omega^2} \qquad (2)$$

When laser welding, if the irradiance is low, so that only melting is observed, the resulting weld seam is shallow. It is often called the conduction mode welding. Higher irradiances, in the order of 10^6 W/cm^2 or above, promote high evaporation rates. The evaporation is accompanied by an increase in volume, which creates a recoil force that pushes on the molten material and forms a cavity, a keyhole. It is then called keyhole welding. When welding in keyhole mode, the penetration is much higher than in conduction mode [9].

2.2.1.3 Beam Quality

The beam quality indicates its focusability. The most usual mean of measuring beam quality is through beam parameter product (BPP), which is defined as the product between the half-angle of the far-field divergence (θ) and the beam waist radius (ω_0). Knowing the BPP of a laser system, the beam waist radius can be estimated with equation (3), where f is the focal length and D the initial beam diameter before being focused [9].

$$\omega_0 = \frac{2f}{D} BPP \qquad (3)$$

For a certain wavelength, the best quality achievable is that of a Gaussian beam (index G), thus it is often called ideal or diffraction-limited beam. The BPP of a Gaussian beam can be calculated using equation (4) [9].

$$BPP_G = \omega_{0,G}\theta_G \frac{\lambda}{\pi} \qquad (4)$$

When comparing the quality of two beams of the same wavelength, the beam propagation ratio (M^2) can be used. It is defined as the ratio between the BPP of a real or non-Gaussian beam (index NG) and the BPP of a Gaussian beam with the same wavelength. Equation (5) can be used to correlate BPP_{NG} with M^2 [9].

$$BPP_{NG} = \omega_{0,NG}\theta_{NG} = M^2 BPP_G = M^2 \frac{\lambda}{\pi} \qquad (5)$$

Because the quality of the beam affects the beam waist radius, it is also relevant to the maximum achievable irradiance of a laser.

2.2.1.4 Disk Laser

Created by Adolph Giesen in the 1990s, the disk laser is a solid-state laser source capable of achieving high power with high beam quality, making it the main competitor to fiber laser. Its gain medium is usually a thin disk of Yb:YAG measuring between 5 mm and 15 mm in diameter with a thickness of 0.1 mm to 1 mm, generating a light of 1.03 µm wavelength [23, 24].

The most limiting factor against power increase in most typical solid-state lasers, like Nd:YAG, is the heating of the gain medium. With an efficiency of no more than 30 %, a lot of heat is generated inside the resonator and in the crystal of a Nd:YAG laser source and this heat must be dissipated. The rod shape of the crystal utilized in such sources is not optimal for heat dissipation, leading to intolerable thermal lensing effects and risk of damages if the power is increased too much. The disk shape, on the contrary, has a high surface/volume ratio and can be mounted in direct contact with a heat sink element. This way, higher powers with high quality and no damage to the crystal can be achieved [23, 24].

There are already 16 kW power sources available commercially, but more is to come, due to the ease of power scaling from its design [23, 24]. It also seems promising in the short pulses area. 30 mJ pulses with 1.6 ps duration and 10 kHz frequency have already been achieved [25].

2.2.2 Electric Arc Sources

Arc welding was developed at the end of the 19th century and it has now many kinds of welding techniques [9]. They can be divided into two major categories: consumable electrode welding and non-consumable electrode welding.

2.2.2.1 Consumable Electrode Sources

The most important arc welding source nowadays for hybrid welding is the gas metal arc welding (GMAW), thanks to its ease of automation and high metal deposition rates [10]. But investigations with hybrid laser – submerged arc welding have also been done [26].

Depending on the current and voltage of the GMAW process, three primary metal transfer modes can occur: short circuit, globular and spray [9].

The short circuit metal transfer mode happens at relatively low voltage and current. In this regime, there is a transitory contact between the electrode and the melting pool. The electric arc melts some metal from the electrode, but the molten drop does not detach from the wire until the wire reaches the molten pool. When that happens, a short circuit is formed, the electric arc extinguishes itself and the pinch effect and the surface tension causes the molten drop to be transferred to the molten pool. After that material transference, there is again a separation between electrode and workpiece and the arc is reignited. The lower heat input makes this welding mode more adequate for thin plates welding [9].

With slightly higher currents and voltages, the size of the molten metal drops grows, becoming larger than the wire diameter, and are detached by gravity, by electromagnetic forces and, sometimes, by contact with the molten pool. This is called the globular transfer mode. It is often associated with severe spatter and uneven weld seam [9, 17].

With even higher currents and voltages, the electromagnetic force becomes dominant for the detaching of the molten drops from the electrode. This results in smaller and more frequent drops, producing a very stable arc with minimal spatter. As current and voltage are high for this metal transfer mode, the thermal input is also elevated, making it more desirable for the welding of thicker plates. The heat input can be however lowered with the use of pulsed sources, that force the formation of small drops in the pulse current, but keep the mean current lower [9, 17].

Figure 2.4 shows all the three primary metal transfer modes plus a fourth one, the rotating transfer mode, which occurs at even higher currents, but it is very hard to control and rarely used [9].

Figure 2.4: GMAW metal transfer modes.

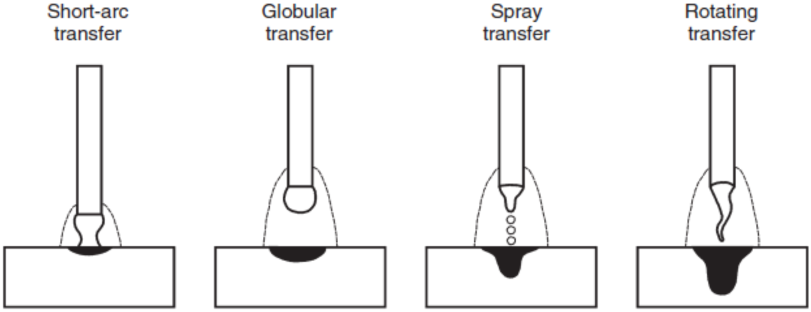

Source: [9]

2.2.2.2 Non-Consumable Electrode Sources

The two most prominent welding techniques that use non-consumable electrodes are the gas tungsten arc welding (GTAW) and the plasma arc welding (PAW). An electric arc is formed between the workpiece and the tungsten electrode in GTAW. Filler metal can be fed to the welding pool separately from the electric circuit, giving this process some more versatility in the choice of parameters, but offering a lower deposition rate when compared to the GMAW process [9]. The first hybrid laser – arc welding system ever made used a GTAW torch as the electric arc source [12] and, nowadays, it is the preferred hybrid laser – arc welding for autogenous welding.

To achieve higher energy densities, the PAW was developed. Its main difference to the GTAW is the constriction nozzle. In PAW, the plasma stream from the electric arc is confined by a second nozzle, so that the arc becomes narrower, as can be seen in figure 2.5 [9]. It is less popular for hybrid welding than GTAW, but it is still a viable option [27].

Figure 2.5: Typical welding torch for TIG (left) and PAW (right).

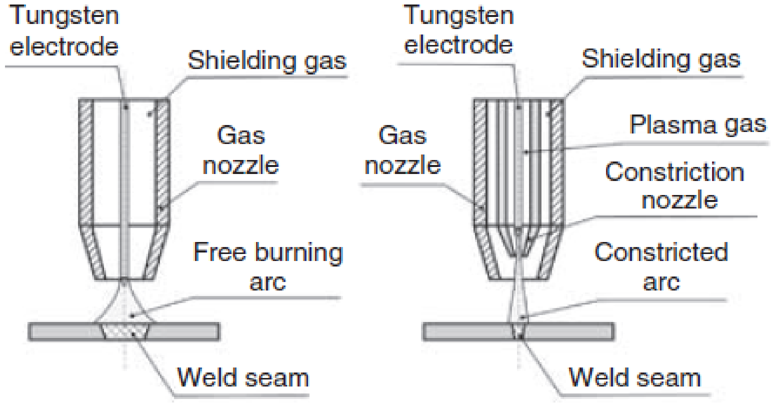
Tungsten electrode
Shielding gas
Gas nozzle
Free burning arc
Weld seam
Tungsten electrode
Shielding gas
Plasma gas
Gas nozzle
Constriction nozzle
Constricted arc
Weld seam

Source: [9]

2.3 RELATIVE POSITION OF THERMAL SOURCES

Aside from the different kinds of laser and arc sources, the way they are geometrically arranged plays also an important role in the welding final result. They can be arranged coaxially or inclined [9].

The coaxial configuration has the main advantage that the results are independent from the welding direction. On the other hand, the laser to arc distance (D_{LA}) is also an important parameter and it cannot be changed in a coaxial design. Other than that, achieving that configuration is not a simple task [9].

Much more popular is the inclined configuration , built usually with the laser beam perpendicular to the workpiece and the arc torch inclined to it, because of its simpler design and the freedom to change the relative position of both heat sources [9].

The separation between both heat sources can be parallel and serial. The parallel separation is the one done in the plane orthogonal to the welding direction, while the serial separation is along the welding path and it can also be considered a temporal separation. A combination of both kinds of separations is possible and common [9].

Hybrid laser – arc welding is also not limited to only two heating sources [8-10, 17, 28, 29].

2.3.1 Effects of the Laser to Arc Distance

Matsuda *et al* [30] have shown that the relative position between the thermal sources have a strong effect on the results obtained from hybrid welding.

As it will be better discussed in chapter 2.4, there are some synergies and interactions between both thermal sources, like arc contraction and laser attenuation, and the level of these effects are dependent on the relative position between laser and arc [28, 31-33].

In hybrid laser – GMA welding if the sources are too close, the laser can disturb the drops detachment, causing an unstable metal transfer and, if the drops impact in the keyhole exit zone, the keyhole can be disturbed [203, 331, 344] *apud* Suder [10].

Another effect that affects the penetration depth of the weld is the welding pool surface shape. The pressure and electromagnetic force generated by the arc cause a depression on the pool and where the interaction point of the laser is located in that depression has a big influence in the total penetration depth [10, 32]. Figure 2.6 shows the effects of the D_{LA} on the resulting welding depth.

Figure 2.6: Effects of the D_{LA} on the resulting weld depth.

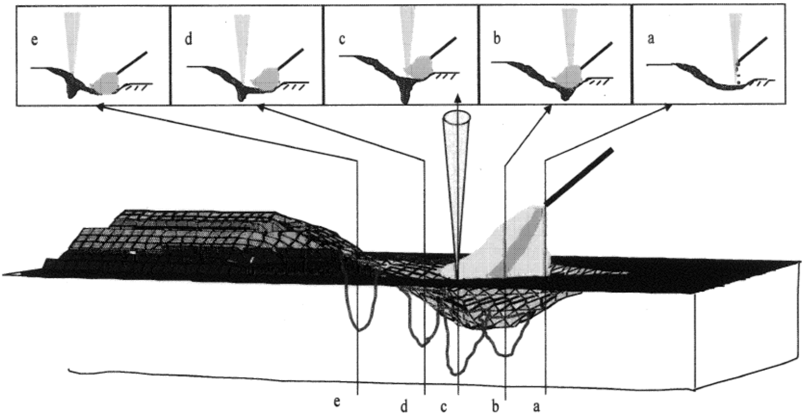

Source: [32]

A lot of experiments have been done to determine the optimal geometrical configuration. In the research from Matsuda and Utsumi [30], using a 5 kW CO_2 laser and GMAW or GTAW torches with currents ranging from 100 A to 400 A, it was concluded that the deepest welding penetration was achieved for the smallest D_{LA}, because it should be the deepest point of the welding pool depression.

Liu *et al* [34] have done some experiments using a hybrid system with a Nd:YAG laser source and a GTAW torch on magnesium alloy AZ31B plates and verified the influence of the D_{LA} on the penetration depth with both GTAW leading and trailing processes. Figure 2.7a) shows some of the results. The deepest welds were achieved with the GTAW torch leading at a 4 mm distance. On the other hand, the GTAW trailing process was even shallower than the laser welding alone at D_{LA} above 3 mm. This lack of penetration was not explained by the authors. In the same work, it was shown that the peak of penetration depth happened at higher D_{LA} when the current was increased, figure 2.7 (b). That might happen because of changes in the welding pool shape.

Figure 2.7: Penetration depth as a function of the D_{LA} for a) different processes and b) different arc currents in a hybrid laser – GTA welding with the GTAW torch leading.

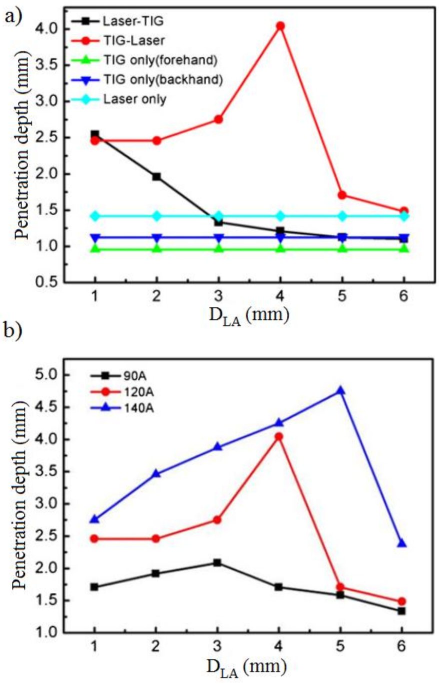

Source: [34]

Welding C/Mn steel with a 12 kW CO_2 laser and a GMAW torch hybrid system, Nielsen *et al* [35] achieved a 10% weld depth increase when welding with the GMAW torch trailing in comparison to it leading. The tests were done with only 1 mm to 2 mm D_{LA} however. That behavior might be different for higher D_{LA}, like what happened in the previous example.

There are different optimal laser and arc arrangements to different welding conditions. There is no absolute best geometrical configuration, because there are many influencing factors that should be considered [9]. Bagger and Olsen [15] claim that ideal distances should be mostly between 1 mm and 3 mm, since those values have been found by many authors [6, 9, 18, 19, 22, 23] *apud* Bagger and Olsen [15].

2.4 INTERACTIONS BETWEEN THERMAL SOURCES

The molten volume has been found to be higher in the hybrid process than the sum of volume in both processes separately in many cases. This shows that there should be synergetic effects when welding with both sources simultaneously [36-40].

2.4.1 Laser Influences on the Electric Arc

Since the first works with hybrid laser – arc welding, Steen *et al* [12] have already noticed increased current, reduced tension, narrowing and rooting of the electric arc when combined with a laser.

The main explanation to those effects is the reduced ionization potential of the local gases due to the presence of metallic vapors produced by the laser keyhole [9, 32, 41-45]. As can be seen in figure 2.8, iron and aluminum reach high ionization grades at much lower temperatures than argon and helium, usual shielding gases. The presence of such metallic vapors reduces the ionization potential near the keyhole opening, reducing the arc electric impedance and increasing its stability [9, 41, 44, 45].

Figure 2.8: Ionization grade of different materials as a function of the temperature.

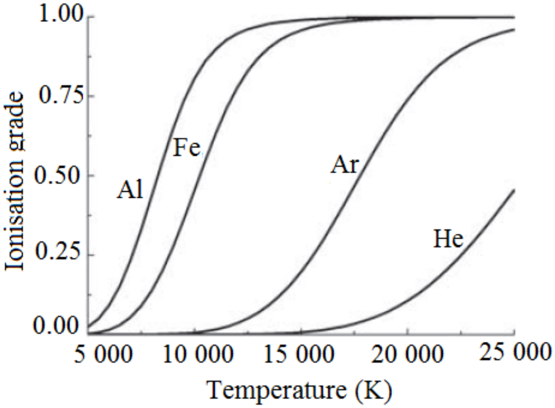

Source: [9]

The decrease in impedance causes the narrowing of the electric arc and the increase of current for constant voltage (CV) sources or the decrease of voltage for constant current (CC) sources. The narrowing of the arc (and the increase in electric current if CV) lead to a beneficial enhance in current density [41, 44-46]. The figure 2.9 shows the effect of a laser acting near a GTAW torch, as observed in the work from Gao *et al* [45].

Figure 2.9: Arc narrowing observed on an electric arc of a GTAW. (a) is without laser and (b) is with a laser.

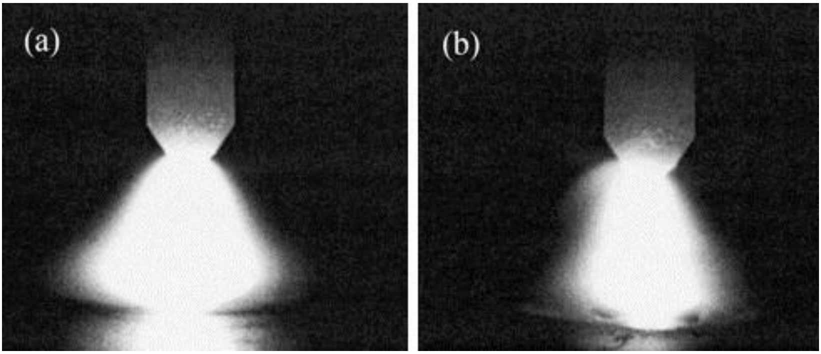

Source: [45]

The closer to the keyhole opening, more metallic vapors there are, so there is an ionization potential gradient. In regular arc welding conditions, the path with the least electrical impedance for the arc between the electrode and the workpiece is usually the shortest one. However, due to the ionization potential gradient, the path with the least impedance might be between the electrode and the keyhole opening, even if it is not the shortest path. This causes the arc to be rooted at the laser interaction point and reduces arc wandering. The arc rooting cannot be fully explained through the reduced ionization potential theory alone though, because it can happen even in situations where the laser induced metallic vapors are not present [12, 47, 48]. Steen and Eboo [12] experienced arc rooting even when the laser actuated in the opposite side of a plate, as long as the surface on the arc side was heated up to at least 400 °C by the laser. Arc rooting was also observed in situations where the laser alone did not have enough power to melt the metal [47, 48].

Some authors believe that the rooting effect may be influenced by the thermionic emission, the emission of electrons from a bulk material, highly dependent on the temperature [9, 47, 49, 50]. But others believe that it should not play an important role, because very high temperatures would be necessary for it to be significant [50, 51]. Stute *et al* [50] estimate that the temperature should be above 2200 °C to induce a considerable thermionic emission in aluminum, even though the arc rooting effect is observed at temperatures much lowers than that.

Aside from the metallic vapors formation, the laser can also increase the plasma ionization grade by two other means: inverse Bremsstrahlung heating and the optogalvanic effect [9, 21, 50-53].

The plasma can be heated by absorbing energy from the laser through inverse Bremsstrahlung, which is much more evident in the 10.6 µm wavelength of CO_2 lasers than in the shorter wavelength from solid-state sources [9, 21, 50-53]. Through mathematical models, Paulini and Simon [53] estimate that 40 % of the energy from a CO_2 laser beam would be absorbed after passing through 10 mm of a plasma with a typical arc welding electron density, while a Nd:YAG laser beam would lose only 0.3 % of its energy to plasma absorption under the same conditions. Arc rooting by a CO_2 laser was observed by Beyer *et al* [54] but it did not happen when welding with a Nd:YAG laser under similar conditions.

The optogalvanic effect can cause a higher ionization grade of the plasma even at low irradiance levels. This effect happens when the photon energy matches the energy gap between two atomic energy levels, inducing the electron to jump to the higher level. The atom becomes then more easily ionized through inelastic electron-atom collisions, as the electron now needs less energy to be extracted from the atom [50]. Stute *et al* [50] showed through their experiments that an electric arc can be rooted through the optogalvanic effect.

It was clearly shown by Hermsdorf [40] that an electric arc can interact with a very low power laser. The figure 2.10 shows an electric arc being guided by a 7 W CO_2 laser beam, even though that was not the shortest path between both electrodes.

Figure 2.10: An electric arc bended under the influence of a 7 W CO_2 laser.

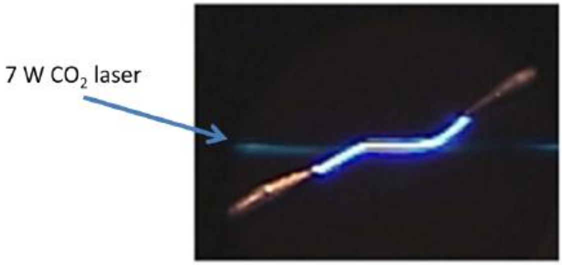

Source: [40]

2.4.2 Electric Arc Influences on the Laser

The absorptivity of metals to the typical wavelengths from laser sources increase sensibly with the temperature [55], so many authors believe that the preheating of the workpiece by the arc welding can increase the laser absorption [37, 48, 56-58]. Diebold and Albright [48] noticed an increase in CO_2 laser coupling with aluminum after the ignition of a TIG torch in a hybrid process.

Gao *et al* [16] did some experiments with hybrid CO_2 laser – GMA welding of mild steel and analyzed the results using the dimensionless parameter Ψ, the variation of the melting energy between the hybrid process and the sum of the two processes separately, defined by equation (6). With a D_{LA} of up to 4 mm, they observed that the dominant synergetic effect was the increased current and narrowing of the arc with a Ψ up to 23%, which means 23% more melting energy as compared to the two processes apart. Above 4 mm separation the arc suffers little to no influence from the laser and the preheating effect becomes dominant. From the graphic in figure 2.11, it can be concluded that the absorption increase of the laser is low for steels, with Ψ below 5%.

$$\Psi = \frac{E_H - (E_L + E_{GMA})}{E_L + E_{GMA}} = \frac{S_H - (S_L + S_{GMA})}{S_L + S_{GMA}} \qquad (6)$$

Figure 2.11: Ψ as a function of the D_{LA} for different laser and arc parameters in a hybrid CO_2 laser – GMA welding.

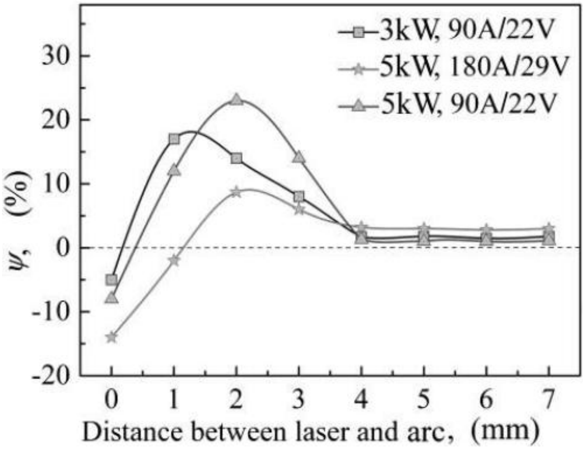

Source: [16]

A second beneficial effect of the preheating is the reduction of thermal diffusivity, reducing the energy loss through conduction to the rest of the workpiece [37].

As previously discussed, there is laser absorption by the plasma through inverse Bremsstrahlung effect. Although it might be advantageous for the electric arc, because of the increase in its ionization grade, the beam energy reaching the workpiece is reduced, especially from CO2 lasers [9, 42, 59]. This effect is quite obvious in the experiments from Chen *et al* [42], who did some tests varying the current of a TIG torch in a hybrid CO_2 laser – GTA welding system, shown in figure 2.12. The penetration increased with increasing current up to a peak. Further increases in GTAW torch current have only reduced the penetration depth, because of the excessive inverse Bremsstrahlung absorption.

Figure 2.12: Effect of the arc current on a hybrid CO_2 laser – TIG welding penetration depth.

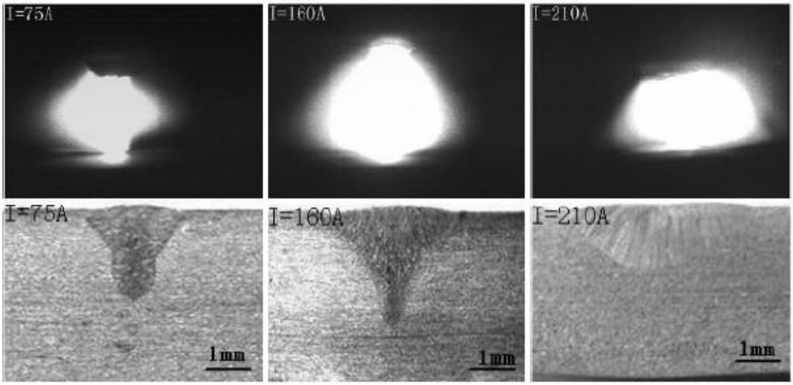

Source: [42]

In the case of 1 µm wavelength lasers, there is very little absorption of the laser by the plasma, but the plasma and gases found in the laser path can still have other undesirable effects on it [51, 60-62]. The laser irradiance on the workpiece might be reduced due to refraction, because the high thermal gradients found in the gases and plasmas in the working area induce a refraction gradient as well [51, 60]. Katayama *et al* [60] showed in their experiments that a high plume during fiber laser welding have negative effects on the weld. The uneven refraction indexes in the laser path cause defocusing and random deflection of the beam. As can be seen in figure 2.13, in the tests where a fan was used to suppress the plume formation, there is a small keyhole with one regular shaped welding pool. Without the fan, fusion points ahead and at the sides of the welding pool are found, due to the erratic deflection of the beam trajectory caused by the plume.

Figure 2.13: Molten pool shape of a fiber laser welding when the laser induced plume is not suppressed (left) and when it is suppressed with a fan (right).

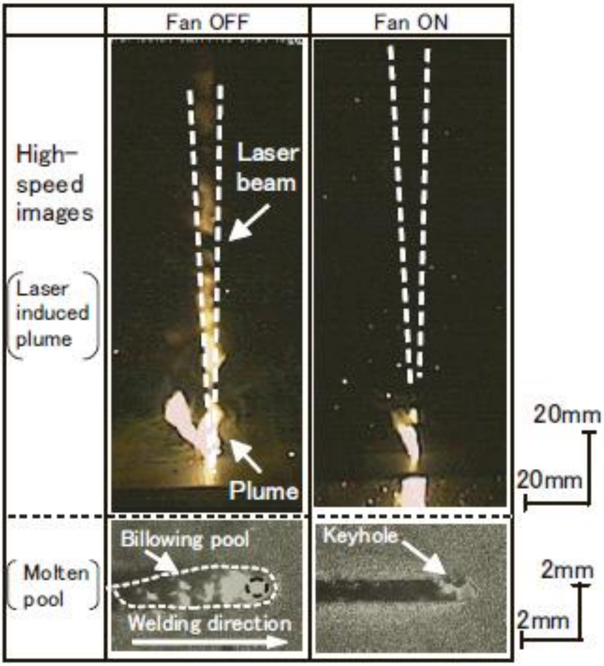
Fan OFF
Fan ON
High-speed images
(Laser induced plume)
Laser beam
Plume
20mm
20mm
(Molten pool)
Billowing pool
Welding direction
Keyhole
2mm
2mm

Source: [60]

2.5 WELDING DISCONTINUITIES

2.5.1 Porosity

Porosity is a discontinuity of the weld caused by gas entrapment during solidification [63]. It is not considered a very serious defect, as long as its size and quantity do not reach high levels [64].

Pores are usually formed by dissolved gases, like hydrogen, nitrogen and oxygen, and by chemical reactions in the molten pool [63, 65]. Hydrogen is the main cause of porosity in aluminum, copper, titanium and magnesium. In steels however, hydrogen is more likely to cause cracks than pores [63].

The nitrogen found in the air can cause pores in carbon steels, stainless steels and nickel alloys [63]. Nitrogen induced porosity can also be extremely severe in full penetration CO_2 laser welding without back shielding. The energy of the laser induces plasma rich in monatomic nitrogen on the backside of the weld, which can be easily dissolved into the molten metal [66, 67]. A result of such a welding is shown in figure 2.14.

Figure 2.14: Longitudinal section of an 11 kW CO_2 laser weld of 11 mm thick C-Si-Mn steel without back shielding.

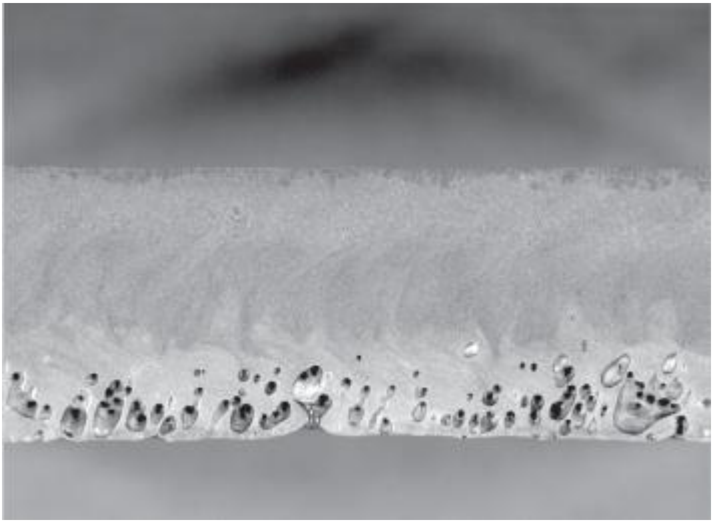

Source: [66]

The main causes of porosity are [64]:

- Surface contaminants, like oil, grease, rustiness and humidity;
- Zinc coating and painting;
- Not enough protection by the shielding gas, due to low shielding gas flow, incorrect constitution or turbulence. Turbulence might be due to exaggerated flux or wind.

During deep laser welding, porosity may arise due to keyhole instabilities [65, 68, 69]. The instabilities cause the collapsing of the keyhole bottom, entrapping metallic vapors, shielding gas and air. The metallic vapors condensate with the reducing temperatures and form oxides with any eventual oxygen present, leaving a pore with shielding gas and small quantities of nitrogen and hydrogen, that might have been entrapped by the keyhole collapsing or diffused all the way to the pore

[65, 68, 70, 71]. Matsunawa *et al* [70, 72] explain that the evaporation at the keyhole front wall happens locally and not evenly through its entire depth, generating a knob, or a step, that moves from the upper side to the bottom of the keyhole. This localized evaporation produces a depression in the rear wall of the keyhole, because of the recoil pressure. When the knob reaches the bottom of the keyhole, the depression on the rear wall can develop into a bubble, or it can cause the bottom of the keyhole to collapse. Figure 2.15 depicts this effect.

During pulsed laser welding, the keyhole collapses when the laser stops providing energy. As explained in the figure 2.16, the collapsing keyhole can entrap gas that causes porosity [65, 68].

The porosity formation due to keyhole instabilities is strongly reduced in full penetration welding. This happens because the gas that would be imprisoned by the downward dislocating knob is expelled from the keyhole when it reaches the bottom of the weld [60, 65, 73]. Porosity can still occur due to localized evaporation, caused by the knob or by lower temperature evaporating elements. If enough recoil pressure is provided, the depression seem in figure 2.15 can develop into a bubble before the knob reaches the bottom of the keyhole [65].

Figure 2.15: Knob formation at the top of the keyhole and its descent to the bottom, causing a gas bubble.

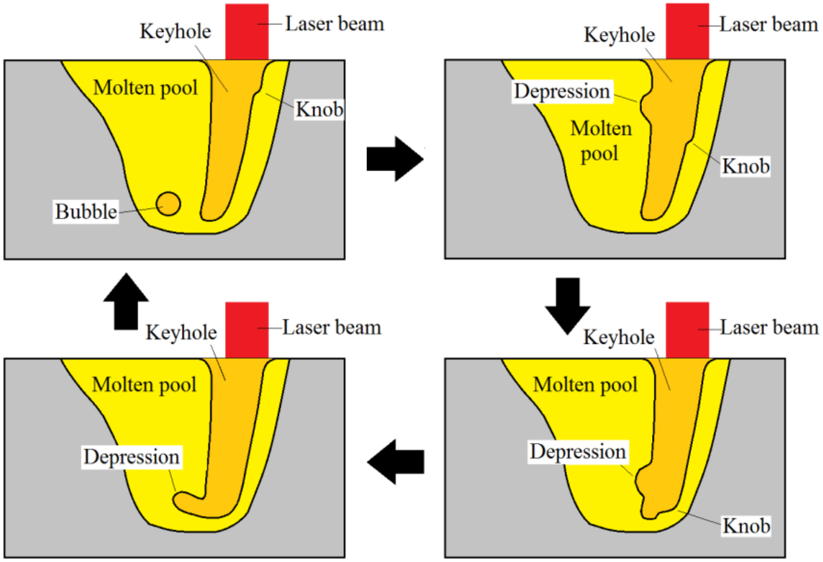
Keyhole
Laser beam
Molten pool
Knob
Bubble
Keyhole
Laser beam
Depression
Molten pool
Knob
Keyhole
Laser beam
Molten pool
Depression
Keyhole
Laser beam
Molten pool
Depression
Knob

Adapted from: [72]

Figure 2.16: Bubble formation process in pulsed laser welding: (a) keyhole drilling, (b) expansion and detachment, (c) pulse termination, post-vaporization and vapor relaxation, (d) cooling, recondensation and shielding gas reverse flow, (e) keyhole collapse, (f) contraction, (g) final sphere and buoyancy.

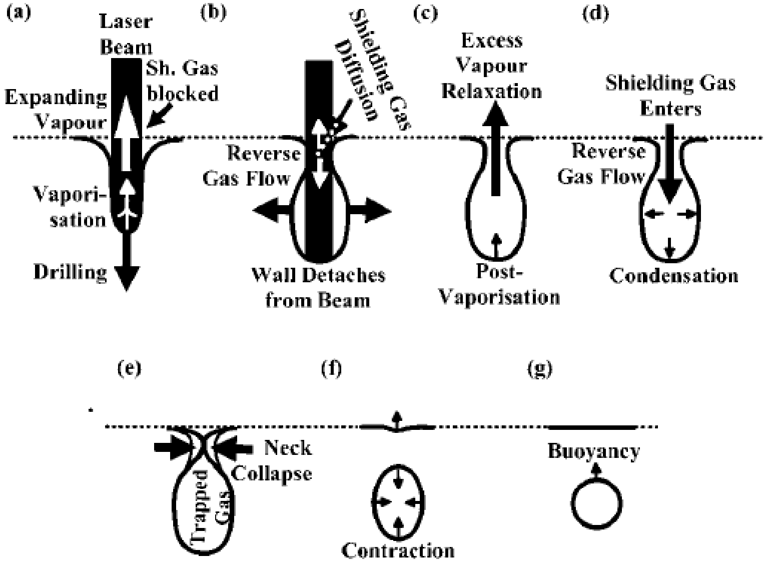
(a)
Laser Beam
Sh. Gas blocked
Expanding Vapour
Vapori-sation
Drilling
(b)
Shielding Gas Diffusion
Reverse Gas Flow
Wall Detaches from Beam
(c)
Excess Vapour Relaxation
Post-Vaporisation
(d)
Shielding Gas Enters
Reverse Gas Flow
Condensation
(e)
Neck Collapse
Trapped Gas
(f)
Contraction
(g)
Buoyancy

Source: [68]

Hybrid laser – arc welding is less susceptible to porosity formation than laser welding. This might be due to [9, 10, 60]:

- Higher heat input that provides more time for the bubbles to be eliminated at the surface;
- Electromagnetic forces influencing the molten material flow; and
- Increased keyhole inlet diameter and stability.

Katayama *et al* [74] did some experiments welding stainless steel with hybrid laser – TIG welding and aluminum with hybrid laser – MIG welding and verified that increasing arc current reduced the weld porosity. The interesting fact is that the porosity reduction mechanisms were different for both processes. In the hybrid laser – TIG welding of stainless steel, the keyhole became more stable due to its increased inlet opening and fewer bubbles were formed due to keyhole instabilities. In the hybrid laser – MIG welding of aluminum, the MIG arc produced a concavity on the molten pool. This concavity made it easier for the gas bubbles in the molten material to reach the surface and dissipate. Figure 2.17 shows this effect.

Figure 2.17: Schematic welding phenomena during laser welding and during hybrid YAG laser – MIG welding at 120 and 240 A, showing melt flows, bubble and porosity formation or no porosity.

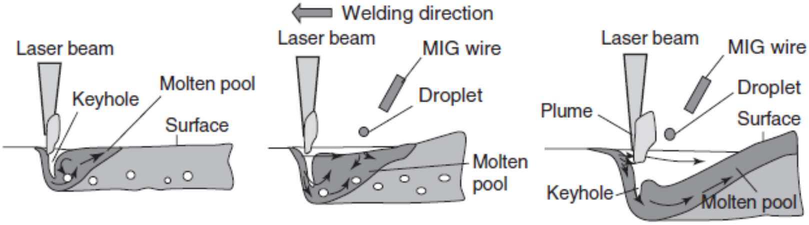
Welding direction
Laser beam
Keyhole
Molten pool
Surface
Laser beam
MIG wire
Droplet
Molten pool
Laser beam
MIG wire
Plume
Droplet
Surface
Keyhole
Molten pool

Source: [74]

2.5.2 Solidification Cracking

Solidification and cooling shrinkage generate stresses in the weld that might lead to cracking. Hot cracks for instance are caused by the tensile stresses during the final stages of solidification, when thin films of liquid remain between two solidification fronts [75-77].

ISO 5817 [78] considers cracks, except for micro-cracks, as serious and intolerable defects to any weld quality, B, C or D, because they act as strong stress concentrators. API 5L [7] does not allow any kind of cracks in pipes.

The main causes of hot cracking are [64, 79]:

- Weld metal composition;
- Movement restriction;
- Depth/width ratio;
- Gap.

Metallurgical factors, defined mainly by the weld metal composition, that affect the hot cracking susceptibility include [79]:

- Solidification temperature range;
- Quantity and distribution of liquid in the final stages of solidification;
- Primary solidification phase;
- Surface tension; and

- Grain structure.

The solidification temperature range depends on the alloy elements and impurities of the metal. Sulfur is an impurity example that makes steels more susceptible to hot cracking. The compound FeS has a lower solidification point, 938 °C, and low surface tension with solid steel, resulting in crack inducing thin films during solidification. Manganese helps reducing the hot crack formation, because sulfur forms preferentially MnS instead of FeS, which has higher solidification point and higher surface tension with solid steel than FeS [79, 80]. Figure 2.18 shows the effect of the surface tension on liquid distribution during solidification. Higher surface tension liquids tend to form isolated globules instead of continuous films of grain boundary liquid, resulting in increased weld resistance during solidification [79,80]. The effect of sulfur, manganese and carbon content in hot cracking of steel is presented at figure 2.19.

Figure 2.18: Effect of grain boundary liquid morphology on crack susceptibility: (a) weld; (b) continuous; (c) isolated.

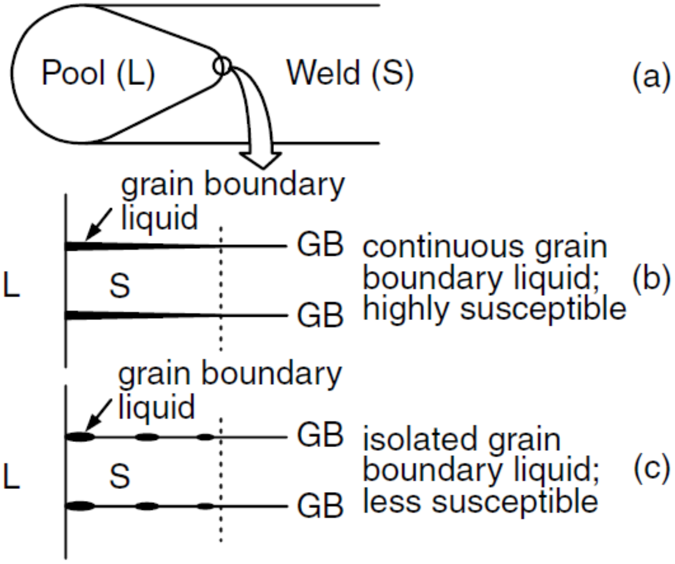
Pool (L)
Weld (S)
(a)
grain boundary liquid
L
S
GB
GB
continuous grain boundary liquid; highly susceptible
(b)
grain boundary liquid
L
S
GB
GB
isolated grain boundary liquid; less susceptible
(c)

Source: [79]

Figure 2.19: Effect of Mn–S ratio and carbon content on solidification cracking susceptibility of carbon steel weld metal.

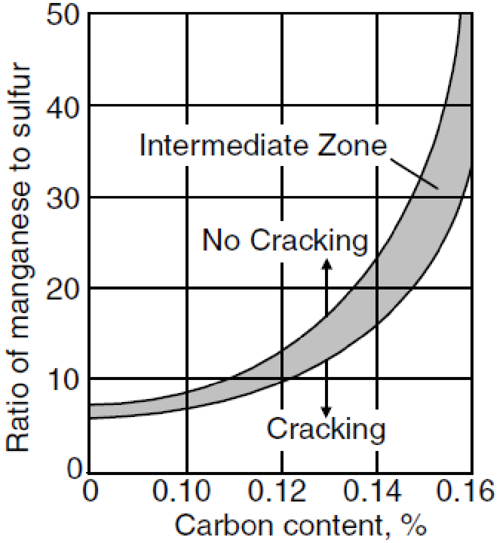

Source: [81]

It is well accepted that the process is more sensible to hot cracking if there is movement restraint of the welded pieces [79].

Solidification cracks do not form at the tip of the molten pool, but lags some distance behind the pool [82, 83]. That happens because compressive stress is present around the welding pool, as observed by Chihoski [82] through Moire fringe and by Zacharia [83] through his numerical model. Zacharia's model also shows tensile stresses in a region behind the molten pool, where temperature can still be high enough for low solidification point materials, like FeS, to remain liquid and induce solidification cracking [83]. Figure 2.20 presents the transversal stress fields obtained through numerical simulation of a Sigmajig test and figure 2.21 describe the conditions required for solidification cracking. If the terminal solidification temperature (TE) is found in the tensile region, solidification crack may occur (Figure 2.21 (a)), but if the liquid is only present in the compressive region, no solidification crack will happen (Figure 2.21 (b)). In the same work, direct observation of solidification crack development showed the nucleation happening at a certain distance from the molten pool and later propagation in the direction of the molten pool, figure 2.22. It was also observed that the distance at which the stress changed from compressive to tensile decreased with the increase of the tensile pre-load of the Sigmajig test. That means that tensile stress is present in regions with higher temperatures for higher pre-loads, where the presence of liquids is more likely. Leading to the conclusion that higher movement restraints leave the weld more sensitive to solidification cracking [83].

Figure 2.20: Calculated stress distribution in the Sigmajig specimen.

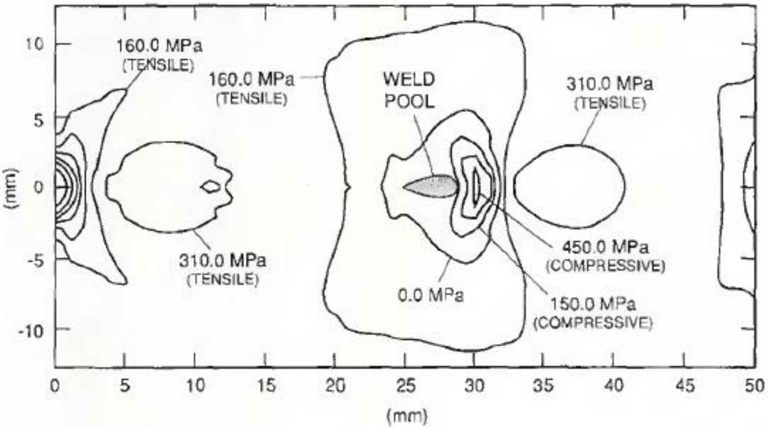

Source: [83]

Figure 2.21: Conditions in a Sigmajig specimen. T_E in the tensile region (a), TE in the compressive region and (c) Stress distribution along the weld bead centerline.

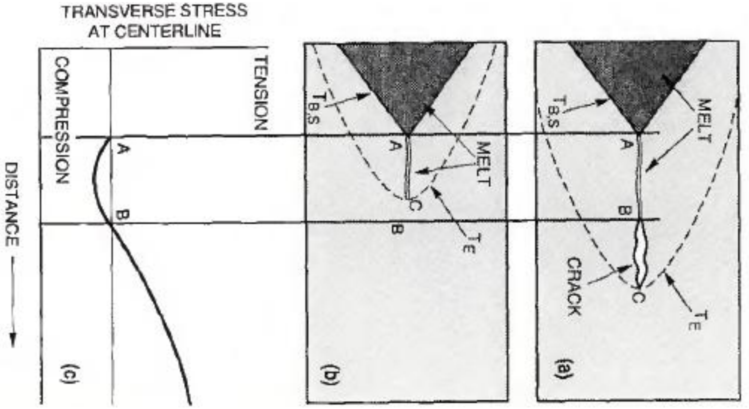
TRANSVERSE STRESS AT CENTERLINE
COMPRESSION
TENSION
DISTANCE
A
B
(c)
$T_{B,S}$
MELT
A
C
B
T_E
(b)
$T_{B,S}$
MELT
A
B
CRACK
C
T_E
(a)

Source: [83]

Figure 2.22: Sequence of photographs showing various stages in the Sigmajig test. (a) Molten pool without cracks. (b) Crack nucleation. (c) and (d) Crack propagation.

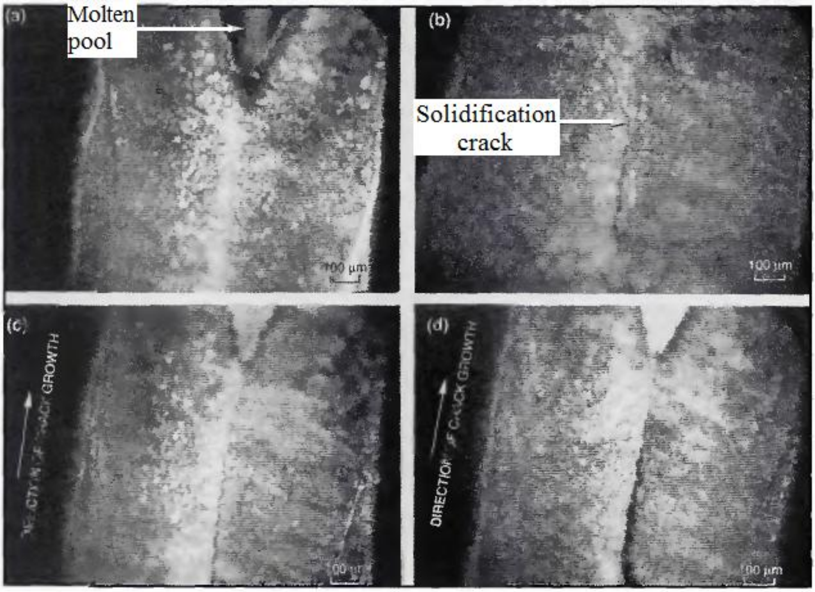
(a)
Molten pool
100 µm
(b)
Solidification crack
100 µm
(c)
DIRECTION OF CRACK GROWTH
100 µm
(d)
DIRECTION OF CRACK GROWTH
100 µm

Source: [83]

High depth/width ratio of the weld seam can also lead to hot cracking, because of the steep angle of abutment between columnar grains growing from opposite sides [79, 80, 84]. The effect of the depth/width ratio is shown in figure 2.23. The laser keyhole welding can have very high ratios in combination with high cooling rates, causing it to be more susceptible to hot cracks [9, 79, 80]. The addition of an arc thermal source reduces the width/depth ratio and the cooling rate of the hybrid process, making it less prone to hot cracking [9, 15, 85].

Figure 2.23: Effect of depth/width ratio on centerline cracking.

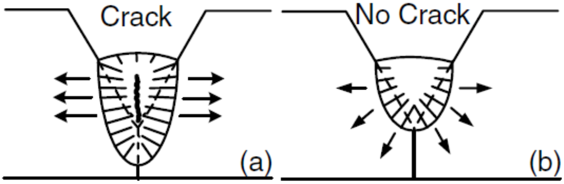
Crack
No Crack
(a)
(b)

Source: [84]

2.5.3 Solidification Flaw

Solidification flaw is a defect that was only observed after thick plates started to be laser welded. It is usually a small isolated defect happening with certain regularity along the weld seam center line. Some examples are shown in figure 2.24. There is a big discussion about its formation mechanisms. One explanation given in the literature is that it is actually a solidification crack, just like the cracks discussed in chapter 2.5.2, but happening deeper in the weld seam. The other main explanation is that it is shrinkage porosity, similar to that found in casting [86, 87].

Figure 2.24: Examples of solidification flaws.

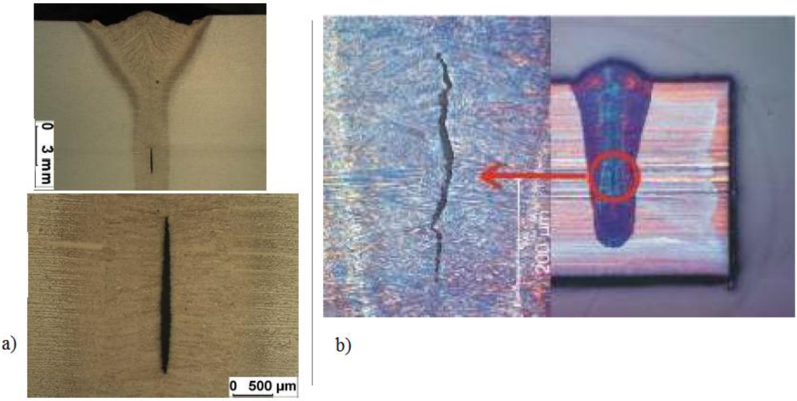

Sources: a) [88]; b) [89]

As a shrinkage defect, it could be caused by a bulge in the weld seam profile. Figure 2.25 helps to explain the phenomenon. Firstly a molten pool is formed with a bulge in its middle (a), due to energy distribution in the keyhole. The solidification fronts grow from both sides (b) until they meet above and under the bulge, while the bulge still has molten metal (c). The material inside the bulge will keep solidifying, shrinking in the process. Since the transport of molten metal to the bulge is very limited, it cannot compensate the volume loss induced by solidification and thermal shrinkage happening in the bulge, so there might be a void by the end of the solidification (d). That void is the solidification flaw [86].

Figure 2.25: Solidification flaw formation as shrinkage porosity.

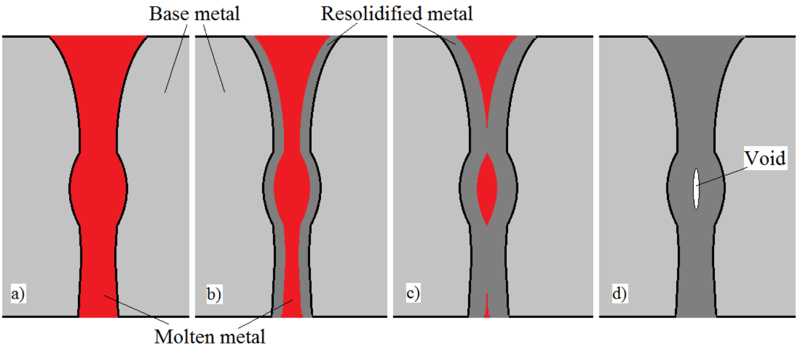

Source: The author

Although it is a complex and not well understood phenomenon, there are factors known to have some influence on the solidification flaw development [90]:

- Keyhole geometry, especially depth/width ratio and bulging;
- Keyhole dynamics;
- Solidification shrinkage;
- Solidification temperature range;
- Welding speed;
- Quantity and kind of segregation;
- Solidification mode;
- Weld geometry; and
- Grain size of the solidification structure.

To reduce the possibility of solidification flaw formation, it is often suggested to reduce the welding speed. That should make the keyhole more stable, reduce the bulging and reduce the temperature gradient [89, 91]. But it has also been observed that increasing the welding speed can reduce solidification flaw in some cases as well, because it leads to a more parallel profile [92, 93]. Increasing the Rayleigh length, or the focus position, can also promote better results by changing the energy distribution in the keyhole [91, 92]. Change of the weld material to avoid solidification temperature range increasing elements, like sulfur and phosphorus, can also help [86].

3 EQUIPMENT AND MATERIAL

3.1 EQUIPMENT

3.1.1 Laser Source

The laser source used for this work was a disk laser TRUMPF TruDisk 16002. It achieves up to 16 kW coupling four 4 kW Yb:YAG disks in its resonator. Table 3.1 presents some of its characteristics.

Table 3.1: Laser source characteristics.

Power	320 W to 16 kW
Lowest BPP	8 mm·mrad
Wavelength	1030 nm
Minimum fiber diameter	200 µm
Energy efficiency	>30%

The beam is delivered to the welding head through an optical fiber. Two different fibers were used for the experiments, one with a diameter of 200 µm and the other with 300 µm.

3.1.2 GMAW Source

Both the GMAW used in the project are from the Phoenix 522 RC Puls force model from EWM Hightec Welding GmbH. It is a programmable pulsed power source with welding current ranging from 5 A to 520 A with an open circuit voltage of 79 V. This arc source allows the use of preprogrammed current–voltage curves to adequate itself easily to the process. Both GMAW torches work under the spray transfer mode.

Phoenix Drive4 Rob 3 is the model of the wire feeders, which is also from EWM Hightec Welding GmbH. They enable feeding speeds from 0.5 m/min up to 24 m/min.

3.1.3 Welding Head

The HYBRILAS welding head, figure 3.1, consists of an YW52 laser welding head from Precitec GmbH & Co. KG, a coaxial camera, a scanner, two GMAW torches and an additional cross-jet. So there are two cross-jets, the one that is part of the YW52 laser welding head and an additional cross-jet for extra protection of the optical elements. The whole welding head weights 20 kg.

The coaxial camera is a MV-D1024E-3D01-160-CL-12 from Photonfocus AG. It has a maximal resolution of 1024 x 1024 pixels, a frame rate of 150 fps at maximal resolution and 12 bit grayscale color resolution. The scanner from ARGES GmbH can reach oscillations of up to 500 Hz. The maximal amplitude in the focal spot at 50 Hz is 3 mm.

Figure 3.1: HYBRILAS welding head picture.

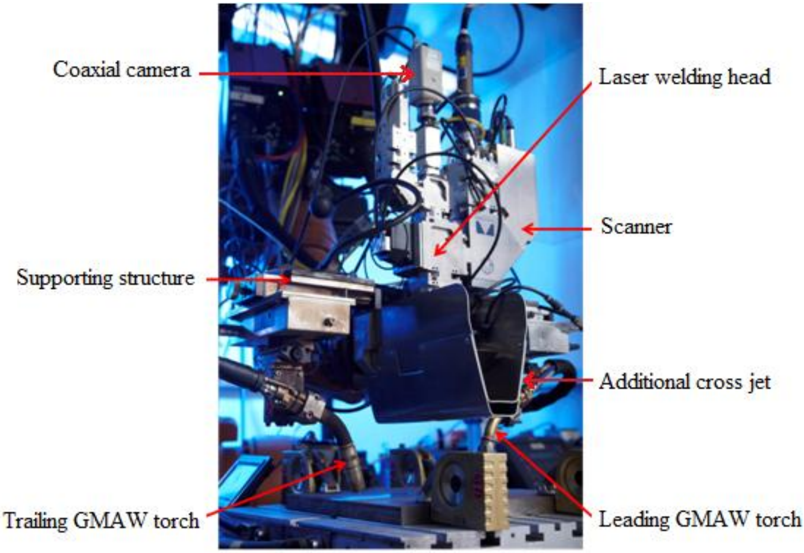

Adapted from: [8]

The collimating and focusing lenses have a focal distance of 150 mm and 300 mm respectively, resulting in a magnification ratio of 2:1. This way, the beam focus diameter with 200 µm and 300 µm optic fibers is 400 µm and 600 µm respectively. Beside the two lenses, the optical path, depicted in figure 3.2, is also comprised of two mirrors. The first one is coupled to the scanner and is responsible for the oscillatory movement of the laser beam. The second mirror is used to deflect the beam by 90° and to allow light from the process zone to reach the coaxial camera.

Figure 3.2: Optical path of the HYBRILAS welding head.

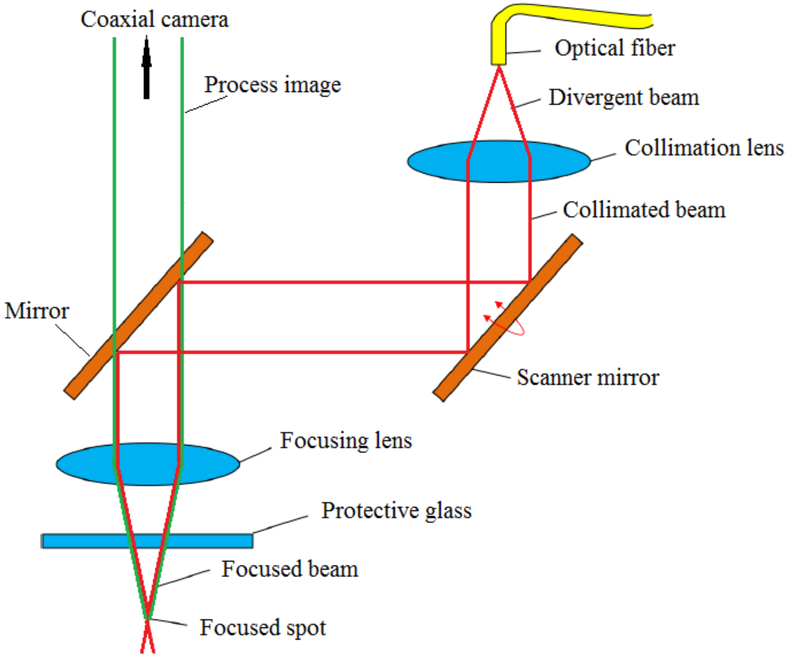
Coaxial camera
Process image
Optical fiber
Divergent beam
Collimation lens
Collimated beam
Mirror
Scanner mirror
Focusing lens
Protective glass
Focused beam
Focused spot

Adapted from: [94]

3.1.4 Robotic Arm

The HYBRILAS welding head is mounted on a six axis KR 60 HA robotic arms from KUKA Roboter GmbH. It has a repeatability of less than ±0.05 mm and support loads of up to 60 kg.

3.1.5 Weld Monitoring System

The first GMAW torch is monitored by a HKS WeldScanner system, capable of 3200 measurements per second. Measurement of the electric current and voltaeg is done with the HKS – P1000 module, which is able to measure up to 1000 A and 100 V with an accuracy of ±1%. The module HKS – GM 30L 10B can measure up to 30 l/min of shielding gas flow with ±3%.

3.2 MATERIAL

3.2.1 Plates

API 5L grade X70 pipeline steel is the material of the specimens. The composition of this steel is presented in table 3.2.

Table 3.2: API 5L X70 steel composition.

C	Si	Mn	P	S	Al	Cu	Mo
0.094	0.362	1.761	0.015	0.0024	0.031	0.008	0.001

Ni	Mo	V	As	Sn	Ti	Nb	Mg
0.007	0.001	0.003	0.002	0.001	0.020	0.056	0.0001

Ca	B	Pb	W	Zr	Mg	N
0.0013	0.0001	0.001	0.003	0.001	0.0001	0.0005

The experiment consists of welding two plates together along their length. Each plate measures 350 mm length and 140 mm width. The thickness is 23 mm. Plain milling is done on the sides to be welded and a handheld milling device is used to bevel the edges. Figure 3.3 shows the geometry of the plates and the chamfer geometry on the edges.

Figure 3.3: Specimens geometry and edge preparation.

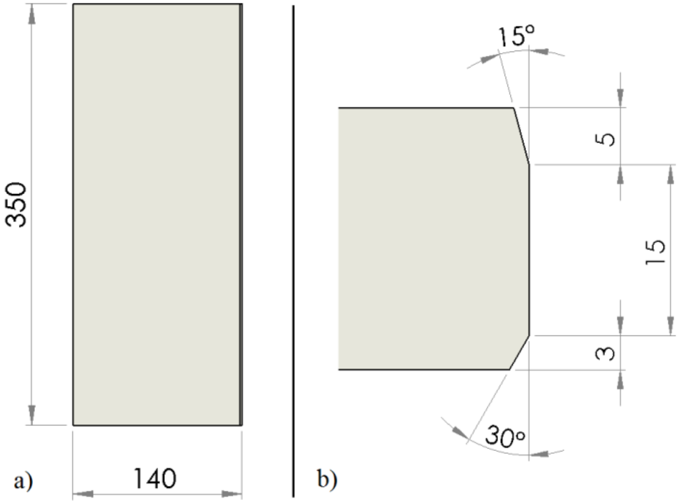

Source: The author

3.2.2 Filler Metal

Two different filler metals were used for the experiments. Most of the plates were welded with NiMo 1-IG and one weld was made with G4Si1, both with a diameter of 1.2 mm. Their compositions can be found in table 3.3.

Table 3.3: Filler metals composition in mass percentage.

	G4Si1	**NiMo 1-IG**
C	0.06-0.14	0.12
Si	0.80-1.20	0.40-0.80
Mn	1.60-1.90	1.30-1.90
P	0.025	0.015
S	0.025	0.018
Ni	0.15	0.80-1.30
Cr	0.15	0.15
Mo	0.15	0.25-0.65
V	0.03	
Cu	0.35	0.30
Al	0.02	
Ti+Zr	0.15	

3.2.3 Shielding Gas

The shielding gas is delivered to both welding pools through the GMAW torches. It is the mixture ISO 14175 M21, composed of 82% argon and 18% carbon dioxide, produced by Messer Group GmbH under the name of Ferromix C18.

A small cut was done in the gas nozzle of the leading arc torch to allow the passage of the laser beam, since it stays in the beam path in the welding configuration. A picture of the cut nozzle is presented in figure 3.4.

Figure 3.4: Nozzle used for the leading GMAW torch with a cut to allow the laser beam pass.

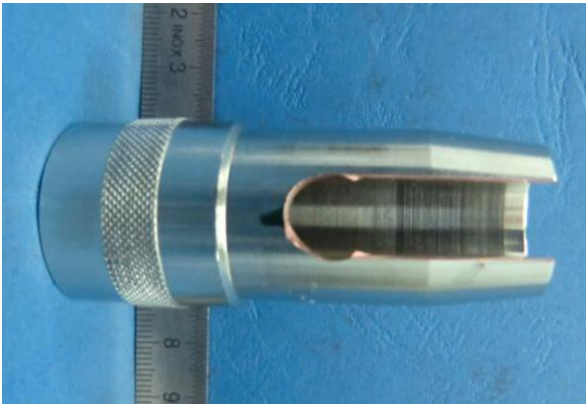

Source: [94]

4 EXPERIMENTAL PROCEDURE

4.1 PROCESS GEOMETRY

The experimental rig developed in the scope of the HYBRILAS project consists of three heat sources: one 16 kW laser beam and two GMAW torches. One of the arc torches leads the laser beam 3 mm ahead. As they act on the same molten pool, they form a hybrid process. The other torch is located 120 mm behind and acts on a discrete molten pool, forming a combined process with the laser. So the process developed in the HYBRILAS research project is a hybrid laser – GMA combined with a GMAW process.

The focal spot of the laser and the tip of the first GMAW torch wire with a stick-out length of 12 mm are placed at the bottom of the groove. The second torch is found on the top surface of the plate with the same stick-out length. Both torches are inclined by 20° to the vertical, with the leading torch in the backhand position and the trailing torch in the forehand position. The laser shines orthogonally to the plates and all three sources are lined up in the welding direction. Figure 4.1 shows the position of the heat sources on the plates.

Figure 4.1: Geometrical arrangement of the heat sources.

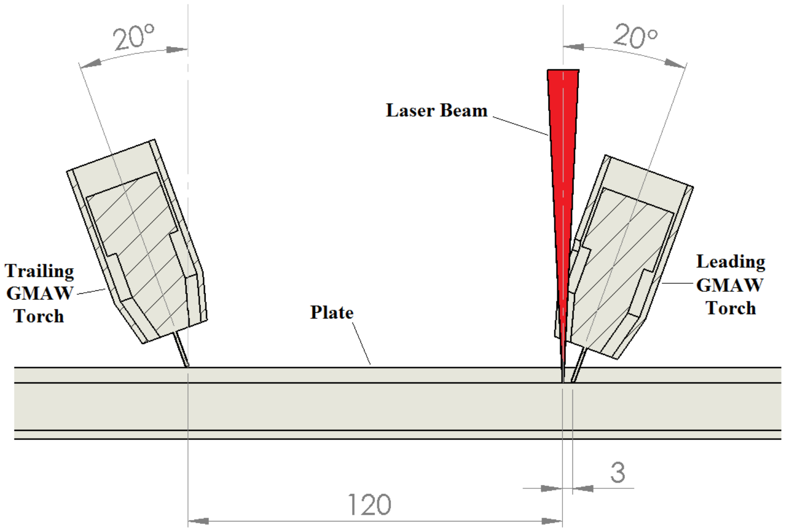

Source: The author

4.2 TESTS PREPARATION

The top and bottom surfaces of the plates are submitted to sand blasting to remove rust and dirt and the lateral faces to be welded cleaned with brake cleaner. The plates are then fixed to the welding table by the use of 62 mm Monobloc tensioners from Kopal with a torsional moment of 75 Nm. A start plate and a stop plate are also placed on the welding table to allow better usage of the specimens length. The fixed plates ready to be welded are shown in figure 4.2. Start and stop plates were not welded to the specimens in these tests, despite what figure 4.2 shows.

For a precise alignment of the laser in the welding position the coaxial camera is used.

Figure 4.2: Plates positioned and ready to be welded.

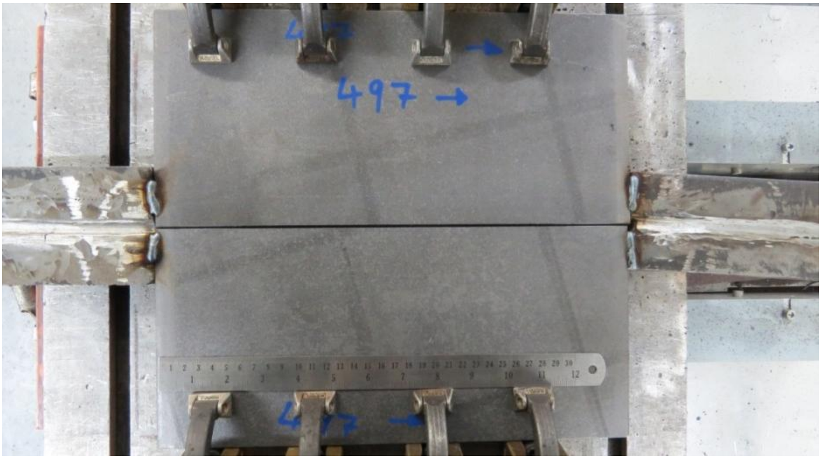

Source: The author

To avoid excessive leakage of molten metal from the weld root, a copper profile filled with OP 10U (EN 760: SA CS 1) backing flux from Oerlikon was used as a weld seam support, as depicted in figure 4.3. The flux constitution is found on table 4.1.

Figure 4.3: Weld bead support.

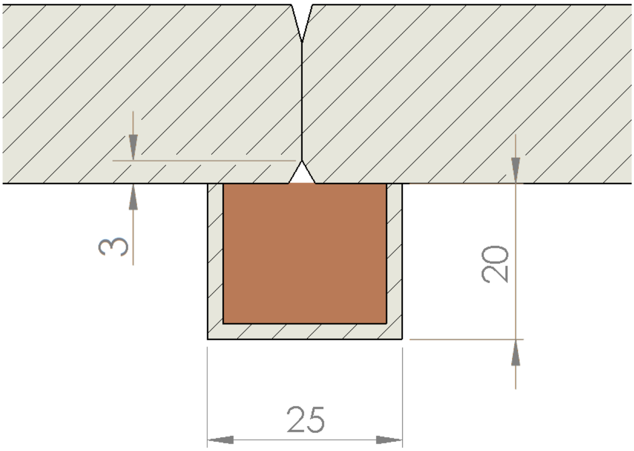

Source: The author

Table 4.1: Backing flux composition used in the weld seam support.

CaO + MgO	35 %
$SiO_2 + TiO_2$	32 %
CaF_2	7 %
$Al_2O_3 + MnO$	5 %

4.3 PARAMETERS

Seven parameter combinations were used in the welds in the scope of this work, as shown in table 4.2. For clear understanding, each weld seam will be labeled by a letter and a number. The letter indicates which parameters were used and the number indicates its order among other welds with the same parameters. “A1” for example refers to the first weld seam produced with the parameters labeled as “A” in table 4.2.

To change the beam width, two different optical fibers were used, one with 200 µm and the other with 300 µm diameter. The magnification ratio of 2:1 from the laser head results in a beam width of 400 µm and 600 µm respectively, as the beam is focused on the material surface. Since the lenses remain the same, the divergence angle does not change.

Table 4.2: Parameter combination for the welds.

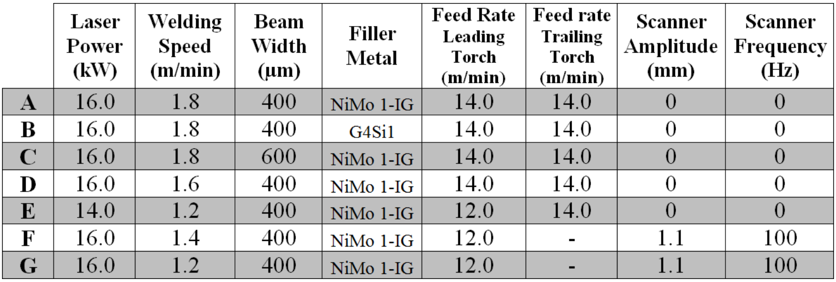

	Laser Power (kW)	Welding Speed (m/min)	Beam Width (µm)	Filler Metal	Feed Rate Leading Torch (m/min)	Feed rate Trailing Torch (m/min)	Scanner Amplitude (mm)	Scanner Frequency (Hz)
A	16.0	1.8	400	NiMo 1-IG	14.0	14.0	0	0
B	16.0	1.8	400	G4Si1	14.0	14.0	0	0
C	16.0	1.8	600	NiMo 1-IG	14.0	14.0	0	0
D	16.0	1.6	400	NiMo 1-IG	14.0	14.0	0	0
E	14.0	1.2	400	NiMo 1-IG	12.0	14.0	0	0
F	16.0	1.4	400	NiMo 1-IG	12.0	-	1.1	100
G	16.0	1.2	400	NiMo 1-IG	12.0	-	1.1	100

Filler metal feed rate had to be reduced at slower welding speeds to avoid excessive material deposition. Material transference from the trailing torch was not smooth for feed rates below 14.0 m/min, so the reduction was made at the leading torch only.

Both arc sources are set to induce a pulse spray metal transfer mode.

4.4 X-RAY

Some of the welds with parameters A, B and C were sent to SLV Halle GmbH for detection of pores and cracks through X-ray imaging.

The first 20 mm and the last 30 mm of the specimens are not considered, because of instabilities at the start and at the end of the weld seam. The remaining 300 mm length was divided either into five 60 mm long zones or into six 50 mm zones. For each zone, the following data was determined:

- Length of the shortest crack;
- Length of the longest crack;
- Whole length of cracks;
- Number of pores;
- Largest pore diameter.

For easier comparison of samples from different lengths, crack length per weld length (C/W) and pores per weld length (P/W) were defined. C/W is the total crack length found in a defined weld length divided by that weld length and P/W (mm^{-1}) is the amount of pores found in a defined weld length divided by that weld length.

4.5 METALLOGRAPHIC IMAGES

Two samples were produced for each weld seam for the metallographic analysis, one 50 mm after the beginning of the weld and the other 50 mm before the end of the weld. They were prepared and observed through an optical microscope. They were also photographed at a small angle with directed lighting to highlight the defects.

4.5.1 Bulge and Solidification Flaw Depth

Defining the bulge depth (h_B) is not a trivial task, as it is an extensive feature with no clear boundaries and center. Defining at which point it should be measured is important to achieve consistent values.

In the scope of this work, the measurement was taken at the point where the swelling first reaches its highest width from the top surface, as depicted in figure 4.4. In the few cases where more than one bulge could be observed, the upper one was used. This point was defined for measurements because it was considered most important how steep the widening of the molten pool is from a minimum, found above the bulge, to its maximum width at the swelling, and that steepness is better represented using this point.

Figure 4.4: Solidification flaw (h_F) and bulge (h_B) depth definition.

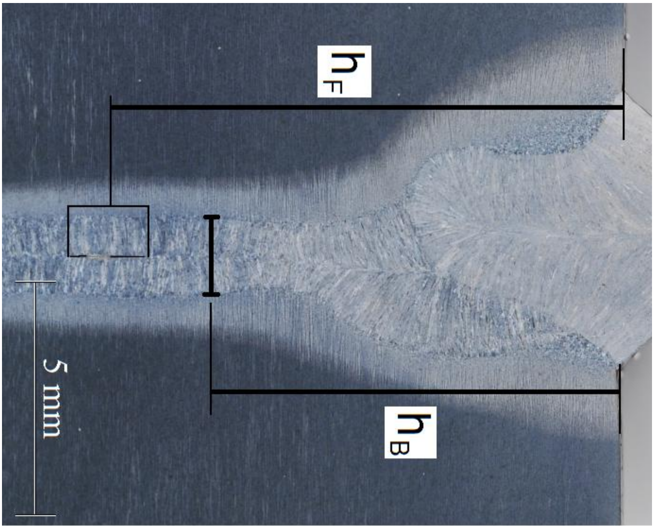

Source: The author

The solidification flaw boundaries are much simpler to define than for the bulge. The depth (h_F) was defined at the midpoint of the solidification flaw height.

4.5.2 Bulge Widening Angle

The solidification flaw formation is strongly affected by the geometry of the molten pool, especially by bulges. To evaluate how severe a bulge is, the bulge widening angle was defined, figure 4.5.

Figure 4.5: Method for bulge widening angle determination.

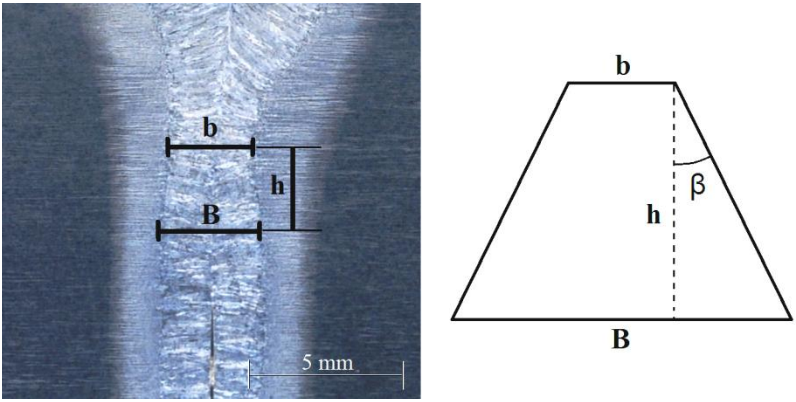

Source: The author

Bulge widening angle (β) is the angle between a leg and a line perpendicular to the bases of an isosceles trapezium, of which the smaller base length (b) is the width of a constriction in the molten pool, the bigger base length (B) is the maximum width of a swelling in the molten pool and the height (h) is the distance between them.

The point where the width and depth of the bulge are taken are the same used before for the bulge depth, at the position where the first bulge first reaches its maximum width, since the solidification flaws were always related to the first bulge in the analyzed specimens.

Because the solidification is expected to be completed faster at the bottom of the molten pool and later at the upper side, the constriction above the bulge is used for calculation and not the constrictions below it, if there is any. Considering that the solidification flaw is caused to some degree by lack of material due to solidification shrinkage and that the solidification happens from the bottom to the top, only the constriction above a swelling in the molten pool can disturb the back flow of material to compensate for the shrinkage, since the material below the bulge should be already totally or mostly solidified, regardless of the presence of a constriction. The material above, on the other hand, is expected to take longer to solidify, unless a constriction is present, a region with less thermal energy and hence faster solidification, which could then interfere with the molten metal backfilling.

Width and depth of the constriction are taken at its narrowest point. In the case that its narrowest width remains constant for some depth, the deepest point with the narrowest width is considered, as it is closer to the bulge, giving a better representation of how steep the molten pool widens at the bulge.

4.5.3 Porosity Evaluation

Each pore was classified for its location and shape.

The weld cross section was divided into four zones (figure 4.6):

- Leading GMAW torch;
- Trailing GMAW torch;
- Laser;
- Root reinforcement.

The leading GMAW torch zone and the laser zone are defined as the arc zone and the laser zone from the hybrid welding molten pool. At the bottom of the weld is the root reinforcement zone, defined as the region inside and below the bottom chamfer. Finally, the trailing GMAW torch zone is the molten pool formed by that same torch alone.

Figure 4.6: Definition of the four zones in the cross section view of the weld bead.

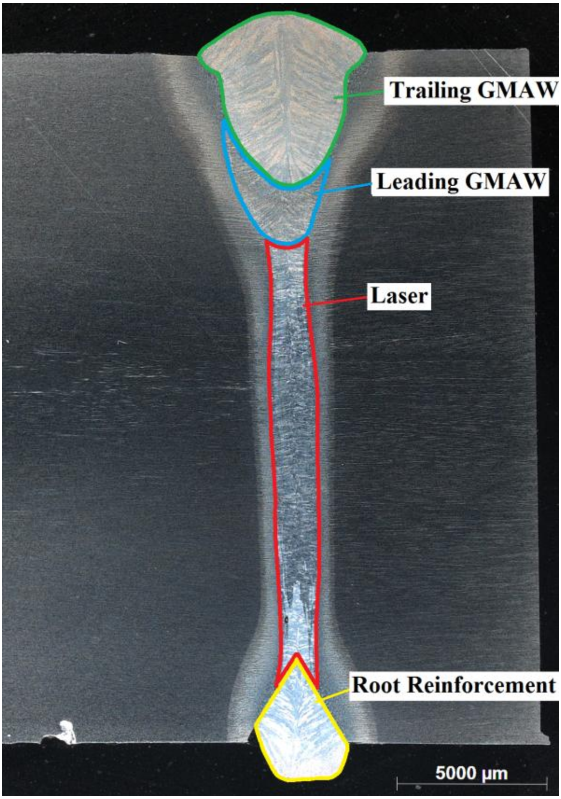
Trailing GMAW
Leading GMAW
Laser
Root Reinforcement
5000 µm

Source: The author

5 RESULTS AND DISCUSSION

5.1 SOLIDIFICATION FLAW

5.1.1 Focal Spot Size and Filler Metal

The X-ray results for crack detections are present in table 5.1.

Table 5.1: X-ray imaging results for cracks detection showing the accumulated crack length, the C/W and the longest crack for the first half (1/2), second half (2/2) and total length (Total) of the weld seams.

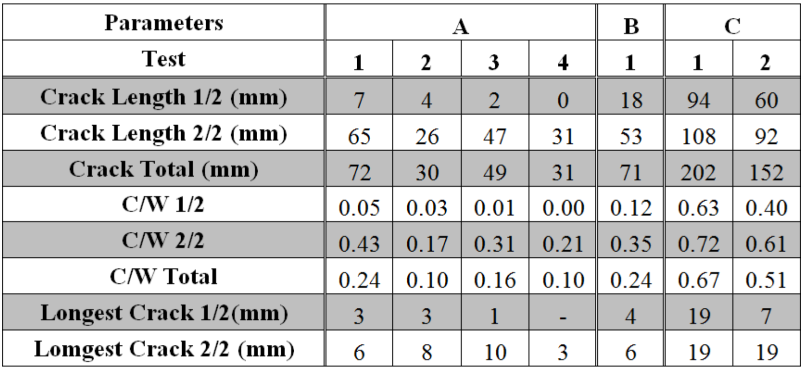

Parameters	A				B	C	
Test	1	2	3	4	1	1	2
Crack Length 1/2 (mm)	7	4	2	0	18	94	60
Crack Length 2/2 (mm)	65	26	47	31	53	108	92
Crack Total (mm)	72	30	49	31	71	202	152
C/W 1/2	0.05	0.03	0.01	0.00	0.12	0.63	0.40
C/W 2/2	0.43	0.17	0.31	0.21	0.35	0.72	0.61
C/W Total	0.24	0.10	0.16	0.10	0.24	0.67	0.51
Longest Crack 1/2(mm)	3	3	1	-	4	19	7
Lomgest Crack 2/2 (mm)	6	8	10	3	6	19	19

All the cracks detected by the x-ray are found in the weld centerline and are short, with the longest cracks measuring 19 mm. Those are typical solidification flaw characteristics. Metallographic images from these tests and others with similar parameters showed only solidification flaws and no hot or cold cracks. For this reason, every crack detection made by the X-ray will be considered a solidification flaw, as it should be mostly accurate.

As it can be seen in table 5.1, the ends of the welds show much more solidification flaws than the beginnings. Further investigations with non-full penetrating welds with the same fixing system showed a gap width variation along the weld direction, with zero gap at the beginning of the weld and up to 0.5 mm at the end, probably caused by the thermal loads during the process. That shows that the gap width plays an important role in solidification flaw formation. To minimize its influence on the results, only the first half of the specimens were used for further analyzes in this work.

Slight more solidification flaws were observed with the G4Si1 filler wire than with the NiMo 1-IG. If the solidification flaw formation mechanism is a localized lack of material in the solidifying molten pool, the viscosity of the molten steel can be an important factor as it is harder for a more viscous fluid to flow and fill the lack of material. Korolczuk-Hejnak and Migas [95] observed that silicon influences the molten steel viscosity and its content is higher in the G4Si1 filler wire. Silicon is also believed to be a solidification crack inducing element, since Metzbower *et al* [96] observed a high amount of silicon at the surface of solidification cracks on laser welding of steel.

Sulfur, phosphorus and manganese are important alloying elements on solidification crack formation [80]. The G4Si1 has slight more of the detrimental sulfur and phosphorus, while the manganese content can be a bit higher. Using the mean values found in table 3.3, the Mn/S ratio is 70 for G4Si1 and 107 for NiMo 1-IG. That makes the weld with the G4Si1 filler metal somewhat more sensitive to hot cracking, although both of them are pretty high inside the crack resistant zone from figure 2.19, as does the base metal, with a Mn/S ratio of 733.

No significant difference was observed at the measured arc current and tension for both filler metals. So it is less likely that the electric arc is a major influencing factor for the solidification flaw increase with the G4Si1 wire.

The tests C, done with the similar parameters as tests A, but with a wider optical fiber, resulted in welds severely affected by solidification flaws. The wider optical fiber provides a bigger focal spot size, which could change the keyhole geometry and the keyhole dynamics, two of the most important factors influencing the solidification flaw formation tendency. So it can explain the high increase in the total solidification flaw length found for the wider optical fiber, despite the heat input and welding speed remaining the same.

It could be expected then that lower irradiance causes more solidification flaws, as the graphic, done with the results from the A, B and C welds, in figure 5.1 suggests. But that might not be true, since the same irradiance could be achieved by changing the focal spot position on the weld plate or by changing the lenses focal distances, yet the keyhole geometry and dynamic should be significantly different.

Figure 5.1: Crack length per weld length (C/W) as a function of laser irradiance.

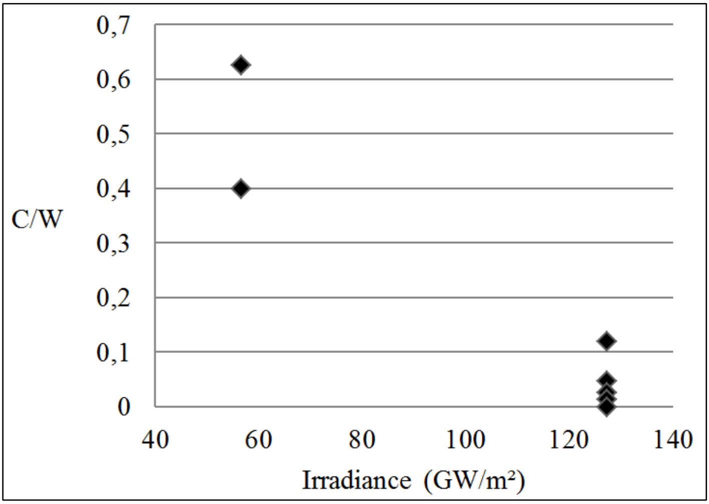

Source: The author

5.1.2 Keyhole Bulging and Solidification Flaws

5.1.2.1 Bulge and Solidification Flaw Position

In the analyzed metallographic images, the solidification flaws are always associated with a bulge in the molten pool transversal profile. Some examples are shown in figure 5.2. There was no solidification flaws observed in locations without bulging.

The depth of the solidification flaws and of the bulges were found to have respectively a mean value of 11.5 mm and 11.0 mm from the plate upper surface, reinforcing the observed relation between both.

The bulging is caused by a region in the molten pool with more thermal energy. Energy from the laser is absorbed by the keyhole mainly by inverse Bremsstrahlung in the plasma and by Fresnel absorption on the walls [97]. Since the laser beam used in these tests has a wavelength of 1.03 µm, the absorption by the plasma (inverse Bremsstrahlung) is lower and the beam multiple reflections at the keyhole walls plays an important role at the energy distribution along the keyhole depth. Laser absorption is the highest at the bottom of the keyhole for Fresnel absorption only models [98-100], but some simulations also observed local increased absorption higher in the keyhole, like in the simulation from Jin *et al* [100], shown in figure 5.3.

Figure 5.2: Cross sectional metallographic images of welds with solidification flaws.

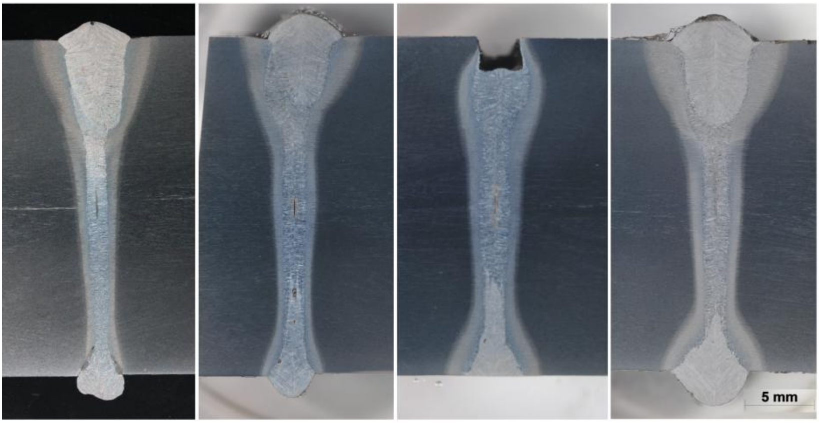

Source: The author

Figure 5.3: The average laser intensity absorbed along keyhole depth (X).

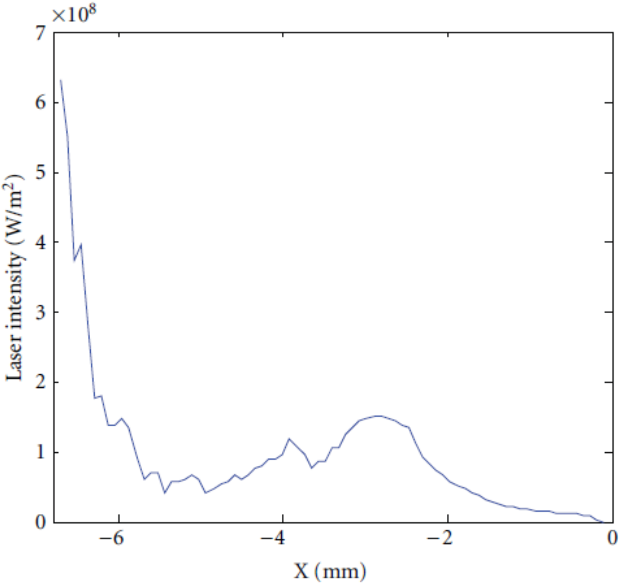

Source: [100]

Keyhole shape, focus position, divergence angle, intensity profile and polarity should be the most important factors on the laser energy absorbed distribution along the keyhole depth. Except for keyhole shape, none of these parameters were changed in any of the tests. Even the keyhole shape is not believed to change much between the tests. For this reason the bulge position is not expected to vary greatly between the tests. The measured bulge depth showed a standard deviation of 1.4 mm, which is considerably low, as it is less than 10 % of the total weld penetration. It is also important to notice that the bulge depth varies randomly along the same weld seam, as it can be seem in figure 5.4, so this obtained deviation might be more due to the random variation than to parameter induced variation. Solidification flaw, on the other hand, showed a more constant depth, varying between 10.4 mm and 12.5 mm with a standard deviation of only 0.5 mm.

Figure 5.4: Cross sectional metallographic image showing the molten pool geometry varying along the same weld seam.

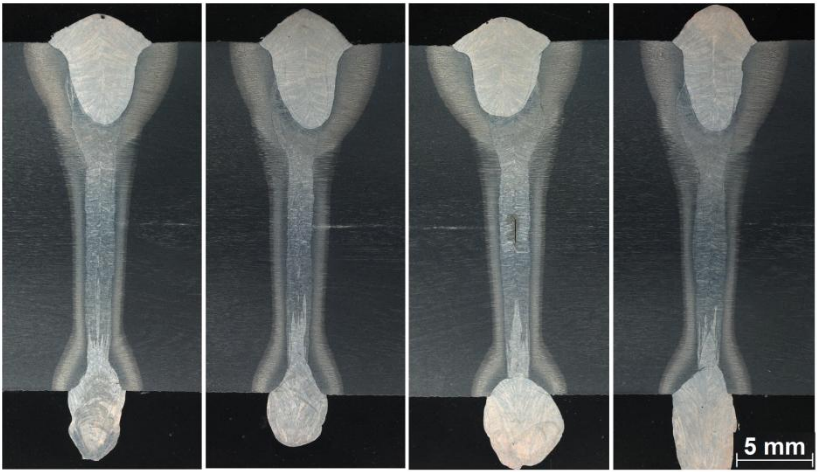

Source: The author

5.1.2.2 *Bulge Widening Angle and Solidification Flaw*

A relation was observed between the bulge widening angle and the solidification flaw formation comparing the x-ray results with the metallographic images. Figure 5.5 shows the obtained results for the total solidification flaw length per weld length (C/W) as a function of the bulge widening angle using the mean values found for the tests with same parameters. The tests with the 300 µm optical fiber, which were much more severely affected by solidification flaws, show a mean bulge widening angle more than two times bigger than for the other tests.

Figure 5.5: Total crack length per weld length (C/W) as a function of the bulge widening angle.

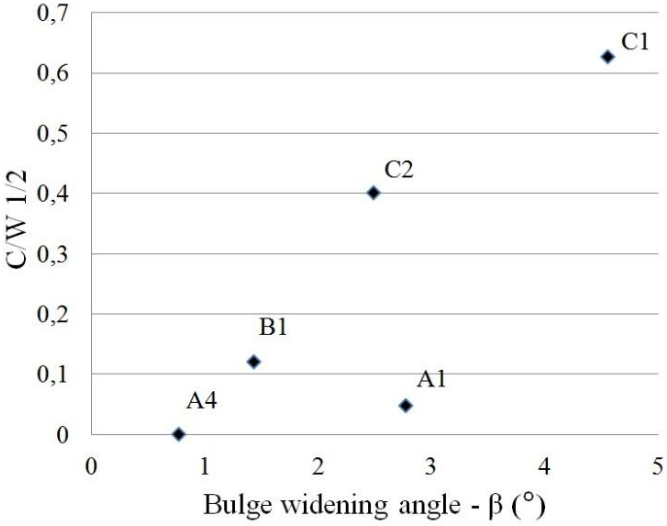

Source: The author

The weld with G4Si1 filler wire showed more solidification flaws than the welds with NiMo 1-IG, despite the slight smaller angle. That might be explained by the already mentioned possible difference in viscosity for both metals. If the G4Si1 is more viscous, it should be more prone to solidification flaw formation for the same bulge widening angle.

5.1.3 Metallographic Images from Parameters D, E, F and G

The metallographic images from the tests with parameters D, E, F and G were analyzed regarding the bulge widening angle and the presence of solidification flaws. It should be noted however that only one weld was done for each of those parameters, except for parameter

D, which had two. For this reason, the results discussed next should be taken with caution.

5.1.3.1 Parameters D

These welds were done with similar parameters to A, but with slower welding speed, 1.6 m/min instead of 1.8 m/min, and two cross sectional cuts are shown in figure 5.6. No solidification flaws were observed in any of the four images taken for the welds with parameters D.

Figure 5.6: Cross sectional view metallographic images from the beginning of weld D1 (a) and from the end of weld D2 (b).

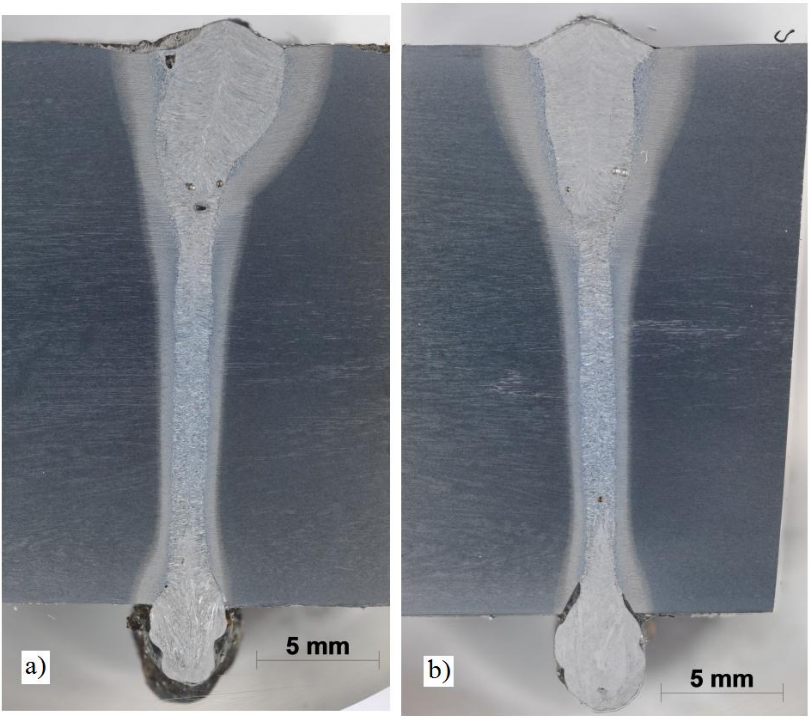

Source: The author

The bulge widening angle showed a mean value of **2.05 °**. It is somewhat higher than the one found for parameters A, **1.52 °**, which showed the fewest solidification flaws in the X-ray images, but the slower welding speed and higher heat input result in slower solidification, thus giving more time for molten metal to backfill the volume loss by solidification and thermal shrinkage.

Without X-ray images, it is not possible to analyze with confidence the effects of reducing the welding speed and increasing the laser heat input (533 kJ/m to 600 kJ/m) had on the formation of solidification flaws. From what has been observed through the metallographic images, it is not expected that the welds done with parameters D have a high amount of solidification flaws.

5.1.3.2 Parameters E

Figure 5.7 shows the metallographic images of the cross section from the beginning and from the end of the weld done with parameters E, with 14 kW laser beam power and 1.2 m/min welding speed. The first cut (figure 5.7 (a)) presented a solidification flaw, which is clearer in the image with special lighting, in figure 5.8.

he measured mean value for the bulge opening angle is **3.66 °**, similar to that found for the very solidification flaw sensitive parameters C, **3,52 °**. The reduced welding speed can compensate somewhat for the severe bulge, but it is probably not enough to fully eliminate solidification flaws, since one was observed.

In this case, decreasing the welding speed (1.8 m/min to 1.2 m/min) and increasing the laser heat input (533 kJ/m to 700 kJ/m) supposedly had a negative effect on the solidification flaw formation, in comparison with the welds done with parameters A.

Figure 5.7: Cross sectional view metallographic images of the beginning (a) and of the end (b) of the weld done with parameters E.

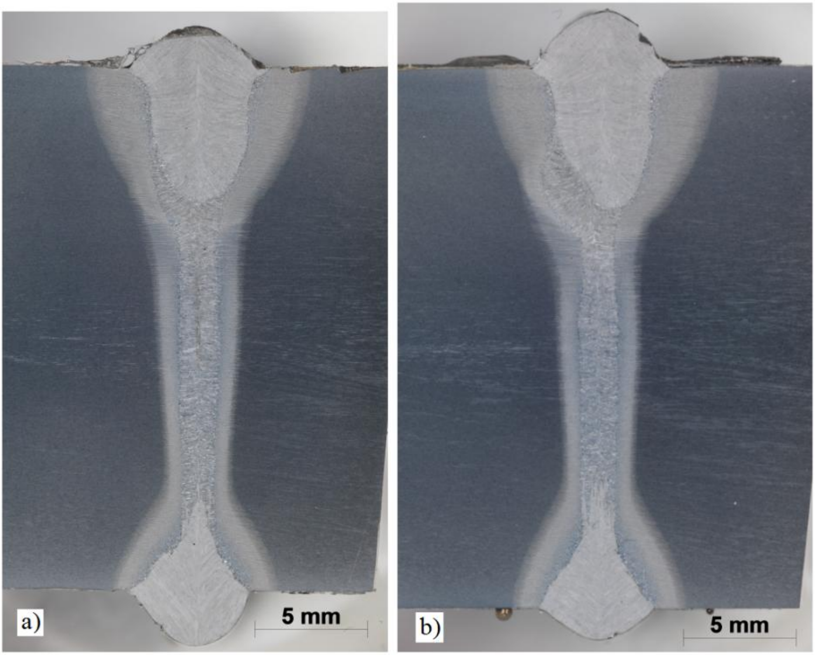

Source: The author

Figure 5.8: Cross sectional image with defect highlighting of the weld with parameters E.

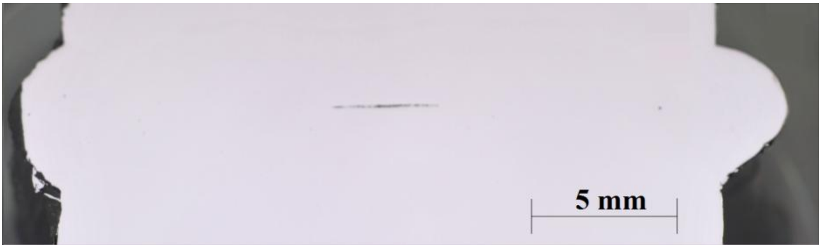

Source: The author

5.1.3.3 Parameters F and G

Tests F and G were done to investigate the effect of using a high frequency transverse beam oscillation, which results in welds with higher heat input and slower welding speed that should be less susceptible to solidification flaws due to a reduced temperature gradient [89, 91]. The parameters combinations differ from each other in the welding speed, F is 1.4 m/min and G is 1.2 m/min, resulting in a laser heat input of 686 kJ/m and 800 kJ/m respectively. Figure 5.9 and figure 5.10 show the cross sectional view of the resulting welds.

Figure 5.9: Cross sectional view metallographic images of the beginning (a) and of the end (b) of the weld done with parameters F. (c) and (d) show with special lighting the solidification flaws found at the beginning and at the end of the weld respectively.

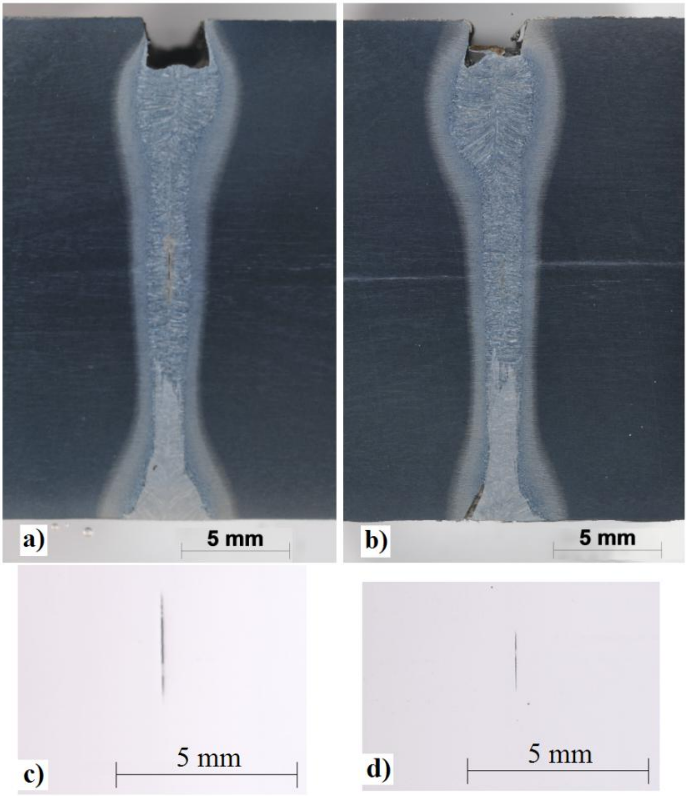

Source: The author

Figure 5.10: Cross sectional view metallographic images of the beginning (a) and of the end (b) of the weld done with parameters G.

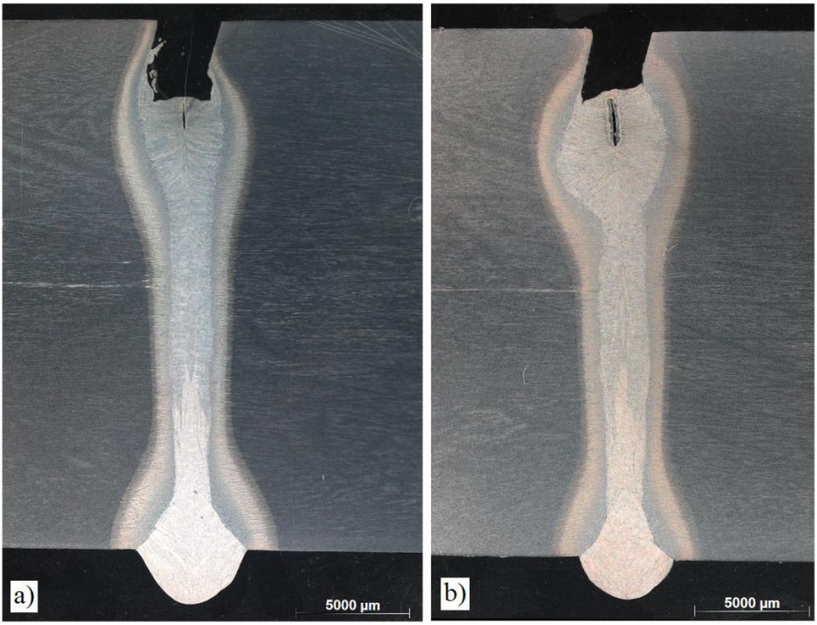

Source: The author

Despite the parameters being very similar, the results for them are pretty different. The faster welding (F) resulted in a worse weld geometry, with a mean bulge widening angle of **2.8 °**, considered high for what has been observed in this work. That can explain the presence of solidification flaws in both cross sectional cuts of that weld

The slower welding (G), on the other hand, showed a much gentler profile with a mean bulge widening angle of only **1.6 °**, close to the angle observed with parameters A, the best welds examined through X-ray. No solidification flaw could be detected in the metallographic images. In this case, the slower welding speed and higher laser heat input seems to be beneficial.

The weld done with parameters G showed however a different defect in the middle of the leading GMAW torch zone. Closer observation of the microstructure around that defect showed that the growth of the upper grains had a downward component, suggesting that the upper surface of the weld bead solidified while there was still molten metal beneath it, as illustrated in figure 5.11. This effect acts similarly to the contraction above a bulge in the laser dominated region of the molten pool, limiting the molten metal backfilling for shrinkage compensation. Hence this defect might be a solidification flaw or have a similar development to it.

Figure 5.11: Cross sectional view of the weld defect from the weld with parameters G (a) and representation of the solidification process (b).

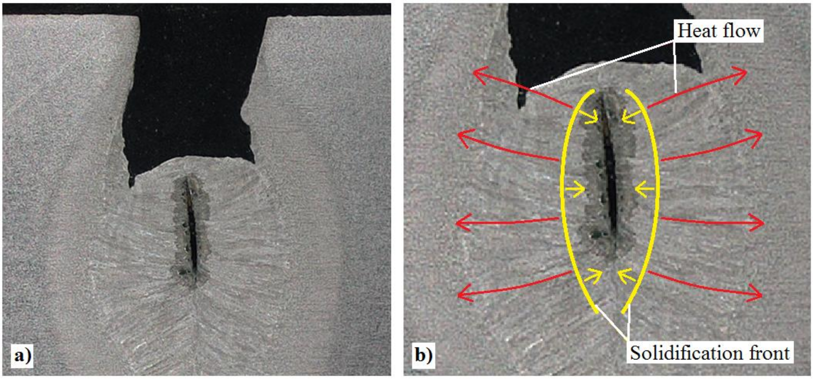

Source: The author

The weld bead support did not provide enough support for the molten metal, so a good amount of material flowed downward to the root reinforcement and lacked in the upper side. This effect was more severe in the weld G, because of the slower welding speed and the higher heat input. As a result, a more severe underfill occurs in this case, which increases the tensile stresses and can cause the aforementioned effect of a downward solidification in the upper region of the molten pool.

5.1.4 Solidification Flaw Formation Mechanism

There are two main explanations to how the solidification flaws are formed, as a solidification crack or as a shrinkage pore. Those two formation mechanisms should result in different characteristics, since the first one is an intergranular crack and the second exhibits a freely solidified surface with no deformation [86].

Researchers have been working hard to identify the signs of those two formation mechanisms. Jüptner *et al* [101] have found indications that solidification flaw is created by the solidification cracking mechanism on their experiments with laser welding of steel, since the two surfaces of the defect seem to fit each other, one is approximately the negative of the other, as can be seem in figure 5.12, indicating an intergranular crack.

Figure 5.12: Solidification flaw formed as a solidification cracking.

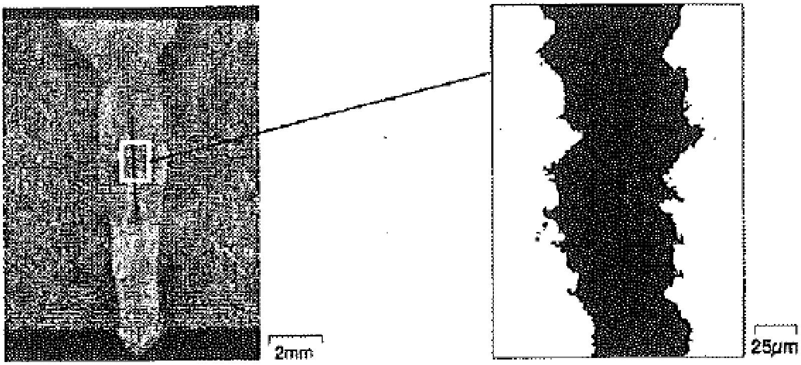

Source: [101]

Free of deformation surfaces were also observed on solidification flaws [102-104]. Scanning electron microscope (SEM) imaging of solidification flaw surfaces showed structures free of deformation, figure 5.13, and energy-dispersive X-ray spectroscopy (EDS) analysis of the same surfaces showed no accumulation of hot crack inducing elements [102, 103], which leads to the belief that these solidification flaws are caused by lack of material during solidification, shrinkage porosity.

In the welds done for the present work, many solidification flaws showed clear characteristics of intergranular cracks, as shown in figure 5.14, so they are most probably result of solidification cracks rather than shrinkage porosity. Some others are not so clear, they are wider and the opposing surfaces seem to have some fitting, but the resolution obtained with the used optical microscope is not enough to determine if they are really intergranular cracks or shrinkage porosity, like in figure 5.15.

Figure 5.13: SEM image of a solidification flaw surface with shrinkage porosity characteristics in a laser beam weld.

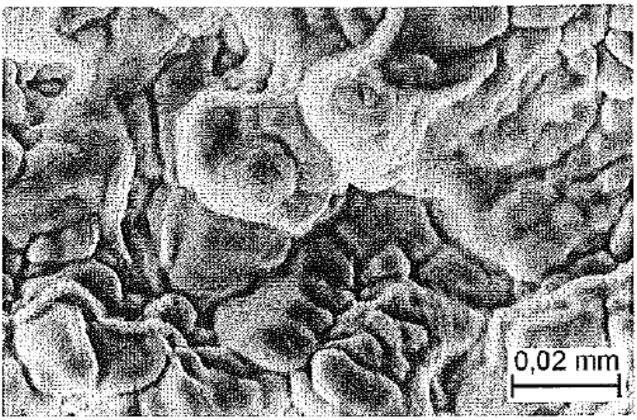

Source: [102]

Figure 5.14: Solidification flaw exhibiting solidification crack characteristics.

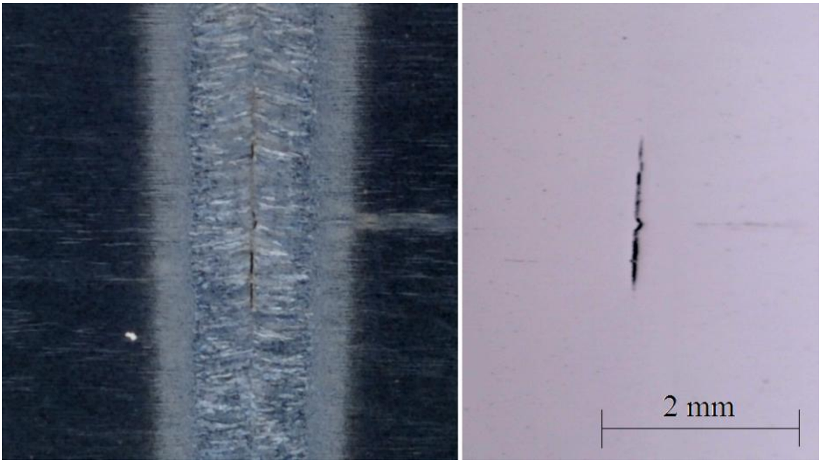

Source: The author

Figure 5.15: Solidification flaw with no clear sign whether it is a solidification crack or a shrinkage pore.

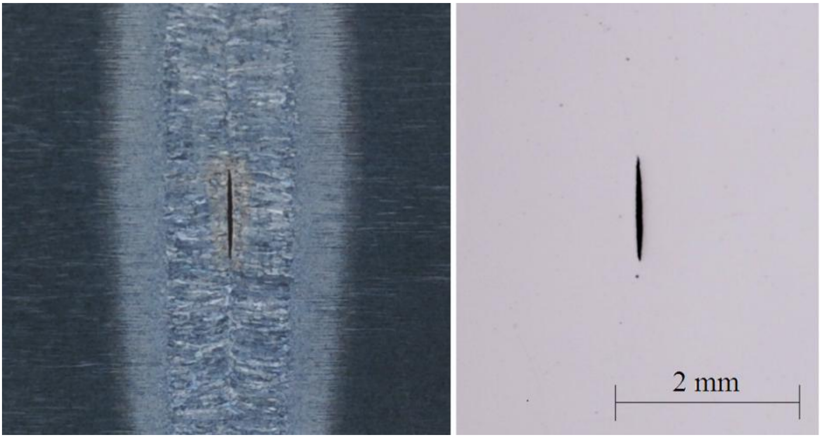

Source: The author

Since strong evidence was found for both shrinkage porosity and solidification cracking, there should be an explanation that agrees with both. One possibility is that under different conditions one of two different defects might appear: a solidification crack or a shrinkage pore. If that is the case, those two defects would have very similar characteristics that make it difficult to tell them apart, but they would be two distinct defects.

Another possibility is that they can happen simultaneously. First a shrinkage pore would be formed. That pore would act as a stress concentration that could deflagrate a crack. The shrinkage pore could also be very small, arising as a little void when lower melting point compounds form a liquid film between the solidification fronts. That void would cause stress concentration and make the weld more sensitive to solidification crack. The resulting solidification flaw would show mostly solidification crack characteristics, even though a pore was also involved in its development.

This explanation agrees well with the fact that every solidification flaw observed during the development of this research is related to a bulge in the molten pool width, as it is a location sensitive to shrinkage porosity formation. Solidification crack alone on the other hand happens when a thin liquid film is present between the two solidification fronts in a region under sufficient tensile stress, which is not necessarily in the bulged area. The bulge region can even be relatively resistant to solidification crack, because solidification is completed just above and below it, and that already joined area can resist the tensile stresses. So the crack would most probably appear outside of the bulge if stress concentration was not present, not within the bulge.

5.2 POROSITY

5.2.1 Focal Spot Size and Filler Metal

The same X-ray images used for crack (solidification flaw) detection were also analyzed for porosity. Table 5.2 shows the pore quantities, the porosity per weld length (P/W) and the diameter of the largest pore for the first half (1/2), second half (2/2) and the whole weld length (Total).

Table 5.2: X-ray imaging results for cracks detection showing the accumulated crack length, the C/W and the longest crack for the first half (1/2), second half (2/2) and total length (Total) of the weld seams.

Parameters	A				B	C	
Test	**1**	**2**	**3**	**4**	**1**	**1**	**2**
Porosity 1/2	5	15	13	6	21	6	2
Porosity 2/2	1	6	1	2	5	5	3
Porosity Total	6	21	14	8	26	11	5
P/W 1/2 (mm^{-1})	0.03	0.10	0.09	0.04	0.14	0.04	0.01
P/W 2/2 (mm^{-1})	0.01	0.04	0.01	0.01	0.03	0.03	0.02
P/W Total (mm^{-1})	0.02	0.07	0.05	0.03	0.09	0.04	0.02
Largest Pore (mm)	0.4	1.0	1.0	1.4	1.0	0.6	0.4
Largest Pore (mm)	0.6	0.6	1.0	0.6	0.6	0.6	0.4

Like it was observed for solidification flaws, the gap width seems to also have a high influence on porosity formation, but contrary to before, wider gaps appear to be beneficial, as they result in welds with reduced porosity. Again, only the first half of the weld seams were used for further analyzes to reduce the gap influence on the results.

The weld with G4Si1 filler metal and 200 µm optical fiber (B) showed the highest porosity, while the tests with NiMo 1-IG filler metal and 300 µm optical fiber (C) achieved the best results, with less and smaller pores. Metallographic images help to better understand what happened in those tests.

Figure 5.16 (a) shows the upper region of the weld seam from test B1. Amorphous pores are present in the arc zone of the hybrid welding. The same kind of porosity was observed in some tests with parameters A (figure 5.16 (b)), but none could be found at the welds done with the 300 µm optical fiber (figure 5.16 (c)).

Figure 5.16: Cross section view of the upper region of the weld seam, showing the porosity in the leading GMAW torch zone for tests with parameters A (a) and B (b), but not with C (c).

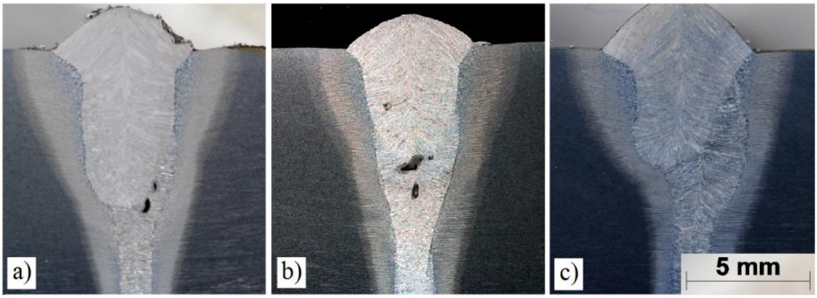

Source: The author

A weld with the same parameters as A was performed without the trailing GMAW torch and the result is presented in figure 5.17. It is clear from that test that porosity can be quite severe in the first torch region. However the second torch remelts most of this area, leaving just a small portion of those pores.

The porosity formation at the first torch zone is probably caused by contamination of the surrounding atmosphere by air. Three factors are suspected of causing disturbances in the shielding gas flow that would allow such contamination in the leading torch molten pool: the cut nozzle, the cross jet and the laser keyhole plume.

The cut made in the nozzle to achieve the desired approximation between the GMAW torch and the laser causes turbulence in the shielding gas flow and exposes it to the surrounding air earlier in its path, causing it to be one of the main causes of porosity in the first GMAW torch zone.

Figure 5.17: Cross section view of the leading GMAW torch zone with severe porosity.

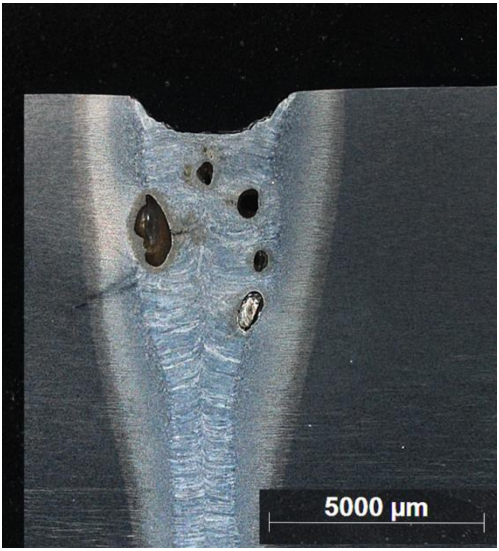

Source: The author

The cross jet used to protect the optical elements of the laser welding head is a high speed nitrogen flow that deflects particles away from the optical elements. Although not measured, it was observed that the cross jet induced winds in the process zone, a well known cause of porosity in welding. The control of flow speed was not precise, which could explain the random porosity variation found for tests with the same parameters.

Plasma and vapors leave the laser keyhole at relatively high velocities. That upward flow also disturbs the shielding gas flow and can lead to porosity formation. Since the 300 µm optical fiber results in a bigger focal spot diameter, it is expected that the keyhole inlet is wider for tests C, than for A and B. The wider inlet leads to reduced plume flow speed, which in turn reduces the shielding gas disturbance and the porosity formation for the tests with 300 µm optical fiber.

Comparing the results obtained through x-ray for solidification flaws and porosity, no relation between those two defects was evident, as can be seen in figure 5.18.

Figure 5.18: Graphic of the crack length per weld length (C/W) as a function of the porosity per weld length (P/W).

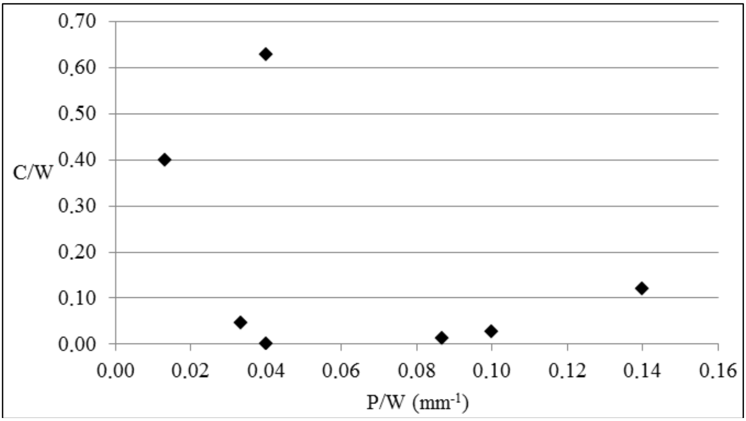

Source: The author

5.2.2 Porosity Distribution and Causes

Table 5.3 shows the fraction of pores present in each weld zone from the total observed through metallographic images and the percentage of pores in those weld zone that display an amorphous shape.

Table 5.3: Porosity distribution and shape along the four weld zones.

Weld Zone	Fraction of Total Porosity (%)	Amorphous Pores (%)
Leading GMAW torch	45	95
Trailing GMAW torch	13	33
Laser	22	10
Root Reinforcement	20	56

5.2.2.1 Leading GMAW Torch Zone

Although it comprises only a small portion of the total weld cross sectional area, it accounts for almost half of the observed porosity. As previously discussed, this might be due to the cross jet and the keyhole plume disturbance of the shielding gas flow.

Figure 5.19 shows the influence the cross-jet can have on the shielding gas flow. The nitrogen jet leaving the nozzle causes a high speed flow of nitrogen and mixed air inside the cross jet structure, which induces lower pressures at points A and B and leads to air flow in the vicinity of the laser and leading arc interaction points. Welding with increased cross-jet flow speed and the leading GMAW torch alone showed pretty severe porosity with big open pores. It shows that the cross-jet does indeed interfere with the molten pool shielding.

Figure 5.19: Transversal cut view of the cross-jet induced air flow in the working zone.

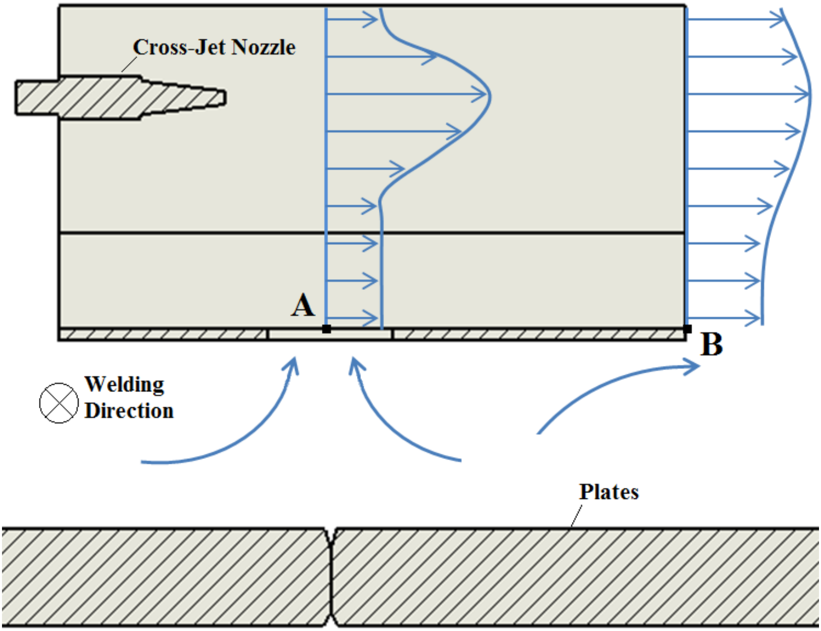

Source: The author

The keyhole plume jet moving upwards also creates a low pressure zone that can drag in air from the surrounding area directly to the molten pool or deflect the shielding gas, as shown in figure 5.20. The different results between 200 µm and 300 µm optical fibers indicate that this effect might play a role in porosity formation, but further experiments are needed to confirm that.

Figure 5.20: Keyhole plume jet inducing shielding gas and air flow.

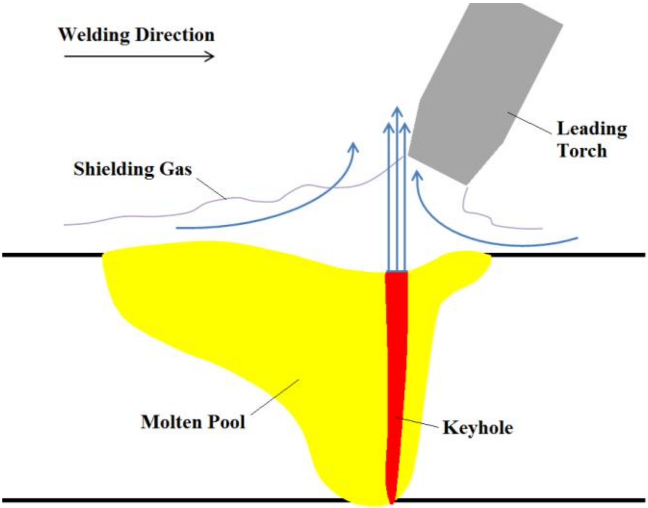

Source: The author

The porosity is probably caused by diffusion of monatomic hydrogen, nitrogen and oxygen dissociated by the electric arc into the molten metal [105]. During solidification, these gases bind together again as H_2, N_2 and O_2. CO is also formed through the reduction of iron oxide, as in the reaction below [106]. For this reason, when the trailing torch remelts the porous region, the gases do not dissolve back into the metal, as the gas molecules are much bigger than nitrogen and oxygen atoms, and they do not get dissociated again, because they are not in the electric arc. Instead they form gas bubbles that float up to the surface and disappear, not inducing porosity again in the second torch pool.

$$FeO + C \leftrightarrow Fe + CO$$

5.2.2.2 Trailing GMAW Torch Zone

Contrary to the first torch zone, the second torch zone showed the least porosity. It even helps reducing overall porosity by remelting part of the very porous leading torch zone.

The first reason for this good aspect is the fact that it is much farther from the cross-jet and the keyhole plume than the other torch, reducing greatly their disturbance on the shielding gas flow.

The trailing torch has another advantage, as its gas nozzle does not need to be cut for the laser beam path, leaving the nozzle in its designed working shape.

Other than that, the forehand position of the second torch might be less prone to porosity formation than the backhand position of the first torch, as has been observed by Afif [107] on GMAW welding of carbon steel.

5.2.2.3 Laser Zone

Some porosity was observed in the laser dominated zone of the hybrid welding. The pores are mostly small and rounded, making them less harmful to the weld mechanical properties.

The pores can be caused by instabilities in the keyhole. Bubbles of gas can form as the bottom of the keyhole collapses due to a knob travelling downward in the front wall. Full penetrating laser welds however are much less sensitive to this effect, as the entrapped gas can escape through the root.

When welding with a 10 kW fiber laser of 0.2 mm focused beam, Katayama *et al* [60] observed the formation of bubbles in the middle of the keyhole that led to pores. Similar high irradiances were used at the experiments carried out in this research work, so this phenomenon can also contribute to the porosity formation in the keyhole zone. Through buoyancy and molten metal flow, those bubbles can reach the leading arc zone and contribute to porosity formation there, but, since very few pores in that zone show the rounded shape observed in the laser zone, this migrating phenomenon should not contribute much to the porosity in the leading GMAW torch zone.

It is also possible that the diluted gases responsible for the high porosity found in the leading GMAW torch zone can affect the laser zone as well, but no relation between the quantity of pores found in the first torch zone and in the laser zone was observed. Welds with severe porosity in the first torch zone did not show more porosity in the laser zone than welds with sound first torch zones. An analysis of the gas content of the pores could indicate their sources. If H_2, N_2, O_2 and CO are the most abundant gases, then the pore is more likely to be the result of diluted nitrogen and oxygen in the molten pool, but, if the shielding gas is more abundant, then it is most probably caused by keyhole instabilities.

5.2.2.4 Root Reinforcement Zone

Bubbles from the keyhole bottom collapse can contribute to the porosity found in the root reinforcement zone of the weld bead. The bubble can travel downward if the molten flow is favorable.

Because of how the edges were prepared, direct contact of the backing flux with the weld root was hard to achieve. The experiments were carried out with a gap of approximately 3 mm between the weld root and the flux, as shown before in figure 4.3, which can compromise the shielding effect of the backing flux. It was also discussed before that high power CO_2 laser welding of steel can lead to severe porosity because of dissociation of N_2 and O_2 in an unshielded backside [66, 67]. The wavelength of the disk laser is less likely to form monatomic hydrogen, nitrogen and oxygen, because the beam energy is more weakly absorbed, but it is still possible that this effect contributes to some degree.

6 CONCLUSIONS

In the scope of the public-funded HYBRILAS research project at the LZH, a hybrid laser – GMA welding with a trailing GMAW acting on distinct molten pools was used to join 23 mm thick API 5L X70 steel plates. Metallographic and x-ray imaging led to the following conclusions.

Filler metal can play a role in the solidification flaw formation, as it can change the viscosity of the weld metal. Higher viscosity can increase the amount of solidification flaws if the formation of a shrinkage pore is part of the solidification flaw development.

It was observed that the beam width at the interaction point influences the solidification flaw formation. In this work, a beam width increase from 400 µm to 600 µm by changing the optical fiber diameter caused severe solidification flaw, most probably caused by a more pronounced bulge in the molten pool.

The welds done with transverse beam oscillation showed different outcomes to each other. Welding performed with a welding speed of 1.4 m/min resulted in severe bulging of the molten pool and solidification flaw was observed in both cross sectional views. On the other hand, the weld performed with 1.2 m/min showed a better geometry and no solidification flaw was observed. However, another discontinuity was present in the leading GMAW torch zone that resembled a solidification flaw and could perhaps be considered one. It is believed that it was caused by lack of material due to solidification shrinkage.

A high relation between solidification flaw and molten pool bulge was detected. Every solidification flaw was found at swollen regions in the molten pool and welds with higher bulge widening angle showed more solidification flaws.

Divergent results were found regarding the welding speed and the heat input effect on the solidification flaw formation. In some cases decreased welding speed and increased heat input resulted in less solidification flaws and less severe molten pool bulging, while the opposite was observed in other tests. The influence from welding speed and heat input seems to be mostly related to the molten pool geometry they deliver, which is hard to predict.

The region most severely affected by porosity was found to be the leading GMAW torch zone, because of the cut nozzle, the cross-jet and the laser keyhole plume disturbance of the shielding gas flow. The trailing torch showed much less pores, since it is farther from those disturbances. By remelting the first torch zone, it helped to reduce the overall porosity of the weld seam.

Little porosity was observed in the laser zone of the weld seam. Those pores were most likely caused by keyhole instabilities. The root reinforcing zone showed more porosity, which was probably caused by insufficient shielding by the backing flux.

Analyzing the results obtained in this dissertation and results found in the literature, two theories were proposed to explain the dubious nature of the solidification flaws, as it sometimes shows more solidification crack characteristics and sometimes it appears more like a shrinkage pore. The first explanation is that there is no such defect as solidification flaw and what is observed are solidification cracks and shrinkage porosity, defects that can happen in similar places with some similar characteristics, but have different formation mechanisms and happen under different conditions. The other possible explanation is that solidification flaws are caused by shrinkage pores that act as stress concentrations and lead to subsequent cracking.

6.1 SUGESTIONS FOR FUTURE WORK

The use of the bulge widening angle was introduced in this work as a way to quantify the severity of a bulge in the molten pool regarding solidification flaw formation in hybrid laser – arc welding, but more tests with different parameters should be done to confirm its usability. Its application could also be tested for laser welding alone. Other means of molten pool geometry evaluation could also be proposed.

The bulges might be caused by local excessive laser beam energy absorption or by the molten pool dynamics. Numerical simulations could be used to find the laser beam energy absorption along the keyhole depth and welds carried to verify if the bulge position matches with regions of increased energy absorption.

The effects of varying the divergence angle and the focal spot position relatively to the weld surface on the keyhole geometry and on the solidification flaw formation should be studied.

Through models, the likelihood of a solidification crack development inside of a bulge in the molten pool without stress concentration should be analyzed. If it is not likely to occur, the same simulations should be carried with shrinkage pores from different sizes. If these pores then induce cracking, it would be a strong evidence supporting the theory that the shrinkage pores act as stress concentration to induce the solidification flaw formation.

A detailed observation of the surface from solidification flaws with crack characteristics should be carried to search for traces of a shrinkage pore. If the presence of shrinkage pores is confirmed for most of those solidification flaws, it would also suggest that the shrinkage pores induce the solidification flaw development by acting as stress concentration.

Numerical simulation can be used to determine the optimal distance between the hybrid laser – GMA welding and the trailing GMAW torch, at which the tensile stresses in solidification crack and solidification flaw sensitive zones are mitigated, because the thermal loads of the trailing GMAW torch can influence the stress field of the hybrid process

The disturbance of the plume jet from the keyhole on the shielding gas flow should be further studied to determine if it can be a contributing factor to porosity.

REFERENCES

[1] ENCYCLOPAEDIA BRITANNICA. **Pipeline**. 2014. Avaiable at: <http://www.britannica.com/>. Date of access: 10/05/2014.

[2] HIPPERT JÚNIOR, E. **Investigação Experimental do Comportamento Dúctil de Aços API-X70 e Aplicação de Curvas de Resistência J-da para Previsão de Colapso em Dutos**. 142 p. Thesis (Ph.D.) Escola Politécnica da Universidade de São Paulo. São Paulo. 2004.

[3] TBG. **Gasoduto Bolívia-Brasil**: Informações Técnicas do Lado Brasileiro. May 2011. Avaiable at: <http://www.tbg.com.br/>. Date of Access: 10/05/2014.

[4] BUCKLAND, B. **An Introduction into the Production and Specification of Steel Pipe**. 2005. Avaiable at: <http://www.piledrivers.org/>. Date of Access: 10/05/2014.

[5] TSURU, E.; HARA, T.; ASAHI, H.; MIYAZAKI, H.; YOSHIDA, T. **High-strength steel pipe excellent in formability and burst resistance**. United States Patent 6782921, 2004.

[6] YAPP, D.; BLACKMAN, S. A. **Recent Development in High Productivity Pipeline Welding**, Fronius, 2004.

[7] AMERICAN PETROLEUM INSTITUTE. **API 5L:** Specification for Line Pipe. Washington D.C., 2007.

[8] SEFFER, O.; Lindner, J.; Springer, A.; Kaierle, S.; Wesling, V.; Haferkamp, H.. Laser GMA Hybrid Welding for Thick Wall Applications of Pipeline Steel with the Grade X70. In: INTERNATIONAL CONGRESS ON APPLICATIONS OF LASER & ELECTRO-OPTICS, 31., 2012, Anaheim. **Proceedings...** Orlando: Laser Institute of America, 2012. pp. 494-501.

[9] OLSEN, F. O. (Ed.); REUTZEL, E. W.; KATAYAMA, S.; MAHRLE, A.; BEYER, E.; GAO, M.; ZENG, Z. Y.; KUJANPÄÄ, V.; KRISTENSEN, J. K.; LIU, L.; STAUFER, H.; THOMY, C. **Hybrid laser-arc welding**. Cambridge: Woodhead Publishing Limited, 2009. 323 pp.

[10] SUDER, W. J. **Study of fundamental parameters in laser hybrid welding**. 2011. 305 pp. Thesis (Ph.D.) - Cranfield University, Cranfield.

[11] KATAYAMA, S. New development in laser welding. In: Ahmed, N. **New developments in advanced welding**, Cambridge: Woodhead Publishing Limited, 2005, pp. 158-197.

[12] STEEN, W. M.; EBOO, M.; CLARKE, J. Arc augmented laser welding. In: INTERNATIONAL CONFERENCE ON ADVANCES IN WELDING PROCESSES, 4., 1978, Harrogate. **Proceedings...** Abington: The Welding Institute, 1978. pp. 257-265.

[13] DVS. **Laserstrahl-Lichtbogen-Hybridschweißverfahren**. Düsseldorf, 2002.

[14] ISF. **Qualifizierung und Nutzung der Hybrid-Synergieeffekte zum Hochleistungsschweißen von Leichtmetallwerkstoffen**. Aachen, 2006.

[15] BAGGER, C.; OLSEN, F. O. Review of laser hybrid welding. **Journal of Laser Applications**, Orlando, v. 17, n. 1, pp. 2-14, 2005.

[16] GAO, M.; ZENG, X. Y.; HU, Q. W. Effects of welding parameters on melting energy of CO2 laser-GMA hybrid welding. **Science and Technology of Welding and Joining**, London, v. 11, n. 5, pp. 517-522, 2006.

[17] MULIMA, J. B. **Hybrid laser arc welding with high power diode laser**. 2008. 290 pp. Thesis (Ph.D.) - University of Wollongong, Wollongong.

[18] GAHAN, B. C.; SHINER, B. New high-power fiber laser enables cutting-edge research. **GasTIPS**, Houston, v. 10, n. 1, pp. 29-31, 2004.

[19] STEEN, W. M. **Laser Material Processing**. 2. ed. London: Springer, 1988. 558 pp.

[20] ANDREWS, J. G.; ATTHEY, D. R. Hydrodynamic limit to penetration of a material by a high-power beam. **Journal of Physics D: Applied Physics**, London, v. 9, pp. 2181, 1976.

[21] SCHUÖCKER, D. Interaction between high power laser beams and matter. In: SCHUÖCKER, D. **High power lasers in production engineering**. London: Imperial College, 1999.

[22] PASCHOTTA, R. **Optical intensity**. Avaiable at: <http://www.rp-photonics.com >. Date of Access: 22/05/2014.

[23] PASCHOTTA, R. **Thin-disk lasers**. Avaiable at: <http://www.rp-photonics.com/>. Date of Access: 22/05/2014.

[24] HECHT, J. **Photonic Frontiers**: Disk Lasers: Higher powers and shorter pulses from thin-disk lasers. 2014. Avaiable at: <http://www.laserfocusworld.com/>. Date of Access: 22/05/2014.

[25] TEISSET, C. ; SCHULTZE, M.; BESSING, R.; HAEFNER, M.; PRINZ, S.; SUTTER, D.; METZGER, T. 300 W picosecond thin-disk regenerative amplifier at 10 kHz repetition rate. In: ADVANCED SOLID-STATE LASERS CONGRESS, 2013, Paris. **Postedeadline Paper...** Washington, DC: Optical Society of America, 2013.

[26] REISGEN, U. ; OLSCHOCK, S.; JAKOBS, S.; SCHLESER, M.; MOKROV, O.; ROSSITER, E. Laser beam submerged arc hybrid welding. **Physics Procedia**, Amsterdam, v. 39, pp. 75-83, 2012.

[27] BIFFIN, J. R.; WALDUCK, R. P. Plasma arc augmented laser welding (PALW). In: EUROPEAN CONFERENCE ON JOINING TECHNOLOGY, 2., 1994, Firence. **Proceedings...** Porto Salvo: European Federation for Welding, Joining and Cutting, 1994. pp. 295-304.

[28] SEFFER, O. LAHDO, R.; SCHNEIDER, F.; SPRINGER, A.; KAIERLE, S. Laser-MIG Welding Process Combination for Thick Wall Applications of the Aluminum Alloy EN AW-6082-T6. In: INTERNATIONAL CONGRESS ON LASER ADVANCED MATERIALS PROCESSING, 6., 2013, Niigata. Proceedings... Osaka: Japan Laser Processing Society, 2013.

[29] LAHDO, R. SEFFER, O.; SPRINGER, A.; KAIERLE, S.; OVERMEYER, L.; COLLMANN, M.; SCHAUMANN, P.; NEUMEYER, J.; SCHÜLBE, H.; NACKE, B. Induction Assisted GMA-Laser Hybrid Welding of High-Strength Fine-Grain Structural Steels. In: INTERNATIONAL CONGRESS ON APPLICATIONS OF LASER & ELECTRO-OPTICS, 31., 2013, Miami. **Proceedings...** Orlando: Laser Institute of America, 2013. pp. 228-236.

[30] MATSUDA, J.; UTSUMI, A. TIG or MIG arc augmented laser welding of thick mild steel plate. **Joining & Materials**, [S.l.], v. 1, pp. 31-34, 1988.

[31] KIM, C. H. ; CHAE, H. B.; KIM, J. K.; KIM, J. H.. Optimization of laser-arc insterspacing distance during CO2 laser-GMA hybrid welding by using high speed imaging. **Advanced Materials Research**, Pfaffikon, v. 1, pp. 481-484, 2007.

[32] KUTSUNA, M.; CHEN, L. Interaction of both plasmas in CO2 laser - MAG hybrid welding of carbon steel. In: SPIE, 4831., 2002, Osaka. **Proceedings...** Bellingham: SPIE, 2002. pp. 341-346.

[33] WANG, J.; WANG, C.; MENG, X.; HU, X.; YU, Y.; YU, S. Interaction between laser-induced plasma/vapor and arc plasma during fiber laser-MIG hybrid welding. **Journal of Mechanical Science and Technology**, New York, v. 25, n. 6, pp. 1529-1533, 2011.

[34] LIU, L. M.; YUAN, S. T.; LI, C. B. Effect of relative location of laser beam and TIG arc in different hybrid welding modes. **Science and Technology of Welding and Joining**, London, v. 17, n. 6, pp. 441-446, 2012.

[35] NIELSEN, S. E.; ANDERSEN, M. M.; KRISTENSEN, J. K.; JENSEN, T. A. Hybrid welding of thick section C/Mn steel and aluminium. In: INTERNATIONAL INSTITUTE OF WELDING ANNUAL ASSEMBLY, 15., 2002. Copenhagen. **Proceedings...** Roissy: International Institute of Welding, 2002. pp. 1731-1732,

[36] BEYER, E.; DILTHEY, U.; IMHOFF, R.; MAJER, C.; NEUENHAHN, J.; BEHLER K. New aspects in laser welding with an increased efficiency. In: INTERNATIONAL CONGRESS ON APPLICATIONS OF LASER & ELECTRO-OPTICS, 12., 1994, Orlando. **Proceedings...** Orlando: Laser Institute of America, 1994. pp. 183-192.

[37] HAAS, E. J. **Arc-augmented laser welding of aluminum**. 113 pp. Thesis (M.Sc.). Oregon Graduate Center. Oregon. 1986.

[38] GUREEV, D. M.; ZAIKIN, A. E.; ZOLOTAREVSKY, A. B. Method of laser-arc material processing and its application. In: PHYSICAL INSTITUTE OF THE USSR ACADEMY OF SCIENCE, 1989, Nauka. **Transactions...** Moscow: Lebedev Physical Institute , 1989 pp. 41-46.

[39] DILTHEY, U. Capabilities of welding processes and their automation potential with a view to the year 2000. In: IINTERNATIONAL INSTITUTE OF WELDING ASIAN PACIFIC WELDING CONGRESS, 1996, Manukau. Proceedings... Roissy: International Institute of Welding, 1996. pp. 65-81.

[40] HERMSDORF, J. **Laserstabilisiertes Metallschutzgasschweißen mittels fasergeführten Festkörperlasern**. Thesis (Dr.) - Leibniz Universität Hannover. Hannover. 2013.

[41] GORNYI, S. G.; LOPOTA, V. A.; REDOZUBOV, V. D. Examination of the electrical characteristics of the arc in laser-arc welding. **Welding International**, Cambridge, UK, v.4, n. 6, pp. 474-476, 1990.

[42] CHEN, Y. B.; LEI, Z. L.; LI, L. Q.; WU, L. Experimental study on welding characteristics of CO2 laser TIG hybrid welding process. **Science and Technology of Welding & Joining**, London, v.11, n. 4, pp. 403-411, 2006.

[43] HU, B.; OUDEN, G. Synergetic effects of hybrid laser/arc welding. **Science and Technology of Welding and Joining**, London, v.10, n. 4, pp. 427-431, 2005.

[44] STEEN, W. M.; ALEXANDER, J. Arc augmented laser welding. **Joining of Metals**, Coventry, 1981.

[45] GAO, M.; ZENG, X.; HU, Q. Effects of gas shielding parameters on weld penetration of CO2 laser-TIG hybrid welding. **Journal of Materials Processing Technology**, Amsterdam, v. 184, n. 1, pp. 177-183, 2007.

[46] NAITO, Y.; MIZUTANI, M.; KATAYAMA, S. Electrical measurement of arc during hybrid welding – welding phenomena in hybrid welding using YAG laser and TIG arc (Third report). **Quarterly Journal of the Japan Welding Society**, Tokyo, v. 24, n. 1, pp. 45-51, 2006.

[47] SHINN, B. W.; FARSON, D. F.; DENNEY, P. E. Laser stabilisation of arc cathode spots in titanium welding. **Science and Technology of Welding and Joining**, London, v. 10, n. 4, pp. 475-481, 2005.

[48] DIEBOLD, T. P.; ALBRIGHT, C. E. Laser-GTA welding of aluminum alloy 5052. **Welding Journal**, Miami, v. 63, n. 6, pp. 18-24, 1984.

[49] ONO, M; SHINBO, Y.; YOSHITAKE, A.; OHMURA, M. Welding properties of thin steel sheets by laser-arc hybrid welding: Laser focused arc welding. In: SPIE, 4831., 2002, Osaka. **Proceedings...** Bellingham: SPIE, 2002. pp. 369-374.

[50] STUTE, U.; KLING, R.; HERMSDORF, J. Interaction between electrical arc and Nd: YAG laser radiation. In: CIRP, 56., 2007, [S.l.]. **Annals...** Amsterdam: Elsevier, n. 1, pp. 197-200, 2007.

[51] SEYFFARTH, P.; KRIVTSUN, I. **Laser-arc processes and their applications in welding and material treatment:** Welding and allied processes. 1. ed. London: CRC Press Taylor & Francis Group, 2002. 200 p.

[52] HU, B.; OUDEN, G. Laser induced stabilisation of the welding arc. **Science and Technology of Welding and Joining**, London, v. 10, pp. 76-78, 2005.

[53] PAULINI, J.; SIMON, G. Theoretical lower limit for laser power in laser-enhanced arc welding. **Journal of Physics D: Applied Physics**, London, v. 26, n. 9, pp. 1523-1527, 1993.

[54] BEYER, E.; BRENNER, B.; POPRAWE, R. Hybrid laser welding techniques for enhanced welding efficiency. In: ICALEO, 81., 1996, Detroit. **Proceedings...** Orlando: Laser Institute of America, 1996. pp. 157-166.

[55] READY, J. F.; FARSON, D. F. Reflectivity and absorptivity of opaque surfaces. In: MODEST, M. F. **LIA handbook of laser materials processing**. Orlando: Magnolia, 2001. pp. 175-181.

[56] TUSEK, J.; SUBAN, M. Hybrid welding with arc and laser beam. **Science and Technology of Welding and Joining**, London, v. 4, n. 5, pp. 308-311, 1999.

[57] KIM, Y. P.; ALAM, N.; BANG, H. S. Observation of hybrid (cw Nd:YAG laser+MIG) welding phenomenon in AA 5083 butt joints with different gap condition. **Science and Technology of Welding and Joining**, London, v. 11, n. 3, pp. 295-307, 2006.

[58] MORGAN, S. A.; WILLIAMS, S. W. Hybrid laser conduction welding. In: Annual Assembly of the International Institute of Welding, 55.,Copenhagen, 2002. **Proceedings...** Roissy: International Institute of Welding, 2002.

[59] LIU, L.; HAO, X. Study of the effect of low-power pulse laser on arc plasma and magnesium alloy target in hybrid welding by spectral diagnosis technique. **Journal of Physics D: Applied Physics**, London, v. 41, n. 20, 10 pp., 2008.

[60] KATAYAMA, S.; KAWAHITO, Y.; MIZUTANI, M. Elucidation of laser welding phenomena and factors affecting weld penetration and welding defects. **Physics Procedia**, [S.l.], v. 5, pp. 9-17, 2010.

[61] GRESES, J.; HILTON, P. A.; BARLOW, P. A.; STEEN, W. M. Plume attenuation under high power Nd: yttrium-aluminum-garnet laser welding. **Journal of Laser Applications**, Orlando, v. 16, n. 1, pp. 9-15, 2004.

[62] LACROIX, D.; JEANDEL, G.; BOUDOT, C. Spectroscopic characterization of laser-induced plasma created during welding with a pulsed Nd:YAG laser. **Journal of Applied Physics**, Melville, v. 81, n. 10, pp. 6599-6606, 1997.

[63] WELDING-ADVISERS.COM. Weld-porosity, know where it comes from. **welding-advisers.com**. Avaiable at: <http://www.welding-advisers.com/ >. Date of Access: 10/05/2014.

[64] NERMAN, P. **Influence of defects and geometry in welded joints**. 2005. 80 pp. Thesis (Licentiate) - Royal Institute of Technology (KTH), Stockholm.

[65] KATAYAMA, S. (Ed.). **Handbook of laser welding technologies**. Cambridge: Woodhead, 2013. 654 pp.

[66] TSUKAMOTO, S.; ARAKANE, G.; KAWAGUCHI, I.; HONDA, H. Keyhole behaviour in high power laser welding of thick steel plates. In: INTERNATIONAL CONGRESS ON APPLICATIONS OF LASERS & ELECTRO-OPTICS, 22., 2003, Jacksonville. **Proceedings...** Orlando: Laser Institute of America, 2003. pp. 176-183.

[67] DONG, W.; KOKAWA, Y.; TSUKAMOTO, S.; SATO, Y. S.; OGAWA, M. Mechanism governing nitrogen absorption by steel weld metal during laser welding. In: METALLURGICAL AND MATERIALS B, 35., 2004, [S.l.]. **Transactions...** Warrendale: The Minerals, Metals and Materials Society, 2004. pp. 331-338.

[68] KAPLAN, A. F. H.; MIZUTANI, M.; KATAYAMA, S.; MATSUNAWA, A. Unbounded keyhole collapse and bubble formation during pulsed laser interaction with liquid zinc. **Journal of Physics D: Applied Physics**, London, v. 35, n. 11, pp. 1218-1228, 2002.

[69] LEGAIT, P. A. **Formation and Distribution of Porosity in Al-Si Welds**. 2002. 109 pp. Thesis (M.Sc.) - Worcester Polytechnic Institute, Worcester, MA, USA.

[70] MATSUNAWA, A. Problems and solutions in deep penetration laser welding. **Science and Technology of Welding and Joinining**, London, v. 6, n. 6, pp. 351-354, 2001.

[71] KATAYAMA, S. Formation mechanisms and preventive procedures of laser welding defects. In: LMP SYMPOSIUM ON HIGH QUALITY AND NEW TREND OF LASER WELDING, 8., 2004, [S.l.]. **Proceedings...** Tokyo: Japan Welding Society, 2004. pp. 8-15.

[72] MATSUNAWA, A.; MIZUTANI, M.; KATAYAMA, S.; SETOo, N. Porosity formation mechanism and its prevention in laser welding. **Welding International**, Cambridge, UK, v. 17, n. 6, pp. 431-437, 2003.

[73] DU, H.; HU, L.; HU, X.; LIU, J. Laser welding of TC-1 titanium alloy. **Journal of Materials Science & Technology**, Shenyang, v.19, n. 5, pp. 475-478, 2003.

[74] KATAYAMA, S .; NAITO, Y.; UCHIUMI, S.; MIZUTANI, M. Physical phenomena and porosity prevention mechanism in laser-arc hybrid welding. In: JWRI, 35., 2006, Osaka. **Transactions...** Osaka: Joining and Welding Research Institute, 2006. pp. 13-18.

[75] DAVIES, G. J.; GARLAND, J. G. Solidification structures and properties of fusion welds. **International Materials Reviews**, London, v. 20, p. 83, 1975.

[76] LEES, D. C. G. Hot Tearing Tendencies of Aluminium Casting Alloys. **Journal of the Institute of Metals**, Nagoya, v. 72, pp. 343-364, 1946.

[77] SINGER, A. R. E.; JENNINGS, P. H. Hot-Shortness of Some Aluminium-Iron-Silicon Alloys of High Purity. **Journal of the Institute of Metals**, Nagoya, v. 73, pp. 273-284, 1947.

[78] INTERNATIONAL ORGANIZATION FOR STANDARDIZATION. **ISO 5817:2014, Welding -- Fusion-welded joints in steel, nickel, titanium and their alloys (beam welding excluded) -- Quality levels for imperfections**. Geneva, 2014.

[79] KOU, S. **Welding metallurgy**. 2. ed. Hoboken: John Wiley & Sons, 2003. 480 pp.

[80] DILTHEY, U. **Schweißtechnische Fertigungsverfahren – Verhalten der Werkstoffe beim Schweißen.** 3. ed. Berlin-Heidelberg: Springer-Verlag, v. 2, 2005.

[81] SMITH, R. B. **ASM Handbook:** Welding, Brazing, and Soldering. 9. ed. Materials Park, OH: ASM International, v. 6, 1993.

[82] CHIHOSKI, R. A. The character of stress fields around a weld arc moving on aluminum sheet. **Welding Journal**, New York, v. 51, n. 1, pp. 9-18, 1972.

[83] ZACHARIA, T. Dynamic stresses in weld metal hot cracking. **Welding Research Supplement**, New York, pp. 164-172, July 1994.

[84] BLODGETT, O. W. **The Welding Innovation Quarterly**, Cleveland, v. 2, n. 3, 4 pp., 1985.

[85] WOUTERS, M. **Hybrid laser-MIG welding: An investigation of geometrical considerations**. 2005. 59 pp. Thesis (Licentiate) - Luleå University of Technology. Luleå. 2005.

[86] KELLER, H. **CO2-Laserstrahl-MSG-Hybridschweißen von Baustählen im Blechdickenbereich von 12 bis 25 mm**. Aachener Berichte Fügetechnik. Aachen. 2003.

[87] KRISTENSEN, J. K. Trends and developments within welding and allied processes. In: Annual Assembly of the International Institute of Welding, 55.,Copenhagen, 2002. **Proceedings...** Roissy: International Institute of Welding, 2002.

[88] RETHMEIER, M.; GUMENYUK, A. Schweißen mit dem Faserlaser. In: Institut für Füge Kolloquium, 2007, Dresden. **Proceedings...** Braunschweig: Institut für Füge, 2007.

[89] BUNDESANSTALT FÜR MATERIALFORSCHUNG UND -PRÜFUNG. **Qualifizierung des Nd:YAG- und CO2-Laser-Plasma-Pulver-Hybridschweißens**. Berlin. 2006.

[90] KRISTENSEN, J. K.; HANSEN, L. E.; NEILSEN, S. E.; BORGGREEN, K. Laser welding of C-Mn steels and duplex stainless steels. In: EUROPEAN SYMPOSIUM ON ASSESSMENT OF POWER BEAM WELDS, Geesthacht, 1999. **Proceedings...** Geesthacht: GKSS-Forschungszentrum, 1999.

[91] WEISE, S. **Heißrißbildung beim Laserstrahlschweißen von Baustählen**. Bremen: BIAS, 1998. 122 pp.

[92] SLV HALLE GMBH. **Erstarrungsbedingte Gefügetrennungen beim Hochenergieschweißen**. Halle. 2009.

[93] KRISTENSEN, J. K.; BORGGREEN, K.; KNUDSEN, S. Large scale testing of laser welded structural steels. In: CONFERENCE ON THE JOINING OF MATERIALS, 8., 1997, Elsinore, 8., 1997. **Proceedings...** Helsingor: Institute for the Joining of Materials, 1997. pp. 1-13.

[94] SEFFER, O. **Prozessentwicklung zur Anwendung einer brillanten Laserstrahlquelle für das Laser-MSG-Hybridschweißen von Pipelinestahl mittels quer zur Schweißrichtung pendelnden Energiequellen**. 2012. 121 pp. Dissertation (Dipl.) - Leibniz Universität Hannover, Hannover.

[95] KOROLCZUK-HEJNAK, M.; MIGAS, P. Analysis of selected liquid steel viscosity. **Archives of Metallurgy and Materials**, Krakow, v. 57, n. 4, pp. 963-969, 2012.

[96] METZBOWER, E. A.; MOON, D. W.; FRASER, F. W. Laser Welding of Structural Alloys. In: INTERNATIONAL CONFERENCE ON WELDING TECHNOLOGY FOR ENERGY APPLICATIONS, 14., 1982, Gatlinburg. **Proceedings...** Oak Ridge: Oak Ridge National Laboratory, 1982. pp. 313-329.

[97] KANNATEY-ASIBU JR., E. **Principles of Laser Material Processing**. Hoboken: John Wiley & Sons, 2009. 849 pp.

[98] CHENG, Y.; JIN, X.; LI, S.; ZENG, L. Fresnel absorption and inverse bremsstrahlung absorption in an actual 3D keyhole during deep penetration CO2 laser welding of aluminum 6016. **Optics & Laser Technology**, Amsterdam, v. 44, pp. 1426-1436, 2012.

[99] ZHANG, Y.; SHI, R.; LI, L. Determination of energy coupling to material in laser welding by a novel “sandwich” method. In: NONFERROUS METALS SOCIETY OF CHINA, 22., [S.l.]. **Transactions...** Changsha, 2012. pp. 1701-1710.

[100] JIN, X.; CHENG, Y.; ZENG, L.; ZOU, Y.; ZHANG, H. Multiple reflections and Fresnel absorption of Gaussian laser beam in an actual 3D keyhole during deep-penetration laser welding. **International Journal of Optics**, Cairo, v. 39, n. 21, 8 pp., 2012.

[101] JÜPTNER, W.; SEPOLD, G.; SCHUBERT, E.; WEISE, S.; KURGUSOW-LINK, A. Modellierung der Heißrißeignung unlegierter Stähle beim Laserstrahlschweißen. **Strahltechnik Band**, Bremen, v. 6, pp. 143-150, 1998.

[102] JACOBSKÖTTER, L. **Laserstrahlschweißen thermomechanisch gewalzter Grobbleche in Dicken zwischen 10 mm und 30 mm**: Vergleich und Kombination mit konventionellen Schweissverfahren. Aachen: Shaker, 1996. 168 pp.

[103] MALY, H. **Laserstrahlschweißen mit Zusatzwerkstoff – Untersuchungen zur Beeinflussung der Nahteigenschaften von Grobblechen**. 1998. 202 pp. Thesis (Dr.) - Rheinisch-Westfälische Technische Hochschule, Aachen.

[104] HENDRICKS, M. **Qualitätsuntersuchungen an Laserstrahlschweißverbindungen un-, niedrig- und hoch-legierter Stähle**. Aachen: Shaker, 1991. 117 pp.

[105] MESSLER JR., R. W. **Principles of welding:** Processes, physics, chemistry, and metallurgy. 1. ed. New York: John Wiley & Sons, 1999. 685 pp.

[106] WARREN, D.; STOUT, R. Porosity in Mild Steel Weld Metal. **Welding Journal**, New York, v. 31, n. 8, pp. 381-388, 1952.

[107] AFIF, M. **Comparison of porosity formation in backhand and forehand welding techniques in carbon steel welding with GMAW process**. Universiti Kuala Lumpur, Kuala Lumpur. 2014.